

Thesis ETH No 13080

**MICRO- AND MACROMECHANICAL
PROPERTIES OF KNITTED FABRIC
REINFORCED COMPOSITES (KFRCs)
WITH REGARD TO
ENVIRONMENTAL EXPOSURE**

Dissertation submitted to the

SWISS FEDERAL INSTITUTE OF TECHNOLOGY ZURICH

for the degree of

DOCTOR OF TECHNICAL SCIENCES

presented by

ROLAND REBER

Dipl. Mat. Sci. ETH

born June 26, 1969

citizen of Schangnau, BE

accepted on the recommendation of

Prof. Dr. E. Wintermantel, examiner

Prof. Dr. P. J. Uggowitzer, co-examiner

1999

Seite Leer /
Blank leaf

To Gabriela. Stefan. Ursula. Felix

ABSTRACT

Knitted fabric reinforced composites (KFRCs) offer several advantages over other composite materials, such as high drapability and low production costs. In this work, two fiber/matrix materials, addressing different fields of application, were investigated: Knitted carbon fiber reinforced poly(ether-ether-ketone) (CF/PEEK) is currently considered for biomedical and aerospace engineering, because of its biocompatibility, excellent environmental resistance and high mechanical properties, respectively. Knitted glass fiber reinforced poly(ethylene-terephthalate) (GF/PET) is of interest for the automotive industry, due to an attractive price combined with good mechanical properties.

A requirement for the use of new materials in actual applications is an extended database of properties, thus enabling reliable engineering. This work addresses micro- and macromechanical properties of KFRCs with respect to potential environmental degradation in the focussed applications.

Since the mechanical performance and the failure behavior is mainly defined by the reinforcing knitted fabric layers, the 3D structure of KFRCs was reconstructed based on polished 2D cross sections of consolidated panels. The knit layers were found to be highly interpenetrated, hence suppressing distinctive interlaminar fracture planes. This observation was confirmed in falling weight impact, where delamination in between knit layers did not occur. The out-of-plane failure, determined in compact tension testing, was also found to be highly dependent on reinforcing structure: Crack growth was controlled by the strength of fiber bundles oriented perpendicular to the fracture path. This was considered to be a determining factor leading to the higher fracture toughness of KFRCs, compared to other composites.

The environmental resistance plays a crucial role in the focussed applications of KFRCs. With respect to the biomedical potential of CF/PEEK, hygrothermal long-term degradation in water and simulated body fluid (SBF) at 37, 60 and 90°C was investigated. After 50 weeks of exposure, CF/PEEK showed no influence of environmental degradation on fracture toughness, bending and impact properties. In contrast, a significant reduction of macro- and microscopical properties was observed in exposed GF/PET. The contribution of the microscopical fiber/matrix interface to this behavior was analyzed by the push-out method. An energy-based model was proposed to extract interfacial properties and to relate them with degradation effects. This allowed a quantitative correlation between microscopical and macroscopical failure behavior. One of the conclusions was that the reduction of mechanical properties of GF/PET was not only caused by degradation of the matrix, but also by degradation of the fiber/matrix interface.

In conclusion, the studied KFRCs were found to be damage tolerant materials, revealing high fracture toughness and impact properties in combination with a pronounced delamination resistance. While GF/PET was observed to be critical for applications involving moisture and elevated temperatures, CF/PEEK exhibited outstanding environmental resistance. Therefore, knitted CF reinforced PEEK is a promising candidate for structural biomaterials, such as load-bearing implants.

ZUSAMMENFASSUNG

Gestrickverstärkte Verbundwerkstoffe (KFRCs) bieten mehrere Vorteile gegenüber anderen Verbundwerkstoffen, wie zum Beispiel hohe Drapierbarkeit und tiefe Produktionskosten. In dieser Arbeit wurden zwei verschiedenen Faser/Matrix Kombinationen untersucht, welche auf unterschiedliche Anwendungsbereiche ausgerichtet sind: Polyetheretherketon, verstärkt mit Kohlenstoffasergestriken (CF/PEEK), wird aufgrund seiner Biokompatibilität, seiner ausgeprägten Beständigkeit gegenüber Umwelteinflüssen und seiner hohen mechanischen Eigenschaften für Anwendungen im Bereich der Medizinaltechnik und Luftfahrtindustrie in Betracht gezogen. Polyethylenterephthalat, verstärkt mit Glasfasergestriken (GF/PET), ist von Interesse für die Automobilindustrie, aufgrund seiner geringen Kosten kombiniert mit guten mechanischen Eigenschaften.

Um ein neues Material verlässlich einsetzen zu können ist eine ausführliche Datenbank von Materialkennwerten erforderlich. Diese Arbeit befasst sich solchen Kennwerten: Mikro- und makromechanische Eigenschaften von KFRCs wurden in Bezug auf das Versagensverhalten und unter dem Aspekt möglicher Umwelteinflüsse in den oben genannten Anwendungsbereichen untersucht.

Da die mechanischen Eigenschaften und das Versagensverhalten hauptsächlich durch das verstärkende Gestrick gegeben sind, wurde die 3D Struktur von KFRCs unter Verwendung von 2D Schliffbildern rekonstruiert. Es wurde eine starke gegenseitige Durchdringung der Gestrickslagen festgestellt, welche die Ausbildung von interlamina- ren Bruchebenen verhindert. Dies wurde in Stossversuchen (Impact) bestätigt, bei welchen keine Delamination entlang der Gestrickslagen beobachtet wurde. Ebenso wurde ein Zusammenhang zwischen der Verstärkungsstruktur und dem out-of-plane Versagen im bruchmechanischen Compact Tension Experiment festgestellt: Das Risswachstum wird durch die Festigkeit der Faserbündel, welche senkrecht zur Rissebene stehen, kontrolliert. Dies wird als Faktor für die im Vergleich zu anderen Verbundwerkstoffen höhere Bruchzähigkeit von KFRCs angesehen.

Die Beständigkeit gegenüber Umwelteinflüssen spielt eine zentrale Rolle für den Einsatz von KFRCs. Bezogen auf die Anwendung im Bereich der Medizinaltechnik, wurde die hydrothermische Langzeit-Degradation von CF/PEEK in Wasser bzw., in "simulated body fluid" (SBF) bei 37, 60 und 90°C untersucht. Nach einer 50-wöchigen Auslagerung zeigten die Proben keine Veränderungen, weder in der Bruchzähigkeit, noch in den Biege- und Impacteigenschaften. Im Gegensatz dazu wurde bei GF/PET eine signifikante Abnahme der mikro- und makroskopischen Eigenschaften gemessen. Die Bedeutung der mikroskopischen Faser/Matrix Grenzfläche wurde mittels Push-out Methode untersucht. Basierend auf Energiebetrachtungen, wurde ein Modell entwickelt, welches die Bestimmung der Grenzflächeneigenschaften und damit eine Zuordnung der Degradationseffekte erlaubte. Dies ermöglichte eine quantitative Korrelation zwischen mikroskopischem und makroskopischem Versagensverhalten und erlaubte unter anderem die Schlussfolgerung, dass die Reduktion der mechanischen Eigenschaften von

GF/PET durch hydrolytische Degradation, nicht nur der Matrix, sondern auch der Faser/Matrix Grenzfläche, bedingt ist.

Zusammenfassend erwiesen sich die untersuchten KFRCs als schadenstolerante Werkstoffe, die hohe Bruchzähigkeit, hohe Impacteigenschaften, sowie einen ausgeprägte Delaminationswiderstand zeigten. Während sich die Anwendung von GF/PET in Zusammenhang mit Feuchtigkeit und erhöhten Temperaturen als kritisch erwiesen hat, wurde für CF/PEEK eine aussergewöhnliche Beständigkeit gegenüber SBF und Wasser festgestellt. Daraus folgt, dass PEEK, verstärkt mit Kohlenstoffasergestricken, ein vielversprechender Werkstoff für biomedizinische Anwendungen ist, wie z.B. für lasttragende Implantate.

TABLE OF CONTENTS

Abstract

Zusammenfassung

1. Introduction	1
1.1. Fiber reinforced composites in biomaterials	1
1.2. Environmental exposure of fiber reinforced polymers (FRPs)	3
1.3. Textile composites	4
1.4. Knitted fabric reinforced composites (KFRCs)	6
1.5. Aim and structure of the thesis	8
2. Materials and manufacturing	12
2.1. Fiber/matrix materials	12
2.2. Manufacturing of KFRCs	14
3. 3D-Structure of KFRCs	17
3.1. Introduction	17
3.2. Methods	18
3.2.1. Sample manufacturing	18
3.2.2. Monitoring of polished sections	18
3.2.3. Stacking of cross sections	19
3.2.4. Identification of fiber bundles	20
3.2.5. 3D reconstruction	21
3.3. Results and discussion	21
3.3.1. Cross sections	21
3.3.2. Single bundle	23
3.3.3. Knit layers	24
3.3.4. Quantitative analysis	27
3.4. Conclusions	28
4. Failure behavior I: Crack growth and fracture toughness in mode I	29
4.1. Introduction	29
4.2. Methods	30
4.2.1. Thermography	30
4.2.2. Modified compact tension (CT) test	32
4.3. Results and discussion	40
4.3.1. Thermography	40
4.3.2. Energy release rates G_{IC}	43
4.3.3. Fracture toughness K_{IC}	48
4.3.4. SEM analysis	49
4.4. Conclusions	53

5.	Failure behavior II: Instrumented falling weight impact	56
5.1.	Introduction	56
5.2.	Methods	57
5.3.	Results and discussion	60
5.3.1.	Perforation impact	60
5.3.2.	Low energy impact	67
5.4.	Conclusions	69
5.4.1.	Comparison of CF/PEEK and GF/PET	69
5.4.2.	Comparison with other composite materials	70
5.4.3.	General conclusions	72
6.	Influence of environmental exposure on the mechanical properties of KFRCs	74
6.1.	Introduction	74
6.1.1.	Environmental stability of CF/PEEK	74
6.1.2.	Hygrothermal stability of GF/PET	76
6.2.	Methods	77
6.2.1.	Environmental conditions	77
6.2.2.	Characterization	79
6.3.	Results and discussion	81
6.3.1.	Mass gain	81
6.3.2.	Effects on the mechanical properties of knitted CF reinforced PEEK	83
6.3.3.	Effects on the mechanical properties of knitted GF reinforced PET	91
6.4.	Conclusions	96
7.	Interfacial properties of KFRCs investigated by means of the push-out method	98
7.1.	An energy-based analytical push-out model applied to characterize the interfacial properties of knitted glass fiber reinforced PET	98
7.1.1.	Introduction	98
7.1.2.	Materials and methods	99
7.1.3.	Energy-based analytical model	103
7.1.4.	Results and discussion	110
7.1.5.	Conclusions	118
7.2.	Push-out analyzer	120
7.2.1.	Introduction	120
7.2.2.	Interactive window I: Data	120
7.2.3.	Interactive window II: Analyze	121
7.2.4.	Interactive window III: Calculate	122
7.2.5.	Conclusions	124

7.3. Effects of environmental exposure on the interfacial properties of knitted GF reinforced PET	124
7.3.1. Introduction	124
7.3.2. Materials and methods	124
7.3.3. Results	126
7.3.4. Discussion	131
7.3.5. Conclusions	133
8. Final conclusions	134
9. References	137
List of abbreviations and symbols	146
Acknowledgments	147
Curriculum vitae	148

1. INTRODUCTION

The concept on which composite materials are founded is very old and applied in many natural materials. However, modern reinforced composites based on artificial fibers exist for barely more than 60 years [1]. Although glass and nylon fibers were originally produced for textile purposes, high properties of the fibers led to their use as reinforcement. The development of carbon fibers introduced a class of material which can achieve several times the stiffness of steel at a fraction of its weight.

Fiber reinforced composites (FRCs) reveal high mechanical properties in the direction of the reinforcing fibers. By orienting the fibers in the direction of the applied load, very high stiffness and strength of the component can be achieved. However, load requirements in actual applications are generally not uniaxial. Stacking of unidirectional (UD) layers to multidirectional laminates enables fiber reinforcement in different directions. In-plane properties of multidirectional laminates can be adjusted to the load requirements through appropriate choice of layer orientation and number. However, the out-of-plane properties of these laminates are always determined by the matrix and therefore severely limited [2]. Furthermore, because of their layer structure, laminates are sensitive to interlaminar fracture, i.e. delamination. By introducing fibers with an off-axis angle to the laminate plane, out-of-plane properties and interlaminar fracture toughness can be significantly improved. The incorporation of out-of plane fibers requires textile processing techniques. A brief introduction to textile composites is given in chapter 1.3.

FRCs were primary developed for aerospace and defense applications. In these industries, high performance considerations overbalance cost efficiency criteria. Nowadays, fiber reinforced composites are also use in larger-volume industry, e.g. in the automotive industry, mainly because of the decreasing price of fibers and the increasing importance of weight reduction [3, 4]. The steadily increasing global activity in the field of composite materials lead to a large variety of commercially available FRCs. Today, they are used in almost any engineering industry.

1.1. Fiber reinforced composites in biomaterials

The European Society for Biomaterials (ESB) defined biomaterials as “non-viable materials, used in a medical device, intended to interact with biological systems” [5]. Biomaterials seek to be biocompatible, i.e. "the ability of a material to perform with an appropriate host response in a specific application". Wintermantel [6, 7] extended this definition and distinguished between surface and structural compatibility of an implant. Surface compatibility is understood as the chemical, physical, biological and morphological suitability of the implant surface properties aiming at clinical desired interactions with the surrounding tissue. Structural compatibility is the optimal adaptation to the mechanical behavior of the hosting tissue. Therefore, structural compatibility refers to

the mechanical properties of the implant material, such as stiffness and strength. Optimal interaction between biomaterial and host is reached when both, surface and structural compatibility are taken into account.

Many human tissues are anisotropic and reveal a structure similar to composite materials. This affinity has been realized and consequently attempts were made to use fiber reinforced composites to replace parts of the human body. It is not the intention of this work to give an overview of all possible biomaterials applications of FRCs, however, some typical examples will be discussed.

Load-bearing implants for bone replacement and fixation, made of fiber reinforced polymers (FRPs) are currently developed because they offer several advantages over metal implant materials:

- Stiffness, strength and anisotropy can be adapted to the biological requirements in a large range, thus offering optimized structural biocompatibility. Stress shielding can be disabled by adopting stiffness and therefore minimizing strain mismatch between implant material and bone tissue.
- Absence of metal ions, thus preventing allergic reactions.
- Adjusting of x-ray transparency by adding contrast medium to the polymeric matrix.
- FRPs cause no artifacts in MRI (magnetic resonance imaging) and CT (computer tomography).

Typical examples of on-going research in the field of load bearing implants made of FRPs are hip prostheses, osteosynthesis plates and artificial intervertebral discs.

Design, processing, characterization and clinical application of FRP hip prostheses were investigated by many researchers [8-14]. The general statement of these studies is that stiffness and anisotropy of composite prostheses can be well adapted to cortical bone, thus minimizing strain mismatch and stress shielding effects. However, the required fatigue strength and surface compatibility considerations, such as coating of FRP prostheses, are still a matter of investigation.

An early clinical comparison of metal and FRP bone plates revealed less cortical porosity after healing using the composite plate [15]. Bone fixation using FRPs were found to be advantageous because of their low stiffness, thus promoting the formation of external callus which increases fracture strength after healing [16, 17]. Development of a knitted fabric reinforced composite (KFRC) bone plate is presented in [18]. There, it was found that formed-in holes increased the fiber density and therefore, the strength in the critical area around the holes. Good results by forming holes in the fabric instead of drilling them after composite manufacturing were also found in [19].

Similar to these examples, the main advantage of artificial disks made of composite materials, is their mechanical similarity to the replaced part, i.e. the natural disk [20]. Encouraging studies with intervertebral discs cages consisting of carbon fiber reinforced polymer are described in [21, 22]. Using a soft elastomeric core and reinforcing fiber sheets, a total disc prostheses is proposed in [23]. Knitted fabric reinforced elastomere

was chosen by Ramakrishna [24], because of its stress-strain behavior similar to intervertebral disks. In his study, knitted kevlar fabrics were used to encapsulate a polyurethane nucleus. It is presumed that the most promising artificial disk duplicates not only its natural form but also its function [20]. Under this viewpoint, it seems evident that FRCs do have a high potential as implant materials.

1.2. Environmental exposure of fiber reinforced polymers (FRPs)

As any other material in service, FRPs are subjected to the influence of their environment. The function of the composite part must be fulfilled during its entire life time. Certain biomedical applications, e.g. load-bearing implants are intended to remain in the human body for several decades, where they are exposed to the body electrolytes. Other high performance materials, such as primary and secondary structures in aerospace applications are exposed to various environmental factors like large and fast changing temperature differences, moisture and chemical fluids.

Unlike metals, FRPs are composed of two phases which introduces different aspects considering their environmental sensitivity. First, polymers are not impervious to moisture penetration. Second, they include fiber/matrix interfaces. The mechanical behavior of FRPs, as anisotropic, inhomogeneous materials, is very complex and is a function of the synergistic properties of fiber, matrix, fiber/matrix interface, and of geometric properties such as distribution and orientation of the reinforcement. With regard to environmental degradation, the most critical properties that have to be considered are the interface characteristics. The fiber/matrix interface, as an adhesive bond, is potentially sensitive to moisture degradation. Strength and failure behavior are significantly influenced by the interface, because it is the location of stress transfer.

The influence of environmental exposure on FRPs is described in many research papers [25-39]. Generally, it can be distinguished between micro- and macromechanical approaches. In micromechanical studies, the fiber/matrix interface was characterized using an interface test method before and after environmental exposure [25-29]. In macromechanical approaches, composite parts were tested for environmental sensitivity by means of standard mechanical test methods, such as tensile, bending, shear and compression experiments [30-39]. Most work was performed on carbon fiber (CF) reinforced polymers for high performance applications like load-bearing implants and aerospace structural parts. However, the reported results are contradictory. For instance, decreasing mechanical properties as a function of exposure time were found for CF reinforced PEEK in [26, 28, 40, 41] while no significant exposure effects are reported by [33, 35, 38, 39]. These opposed results can be better understood, when considering that the influence of environmental exposure on CF/PEEK not only depends on fiber/matrix materials and environmental conditions but also on test methods and reinforcement architecture. A study focussed on the influence of interface degradation on the knitted reinforced struc-

tures was performed by Mayer [42], who observed a strong dependence of the failure behavior on fiber/matrix adhesion

In the presented work, environmental exposure of knit fiber reinforced composites (KFRCs) was studied. The purpose of the investigation was twofold: (a) the environmental sensitivity of the materials was assessed, and (b) the influence of matrix and interface properties on the mechanical properties of KFRCs was studied.

1.3. Textile composites

Composites with reinforcing textile fibers are called textile composites. If they are designed for primary and secondary load-bearing applications, they are defined as textile structural composites [43]. Classification of textile structural preforms is complex because it reflects macrogeometry, i.e. shape and orientation, method of fabrication and microgeometry, i.e. direction of reinforcement [44]. Fukuta et al. [45] classified textile structural reinforcements according to the axis of fiber or yarn introduction and geometric dimensions. According to this classification, laminates made of stacked UD layers are mono-axial (fiber introduction), three dimensional (3D) composites (geometric dimensions). Contrary to Fukuta's classification and in accordance with most researchers in the composite field, 3D textile fabrics are defined as fully integrated structures, having multi-axial in-plane and out-of-plane fiber orientations [44, 46-48]. Ko [44] excludes two dimensional (2D) textile fabrics sewed together after formation of the fabric from these integrated 3D textiles, which are all manufactured with an inherent through-the-thickness¹ yarn component. 2D fabrics are defined as flat textile fabrics with most of the fibers oriented in the plane of the fabric. In braiding, knitting and weaving, yarns are intermeshed which introduces a curvature that results in out-of-plane orientation of a small fiber portion. Figure 1.1 gives an overview of selected 2D and 3D textile fabrics.

1. "Through-the-thickness" means perpendicular to the fabric plane and is a commonly used term in the field of textile composites.

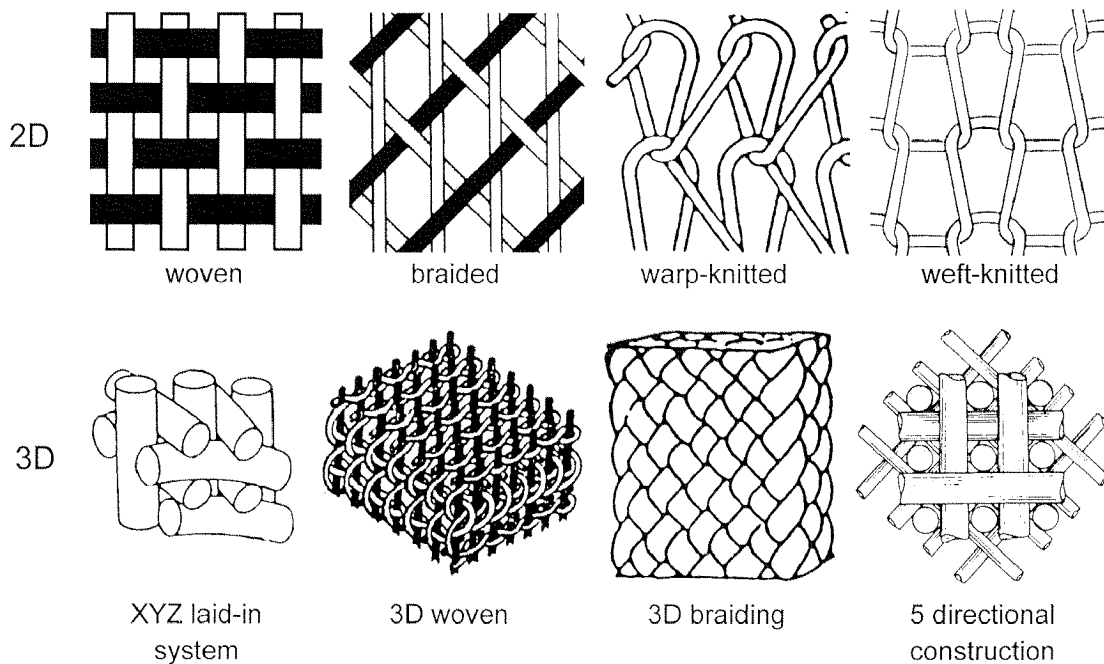


Figure 1.1: Two dimensional (2D) and three dimensional (3D) textile fabrics used as reinforcements in structural textile composites. 3D textile fabrics reveal intentionally integrated fibers in out-of-plane direction while in 2D composites only a small part of fibers are oriented in out-of-plane direction because of the intermeshing of yarns.

The additional through-the-thickness reinforcement of fully integrated 3D textile fabrics makes the resulting composites strongly resistant to delamination [44]. Energy released in model I interlaminar fracture of 3D orthogonal interlock fabrics showed 10 times higher values than that of 2D laminates [49]. However, the textile manufacturing process for 3D integrated fabrics is complex and therefore expensive. Stitching, a traditional textile joining technology, can be applied to reduce the interlaminar delamination sensitivity of 2D textile composites [50, 51]. Textile layers are stitched together with a sewing thread. Stitching of textile composites is limited by the fact that some fiber types, e.g. carbon fibers, are too brittle to be used as sewing threads and that fiber damage caused by the stitching process reduces the composite in-plane properties [49].

An attractive alternative to 3D and stitched textile composites is found in knitted fabric reinforced composites (KFRCs). KFRCs offer the advantage of low production costs combined with the largest out-of-plane orientation observed in non-stitched 2D textile composites.

1.4. Knitted fabric reinforced composites (KFRCs)

Knitted fabrics for reinforcement are made of yarns. Yarns are defined as a linear assemblage of fibers formed into a continuous strand having textile-like characteristics [52]. The knit structure is built by interlooping one or more yarns, thus forming loops, the basic structure unit of any knitted fabric. In knitting, loops are drawn through a previously made loop using needles. A variety of differently knitted fabrics, e.g. warp-knitted, weft-knitted, plain- and rib structures, with and without inlay yarns, are used as composite reinforcements.

Fabrics that are knitted together belong to the class of stitched textile preforms. Considerable research was performed on this class [53-58]. Within this class, knitted non-crimp¹ fabrics represent a textile structure in which highly oriented non-crimp reinforcement, e.g. inlay yarns are used to avoid shrinkage and deformation due to the waviness of the fibers. [59-61]. Consequently, the flexibility of the textile preform is suppressed. Since the properties of these materials are not mainly defined by the knit structure, they will not be further considered in the frame of the presented study. This work is focussed on the most basic existing knit structures, i.e. plain weft-knitted fabrics. The plain weft-knit structure is schematically presented in figure 1.1. The definitions of the structural units in weft-knitted fabrics are indicated in figure 2.1 of chapter 2.

Weft-knitted fabrics are manufactured on flat bed or circular knitting machines. The fabrics used in this work were produced on a circular knitting machine, using the contrary technique [62]. This technique applies very low stress on the fiber yarns, thus reducing fiber damage significantly. All yarn types, e.g. continuous carbon and glass fiber yarns, commingled/intermingled² yarns, FIT (fiber impregnated thermoplastic) yarns, staple yarns, can be knitted using the contrary technique. Definitions and a comparison of the different yarn types are given in [46, 48, 52]. Co-knitting, i.e. merging of reinforcing and polymer fiber yarns directly before knitting was applied to manufacture the composites studied in this work. Co-knitting does not involve yarn intermingling processes and, therefore, reduces the production costs.

Properties of materials reinforced with knitted fabrics were first investigated by Marvin [63] as early as in 1961. Marvin investigated properties of glass fiber reinforced laminates. Surprisingly, after this first paper almost no research on KFRCs was published until the late 80's with the exception of Varin [64] who studied drapability and low production possibilities of KFRCs in 1982. As a result of a revived interest in textile composites during the 80's [43], the number of publications treating KFRCs increased significantly towards the end of that decade. Today, a large number of scientific studies are available, dealing with different aspects of KFRCs.

-
1. Non-crimp fabrics are close to a non-crimp state, i.e. the suppression of the fabrics' extensibility, which is caused by their waviness due to interlacing of yarns.
 2. Commingled is a general term expressing the existence of two fiber types in one yarn. Intermingling is a specific process applied to obtain fiber mixtures. Generally, the two terms are used as synonyms.

Many studies concern basic mechanical properties of KFRCs [18, 65-78]. Most experimental work presented in these papers was performed using tensile and/or flexural testing. Stiffness and strength values, anisotropy considerations and comparisons of different materials and knit structures are given. More specific investigations of the failure behavior and damage tolerance are found in [79-85]. High fracture toughness and low notch-sensitivity of KFRCs were reported in these papers. Energy absorption capabilities and impact behavior were studied in [79, 86-88]. It was found that the impact properties of KFRCs are advantageous in comparison with other composite materials. Few work was published concerning fatigue properties of KFRCs [89, 90]. In a recent study on the fatigue properties of KFRCs produced from staple yarns, high fatigue strengths was determined [91]. Interface/interphase¹ characteristics and their effect on mechanical properties of KFRCs were studied in [42, 92-96]. It was found that interface properties reveal a strong influence on strength and failure behavior of KFRCs. The results gained in experimental studies are often concluded in models, describing the elastic properties of KFRCs [47, 97-105]. Most of these models are based on finite element modeling (FEM). Analytical models, predicting failure strength under specific load conditions are presented in [46, 84]. Some general studies treating various of the aspects mentioned above, and thereby summarizing potentials and limitations of KFRCs are reported in [46, 48, 75, 98, 106, 107].

In conclusion, it can be stated that research, and consequently knowledge, of KFRCs has considerably increased in the last ten years. However, the portion of composite applications in which KFRCs are currently used is still small. Various reasons are responsible for this fact:

- Intuitively, knitted fabrics are considered as loose structures, inappropriate for structural applications [107]. In spite of the fact that their load-bearing capabilities have been proven, the use of KFRCs is still inhibited by their reputation.
- It has been stated that sufficient fiber volume contents cannot be reached in KFRCs [44, 108, 109]. This common misunderstanding has been rectified in many of the aforementioned studies. By using knit structures with low areal loop density and by stacking several knit layers, fiber volume contents of 50% and more can be reached [18, 48, 72-75, 81, 106, 107, 110].
- There is an almost infinite variety of knit structures and fiber/matrix combinations that can be used in KFRCs. Even though being a major advantage, this may also complicate the establishment of a comprehensive database for these materials. According to Ko et al, an extensive database is an inevitable requirement to increase the industrial use of textile composites [111].

1. In the present work, the term interphase is used for three dimensional phases located between fiber and matrix bulk, while interfaces are referred to two dimensional surfaces.

On the other hand, the interest for KFRCs is steadily increasing. The main reasons creating this interest are the followings:

- As mentioned above, knitted fabrics are very flexible structures. The resulting drapability is excellent compared to other reinforcing structures, e.g. woven fabrics. Complex structures can be shaped and reinforcement at strong curvatures is possible [18, 106, 107].
- KFRCs are coherent, meaning the reinforcing yarns are continuously connected by loops. In weft-knitting, an entire fabric layer can even consists of a single yarn. This coherence is very advantageous compared to short fibers and fiber mats.
- By stretching knitted fabrics, stiffness and strength is increased in the stretching direction. This way, mechanical properties of KFRCs can be tailored to their application. However, the anisotropy observed in KFRCs is less pronounced than for instance in woven fabrics. Again, this is a desirable aspect in many applications.
- Because of the holes in knitted fabrics, an interlocking effect of the knit layers occurs during processing. The individual knit layers cannot be distinguished after manufacturing. Interlocking of knit layers increases the interlaminar fracture toughness tremendously. The significance of the interlocking effect depends on the loop size and will be discussed in chapter 3 of the presented study.
- Cost considerations are of crucial importance in any material development. The knitting process itself is an established high volume technology. Production costs of KFRCs are higher than those of short fiber composites, but significantly lower than those of 3D structural composites and UD laminates. As mentioned before, almost any fiber/matrix combination is possible in KFRCs. Simple co-knitting of fiber and matrix yarns in the case of thermoplastic matrices represents an attractive low-cost production possibility. Furthermore, limited waste reduction or even net-shape processing is possible with KFRCs [18, 61, 66, 81].

1.5. Aim and structure of the thesis

As summarized in chapter 1.4, the state of the art of KFRCs has considerably advanced in the last years. However, the excessively large amount of knit structures and possible fiber/matrix combinations complicate the validity of general statements for the entire class of KFRCs. The presented work is focussed on two specific KFRCs, revealing similar knit structures but different fiber/matrix materials. The primary aim of the thesis was to study selected properties with respect to potential applications and to emphasize specific advantages of the investigated materials. The main objectives can be outlined as follows:

- to investigate the three dimensional shape and orientation of the reinforcement architecture in KFRCs and to couple it with macroscopic properties
- to study micro- and macroscopic failure behavior and to establish connecting links

- to determine the fracture toughness and impact performance of KFRCs
- to evaluate the environmental stability of the selected KFRCs
- to extract results relevant for the considered applications

The composites studied in this thesis can be characterized regarding their reinforcement structure and their material combination:

Knit structure. Contrary to most research on KFRCs, this work is focussed on knitted fabrics with a low areal loop density, i.e. large loops. The areal loop density influences interpenetration of knit layers in composites, manufactured from several stacked knitted fabrics. Large loops include large holes which offer more space for loops from other layers to penetrate across several layers. One of the working hypotheses of the presented study was that this interpenetration of knit layers is substantial for the delamination behavior of the investigated KFRCs. Additionally, large loops cause large fiber curvatures which improves their reinforcing quality.

Fiber/matrix materials. Two material combinations were studied, focussing different application fields:

- Carbon fiber reinforced poly(aryl-ether ether ketone), i.e. CF/PEEK, is used in high performance applications, such as load-bearing implants and aeronautic structural parts. The chemical and thermal stability of PEEK combined with the high mechanical properties of CFs at a low weight makes CF/PEEK suitable for both, biomaterials and high performance engineering applications.
- Glass fiber reinforced poly(ethylene-terephthalate), i.e. GF/PET. PET experiences increasing interest in the automotive industry. Being a thermoplastic matrix, significant shorter production cycle times can be reached compared to thermosets. GFs reveal good compression properties and are substantially less expensive than CFs.

As mentioned above, this work addresses micro- and macroscopic properties of KFRCs. In accordance with [46], a third level of observation, the mesoscopic level can be defined. While microscopic is referred to the interface and macroscopic to the complete structure, the mesoscopic level addresses fiber bundles and loops. With respect to this definition, the first chapter is devoted to mesoscopic properties, i.e. bundle shape and orientation in KFRCs. The following sections cover macroscopic behavior, namely failure behavior, fracture toughness and impact properties. Modifications of these characteristics caused by environmental exposure is discussed in the consequent chapter. A considerable part of the thesis treats the fiber/matrix interface in KFRCs, i.e. the microscopic level. Finally, the conclusions drawn from the investigation of the different levels of observation are discussed in a final chapter:

Chapter 2: Materials and manufacturing

This chapter describes materials and manufacturing of KFRCs which concern the entire scope of the thesis. Specific information, such as characterization methods, sample dimensions and experimental set-ups are given in the respective chapters.

Chapter 3: 3D-Structure of KFRCs

Shape and orientation of the knitted fiber bundles in a composite consisting of 8 knit layers was reconstructed to a 3D dataset based on 2D polished sections. The observed structure is discussed with respect to interpenetration of knit layers, bundle cross section and bundle axis deviation.

Chapter 4: Failure behavior I: Crack growth and fracture toughness in mode I

Using a modified compact tension (CT) test, out-of-plane crack growth, energy release rates and fracture toughness of knitted CF reinforced PEEK was investigated. Results indicated high fracture resistance combined with a damage tolerant behavior. A model describing crack propagation is proposed.

Chapter 5: Failure behavior II: Instrumented falling weight impact

CF/PEEK and GF/PET knits were subjected to impact experiments. High impact resistance compared to other composite materials was found. The fact that GF/PET knits dissipated twice as much impact energy as CF/PEEK is discussed. The impact failure damage zones are described by means of SEM micrographs.

Chapter 6: Influence of environmental exposure on the mechanical properties of KFRCs

CF/PEEK and GF/PET knits were immersed in water at elevated temperatures. With regard to their use in biomedical applications, CF/PEEK was additionally exposed to simulated body fluid (SBF). While no significant changes in the behavior of CF/PEEK were observed, GF/PET knits revealed a substantial decrease of its macromechanical properties. This evidence is discussed with regard to the considered applications.

Chapter 7: Interfacial properties of KFRCs investigated by means of the push-out method

A direct interface characterization method was applied on cut-outs of GF/PET knits. A new energy-based model to extract interfacial properties from measured push-out data is proposed. An automated analyzing tool was developed. The interface properties of environmentally exposed and unexposed GF/PET knits are presented.

Chapter 8: Final conclusions

The findings from the previous chapters are summarized. The conclusions drawn from observations on macro- meso- and microscopical level are discussed with respect to the potential applications of KFRCs.

This work arose in close collaboration with Joop de Haan [46] and Dirk Wilde [106]. An extended experimental study and a mechanical model describing the structure-property relations in KFRCs was described by de Haan [46]. Wilde [106] investigated and developed processing methods and forming tools for KFRCs. The results from this investigation were used to manufacture the KFRCs studied in this thesis.

The presented work and the above named collaborations were supported by Brite Euram, BRE2-0938, Project BE-7290.

2. MATERIALS AND MANUFACTURING

This chapter describes materials and manufacturing of KFRCs which concern the entire scope of the thesis. Specific information, such as characterization methods, sample dimensions and experimental set-ups are given in the respective chapters.

2.1. Fiber/matrix materials

As introduced in the previous chapter, the KFRCs studied in this work consisted of two different fiber/matrix combinations. In the case of CF/PEEK, reinforcing and matrix yarn were co-knitted, i.e. brought together immediately before forming the loop. In contrast, GF/PET was obtained as an intimately mixed, i.e. commingled yarn, consisting of fiber and matrix filaments.

Carbon fiber (CF) - Poly(ether-ether-ketone) (PEEK)

Carbon fibers are used because of their high tensile strength and modulus at a low density. In combination with PEEK, high interface strength is reached. Outstanding stability in hydrous solutions is a major advantage of CF/PEEK with respect to biomedical applications. Carbon fibers type “HTA 5131” were obtained from Tenax, Germany. The yarns revealed a linear density of 200 tex¹ and consisted of 3000 fiber filaments.

	Carbon fibers HTA 5131 (Tenax)	PEEK M (Hoechst)
tensile modulus [GPa]	238	4.1
tensile strength [MPa]	3950	100
elongation at break [%]	1.55	50
diameter [μm]	7.4	—
density [g/cm^3]	1.77	1.32
Poisson ratio ν_{12}	0.23	0.4
glass transition temperature T_g [$^{\circ}\text{C}$]	—	143
melting temperature T_m [$^{\circ}\text{C}$]	—	343

Table 2.1: Mechanical and physical properties of carbon fibers (CF) and poly(ether-ether-ketone) (PEEK) used in knitted CF fabric reinforced PEEK.

1. I.S.O. unit, describing mass per unit length of a yarn. 1 tex = 1 g/km

Outstanding characteristics of poly(ether-ether-ketone) (PEEK) are high thermal and chemical stability. Yarns made of 48 PEEK filaments were obtained from PEEK M, Hoechst, Germany. A PEEK grade with a relatively low melt viscosity (0.18 KNs/m^2) was used for better impregnation. The linear density of the yarn was 33 tex. Mechanical and physical properties of fiber and matrix material are presented in table 2.1.

PEEK and CF yarns were co-knitted with a ratio of 4:1, leading to a fiber volume content V_F of 52.5%

Glass fiber (GF) - Poly(ethylene-terephthalate) (PET)

Glass fibers exhibit lower mechanical properties than carbon fibers but are substantially less expensive than the latter. GFs are unsuitable for aeronautic applications because of their high density compared to CFs, but their better compression properties and low price represents attractive reinforcement for structural parts in land transportation and sports applications.

Poly(ethylene-terephthalate) (PET) is of interest for the automotive industry mainly because of its glass transition temperature being higher than polypropylene (PP) and its price being significantly lower than polyamide (PA). In combination with GF reinforcement, high mechanical properties can be reached.

Commingled GF/PET yarn was obtained from Vetrotex, France. The fiber volume content V_F of the yarn was 50% at a linear density of 730 tex. E-glass¹ fibers were used. PET was originally manufactured by DSM (the Netherlands) before being processed by Vetrotex. Amorphous and semicrystalline matrices were produced by controlling of the cooling rate (see section 2.2). Some important mechanical and physical properties of GFs, amorphous and semicrystalline PET are summarized in table 2.2.

1. Normal type of glass used for glass fiber reinforcement. "E" stands for electrical, as the composition exhibits high electrical resistance

	GF E-Glass (Vetrotex)	PET amorphous (DSM)	PET semicrystalline (DSM)
tensile modulus [GPa]	73	2.5	3.0
tensile strength [MPa]	3400	60	80
elongation at break [%]	3.3	300	70
diameter [μm]	19	—	—
density [g/cm^3]	2.6	1.33	1.37
Poisson ratio ν_{12} []	0.22	0.33	0.33
glass transition temperature T_g [$^{\circ}\text{C}$]	—	70	80
melting temperature T_m [$^{\circ}\text{C}$]	—	—	256
crystallinity [%]	—	0	35

Table 2.2: Mechanical and physical properties of glassfibers (GF), amorphous and semicrystalline poly(ethylene-terephthalate) (PET) used in GF knitted fabric reinforced PET.

2.2. Manufacturing of KFRCs

Knitted fabrics

The fabrics were weft-knitted on a circular knitting machine by Buck TSP GmbH, Germany. Using the contrary technique [62], low tension stress is applied to the fiber bundles, thus reducing fiber damage caused by the knitting process. The resulting fabrics revealed 132 stitches per row (course) and 4 stitches per inch. Stitch size in the fabric is measured directly after formation of the loop in the needles. All KFRCs investigated in this work were based on knitted fabrics with a stitch size of 8 mm leading to an areal loop density of $2.6 \text{ loops}/\text{cm}^2$ in the composite.

The structure of a weft-knitted fabric and definitions of the structural units is given in figure 2.1. For the sake of clarity, the term “stitch” is used for the textile fabric while “loop” is referred to the composite material.

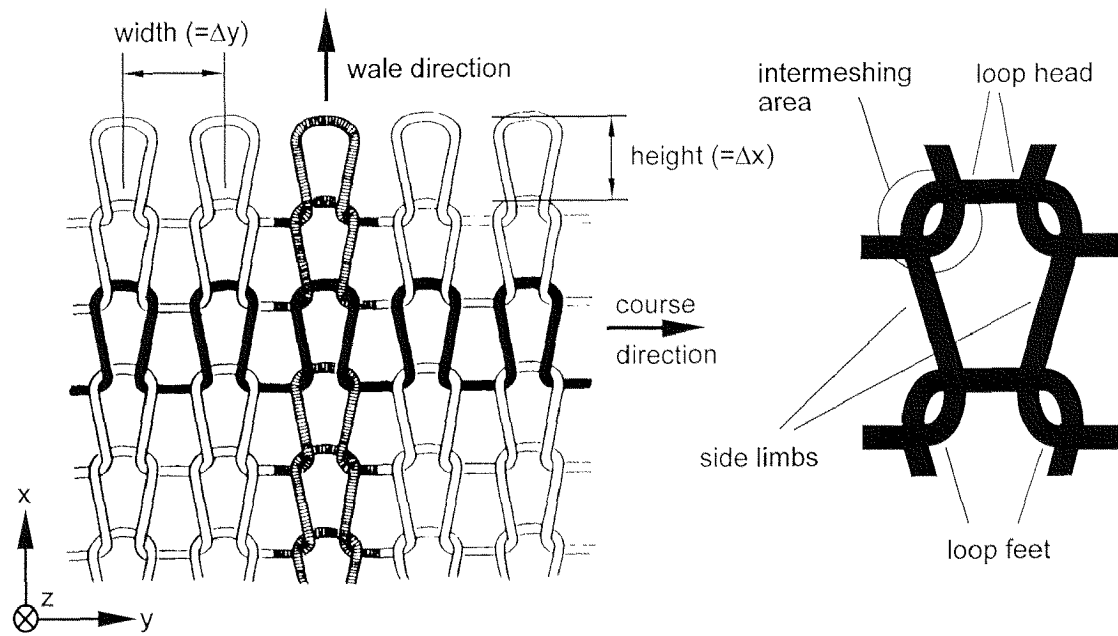


Figure 2.1: Structure of plain weft-knitted fabrics. The knitted fabrics studied in this work were produced on a circular knitting machine, applying the contrary technique [62]. The stitch size, measured directly after formation of the loop, was 8 mm.

Pre-stretching

Knitted fabrics can be pre-stretched in wale and course direction prior to consolidation. For a given stitch size of 8 mm, stretching states were defined after [106], as shown in table 2.3. The unstretched state was based on knitted GF reinforced PET showing a loop height of 5.4 mm at a loop width of 7.5 mm. This state was defined as the unstretched reference state and indexed as (100/100). The first index refers to 100% in wale, the second to 100% in course direction. For knitted CF reinforced PEEK studied in this work, an average stretching state of (140/60) was determined, i.e. stretching of 140% in wale and of 60% in course direction. This corresponds to a loop height of 7.5 and a loop width of 4.5 mm.

		loop height [mm]							
		3.2	4.3	5.4	6.5	7.5	8.6	9.7	10.8
loop width [mm]	2.3								200/30
	4.5					140/60	160/60	180/60	
	6.0				120/80	140/80	160/80		
	7.5			100/100	120/100	140/100			
	9.0			100/120	120/120				
	10.5		80/140	100/140					
	12.0	60/160							

Table 2.3: Definition of stretching states after [106] for a given stitch size of 8 mm. The knitted fabric reinforced PEEK investigated in this work revealed an average stretching state of (140/60). Reference: unstretched state (100/100), i.e. 5.4 mm / 7.5 mm.

Composite processing

CF/PEEK. Tubular fabrics from the circular knitted machine were wrapped around a steel mold ($300 \times 300 \times 5 \text{ mm}^3$), which was previously covered with copper foils (E-Cu, 0.3 mm) to facilitate release of the composite panels after consolidation. The knitted fabrics were also covered with copper foils and transferred into a hot-press (COLLIN 300 with vacuum chamber, Germany). A temperature of 420°C was maintained at a consolidation pressure of 30 bar for 30 min. The air pressure in the vacuum chamber was approximately 30 mbar during consolidation. All knitted CF reinforced PEEK panels studied in this work consisted of 4 and 6 double layers¹ (DL) of knitted fabric, leading to an average thickness of 1.31 and 1.81 mm, respectively.

GF/PET - semicrystalline matrix. Four unstretched tubular double layers were stacked, placed in a hot press (Laufer, Germany) and consolidated to flat panels of $700 \times 500 \times 1.8 \text{ mm}^3$. Consolidation temperature of 280°C was maintained at 20 bar for 20 min. The panels were cooled at $30^\circ\text{C}/\text{s}$ to a temperature of 30°C , leading to a semicrystalline (35%) matrix.

GF/PET - amorphous matrix. Knitted GF reinforced PET, exhibiting an amorphous matrix, was obtained from “Institut für Verbundwerkstoffe”, IVW, Germany. The panels consisted of 3 DL (thickness = 1.35 mm) and were manufactured using a double belt press (DBP). Handling and processing conditions are described in [112].

1. Circular knitting machines produce tubular fabrics. Therefore, double layers (DL) were chosen as the layer unit.

3. 3D-STRUCTURE OF KFRCs

3.1. Introduction

It is evident that the mechanical properties of KFRCs strongly depend on the three dimensional (3D) structure of their reinforcement. This structure, i.e. the shape and orientation of the reinforcing fiber bundles, is not only defined by the knitting process. Other factors, such as pre-stretching of the fabric and interpenetration of knit layers, influence the 3D reinforcement structure of KFRCs:

- Weft-knitted fabrics are coherent, i.e. continuously connected by loops. The fabric is highly flexible and can be stretched in course and wale direction prior to consolidation (see chapter 2). This drapability can be considered as the in-plane liberty of action in knitted fabrics. At a constant stitch size (controlled by the knitting process), different stretching states cause different loop shapes (determined in the composite). Consequently, mechanical properties of KFRCs depend on the pre-stretching state of the knitted fabric.
- The large loops (areal loop density = 2.6 loops/cm^2) of the KFRCs investigated in this work, were one of their key characteristics. Consolidation of a single CF/PEEK knit layer with a fiber volume content V_F of 52.5% lead to a composite with holes, because of insufficient matrix available to fill the holes within the loops. When stacking several knit layers, this space can be filled with fiber bundles from other layers. At a given V_F , a minimum number of layers is required to reach a dense composite. The relation between V_F and the number of knit layers is discussed in [46]. The complementary interpenetration of loops from different knit layers not only enables dense composites, it also introduces an out-of-plane orientation of the layers upon consolidation. As introduced in chapter 1, this out-of-plane orientation and the resulting interlocking of loops is assumed to reduce delamination sensitivity and to increase impact properties.

The purpose of this chapter was to study shape and orientation of the loop forming fiber bundles in knitted CF reinforced PEEK in order to gain a better understanding of its mechanical behavior and to obtain basic data needed for mechanical models of KFRCs.

The orientation and shape of CF bundles in KFRCs was studied by reconstructing their 3D structure using a large amount of 2D polished sections. In contrast, Mayer [18] investigated the loop orientation of KFRCs using X-ray analysis of co-knitted copper filaments. The main differences of the two methods are summarized in table 3.1.

X-ray analysis of cknitted copper wire	3D structure based on 2D polished sections
<ul style="list-style-type: none"> • determination of 2D loop orientation • fast data acquisition: used for quality control and analysis of shaped parts • curvature artifacts induced by different mechanical properties of copper wire and carbon fiber bundles • conclusions on fiber bundle orientation in function of stretching ratio 	<ul style="list-style-type: none"> • determination of 3D loop orientation • determination of 3D bundle shape • performed on exemplary samples and small investigation sizes • reflects the real structure: interpenetration of knit layers, bundle cross section • conclusions on fiber impregnation, porosity, matrix distribution, mechanics of KFRCs

Table 3.1: Aim and scope of two different methods to investigate the loop structure in KFRCs. X-ray is predominantly applied to study stretching and deformation effects, e.g. in shaped parts. By reconstructing polished sections to a 3D structure, additional information on the loop shape is obtained.

Another method, often applied to characterize short fiber reinforced composites is the analysis of the fiber orientation distribution using polished sections and image analysis [113, 114]. The angle at which the fibers are cut by the polishing disc can be determined and used to calculate the fiber orientation distribution. This method is particularly suitable for short fiber composites because their properties can be determined from the fiber orientation distribution. Investigation of the fiber orientation distribution and its correlation with some mechanical properties of KFRCs was performed in [18]. However, shape and orientation of fiber bundles cannot be reconstructed from a fiber orientation distribution analysis.

3.2. Methods

3.2.1. Sample manufacturing

Knitted CF reinforced PEEK was manufactured by hot pressing as described in chapter 2. A flat panel composite of 1.31 mm thickness and a stretching ratio of (150/60), according to the definitions given in chapter 2.2 was obtained. A sample of 25 mm width, and 30 mm length was cut from the panel and embedded in epoxy resin (Bisphenol-A-epichlorhydrine, Struers, Switzerland).

3.2.2. Monitoring of polished sections

The sample was polished using a grinding machine (Struers, Switzerland). The resulting cross section, oriented perpendicular to wale direction (fig. 3.1), was monitored digitally by means of confocal laser scanning microscopy at a laser wavelength of 543 nm

(CLSM, Zeiss LSM 410). Subsequently, the sample was subjected to further polishing in order to remove $56\ \mu\text{m}$ in wale direction at every polishing step. 178 polished sections (fig. 3.1, A) were recorded, every section consisting of 14 CLSM images (B), covering a sample range of $10\ \text{mm} \times 25\ \text{mm} \times 1.3\ \text{mm}$. In order to assure correct positioning, a hole of $0.2\ \text{mm}$ diameter (C), drilled in the embedding epoxy resin, served as a reference point.

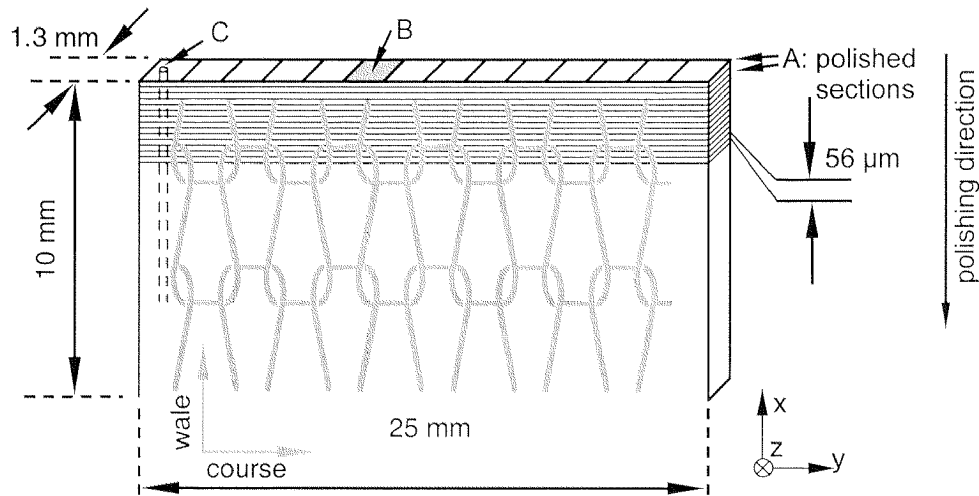


Figure 3.1: Recording of polished sections was performed by means of confocal laser scanning microscopy (CLSM). One polished section (A) consisted of 14 single CLSM images (B) covering the entire sample cross section of $1.3\ \text{mm} \times 25\ \text{mm}$. A total of 178 polished cross sections were recorded. A hole of $0.2\ \text{mm}$ in diameter (C) served as a reference point to assure similar positioning after every polishing step.

3.2.3. Stacking of cross sections

CLSM images (fig. 3.2) were pasted to an entire cross section (fig. 3.3). The cross sections were compiled to a stack with the aid of the program “NIH Image” (National Institute of Health, USA) in order to browse through the sections which was necessary to track fiber bundles through the composite.

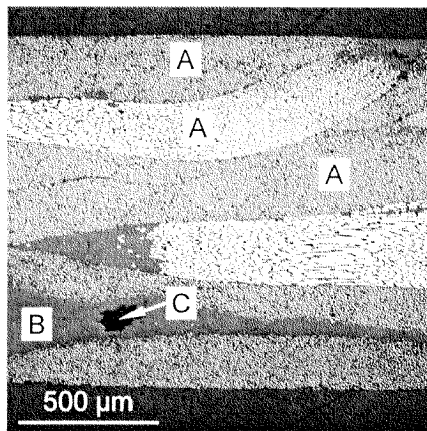


Figure 3.2:

Polished cross section of knitted CF reinforced PEEK, perpendicular to wale direction:

A: Carbon fiber bundles

B: PEEK matrix

C: Voids

The different brightness of fiber reflections is caused by different angles at which the fibers were cut by the polishing disk. Bundles were found to be closely packed, i.e. only separated by a very thin matrix layer.

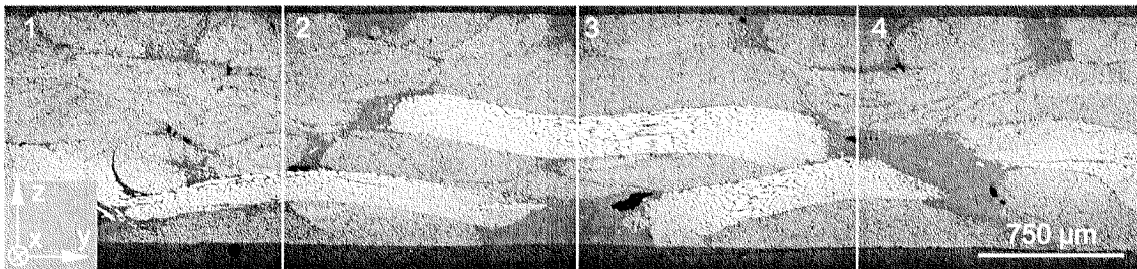


Figure 3.3: *Polished cross section, pasted from 4 single CLSM images. An entire cross section consisted of 14 CLSM images, covering the sample width of 25 mm.*

3.2.4. Identification of fiber bundles

Fiber bundles were manually identified and marked to trace their shape and orientation (fig. 3.4). Automatic bundle identification was not possible, mainly because of two reasons:

- Contrast between fiber bundle and surrounding matrix was not distinctive enough.
- Lack of a clear dividing line between fiber bundle and matrix or neighboring fiber

Fiber bundle cross sections belonging to the same knit layer were marked with the same color index. Identification was limited to two knit layers, assumed to be representative for the entire sample. Figure 3.4 shows a cross sections with digitally marked fiber bundles. Bundle cross sections from layer 1 of 8 (surface) and from layer 4 of 8 (bulk) were marked on a width of 9.5 mm, i.e. approximately 40% of the sample width. The investigated height was 10 mm, i.e. 178 cross sections with an average distance of 56 μm between two sections (fig. 3.1).

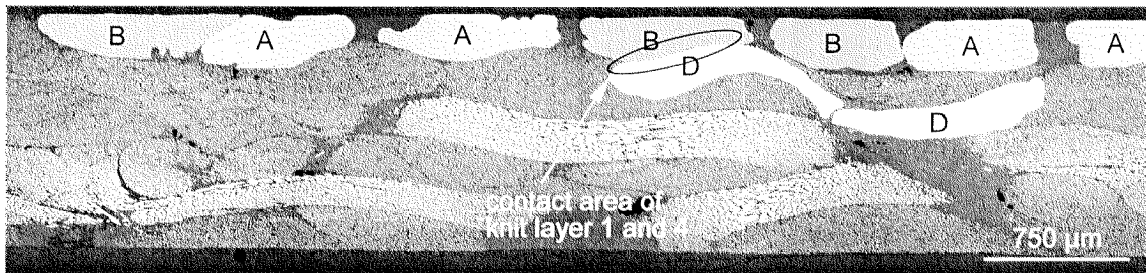


Figure 3.4: Fiber bundles were manually marked to trace their shape and orientation. Bundle D originates from knit layer 4, i.e. from the middle of the sample, while A and B are surface bundles from two different loops of knit layer 1. The fact that knit layer 1 and 4 can be in direct contact underlines the inexistence of clearly defined interlaminar planes and is the result of effective interpenetration in KFRCs with large loops.

3.2.5. 3D reconstruction

The completed stack of 178 sections was reconstructed to a 3-dimensional data set using the program IMARIS (Bitplane AG, Switzerland). The surfaces between the cross sections were calculated by means of the marching cube method [115]. A 3D low pass filter was applied to smooth the calculated bundle surfaces in order to reduce data. The low pass filter introduced some image artifacts at locations where bundle thickness was very small.

3.3. Results and discussion

3.3.1. Cross sections

Cross sections used for 3D reconstruction of carbon fiber bundles are shown in figure 3.5. The white areas represent cross sections of adjacent side limbs (see figure 2.1) at different heights. Section 1 is close to the loop head, while section 4 is at the bottom of the loop, before the side limbs turn into the loop feet (see also figure 3.6).

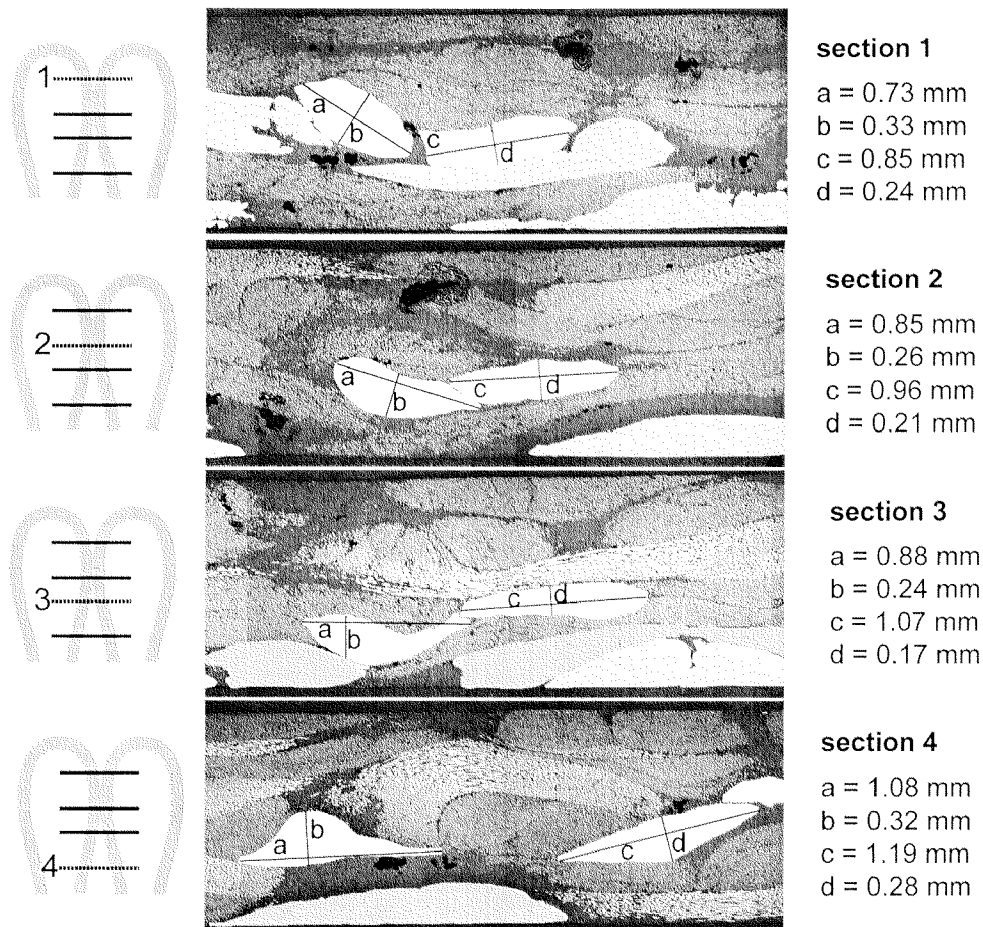


Figure 3.5: CLSM images with manually marked bundle cross sections of a bulk bundle. The white areas in this figure are sections from the side limbs of the bundle presented in figure 3.6. The shape of side limb cross sections differs much from idealized circular cross sections. The average length of the longer bundle section axis (= side limb width) was found to be 0.95 ± 0.15 mm, the shorter axis (side limb thickness) measured 0.26 ± 0.05 mm. This corresponds to a ratio of 3.7/1, a value that characterizes the flatness of the side limbs

Figure 3.5 illustrates the fact that cross section of side limbs differ much from idealized circular shapes. The same result was found for loop heads and loop feet. However, flatness of the side limbs, characterized by the ratio bundle width/height was more pronounced than flatness of loop heads and feet. The flatness generally increased with increasing distance from intermeshing areas. In the intermeshing of bulk layers, the bundles exhibited a width/height ratio of approximately 2.5/1, corresponding to a more circular cross section than in other parts of the loops. This can be understood considering the mutual stabilization of bundle cross sections caused by interlooping.

When comparing the cross sections from bundles of the of surface and bulk layers, it was found that bundles located at the surface of the composite samples were flatter and

therefore wider. The range of bundle width and bundle thickness measured in surface and bulk layers are given in table 3.2. Considering the fact that surface layers are in direct contact with the steel mold during consolidation, the more emphasized planarity in surface layers could be expected.

	surface layers	bulk layers
bundle width [mm]	1.1 - 1.3	0.9 - 1.1
bundle thickness [mm]	0.25 - 0.27	0.26 - 0.4

Table 3.2: Range of bundle width and thickness in surface and bulk layers determined from cross section analysis. Bundles from surface layers were found to be more planar which can be understood considering the direct contact of the surface layers with the steel mold during consolidation.

3.3.2. Single bundle

A 3D reconstructed bundle from the bulk (knit layer 4) of the studied knitted CF reinforced PEEK sample is shown in figure 3.6. Loop width and height are indicated according to the definitions given in chapter 2, figure 2.1. The *z-spacing* of a loop is defined by the largest bundle axis extension in z-direction, a value that characterizes the waviness of a knit layer in out-of-plane direction. In contrast to *z-spacing*, *z-spread* refers to the largest out-of-plane extension of loop surfaces, i.e. the largest z-distance of two points belonging to the same loop or knit layer (fig. 3.6).

The knitted CF reinforced PEEK investigated in this work was stretched in wale direction. Its stretching state was (140/60), i.e. revealed a loop width of 4.5 mm and a loop height of 7.4 mm (definitions see table 2.3).

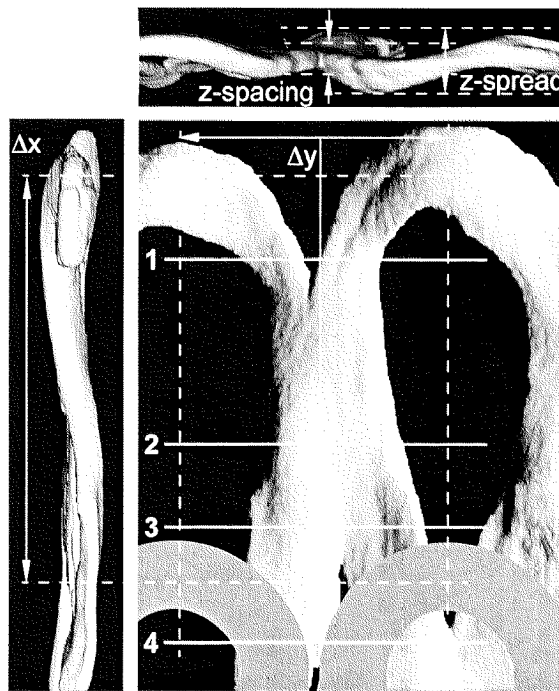


Figure 3.6:
3D orientation and shape of carbon fiber bundles in knitted fabric reinforced PEEK. 150 cross sections were analyzed to calculate the 3D structure of the presented bundles which were located in the bulk of the flat panel. The presented structure is stretched in wale (140/60). Average dimensions for bulk loops are:

$$\Delta x = 7.4 \text{ mm (loop height)}$$

$$\Delta y = 4.5 \text{ mm (loop width)}$$

$$\Delta z_{\text{spacing}} = 0.6 \text{ mm}$$

$$\Delta z_{\text{spread}} = 1.0 \text{ mm (see figure 3.9)}$$

Lines numbered from 1 to 4 refer to the cross sections shown in figure 3.5. Lower bundle row is drafted in grey.

3.3.3. Knit layers

In figure 3.7 an overview of the studied surface and bulk bundles is given as a view on the x-y plane. As mentioned above, smoothing of data using a 3D low pass filter introduced some image artifacts. This occurred only at location where the studied bundle was thin, i.e. consisted only of a few pixel. The single bundle presented in figure 3.6 was calculated with less smoothing, therefore the image artifacts could be reduced.

Knit layers A and B were located at the surface, layers C and D in the bulk of the studied KFRC sample. The more pronounced flatness of the surface layer (fig. 3.9) was caused by its direct contact with the steel mold and the resulting limited liberty of action throughout hot pressing. For the same reason fusing of side limbs was observed predominantly in surface layers (fig. 3.7).

The bundle axis of the loop heads was found to be well approximated by circles (fig. 3.7), connected with side limbs, approximated by straight lines. Figure 3.8 shows details from surface and bulk bundles in a perspective view.

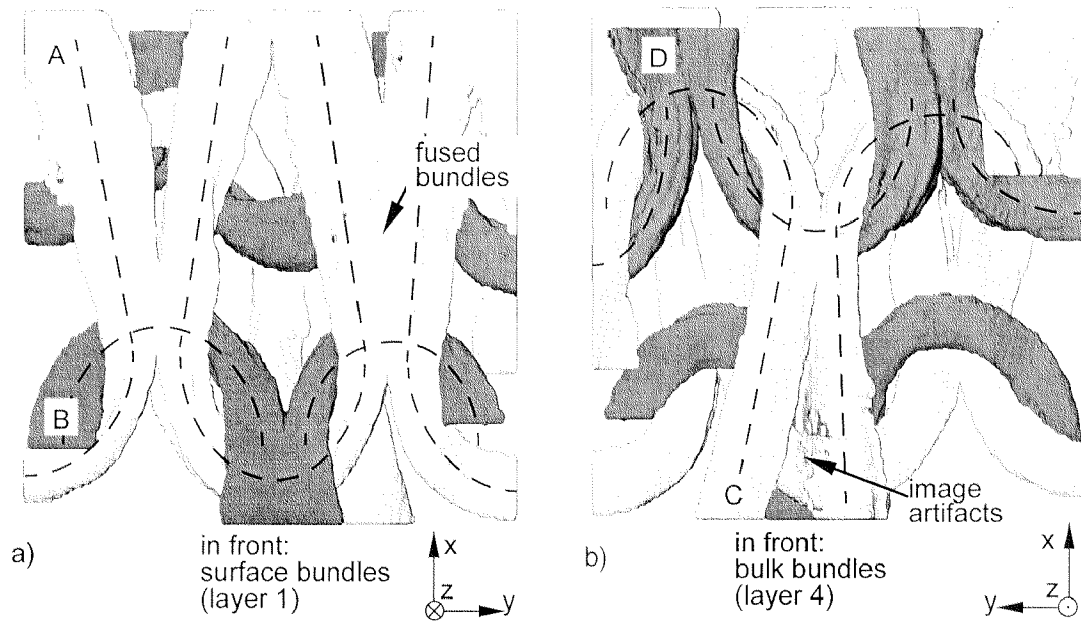


Figure 3.7: 3-D reconstruction of knitted carbon fibre bundles in a PEEK matrix (view on x - y plane). The images show surface (knit layer 1 of 8) and bulk bundles (layer 4 of 8). Loop geometry can be approximated with circular loop heads connected by straight side limbs. Side limbs of adjacent bundles were observed to fuse together under the effect of pressure and temperature throughout hot pressing.

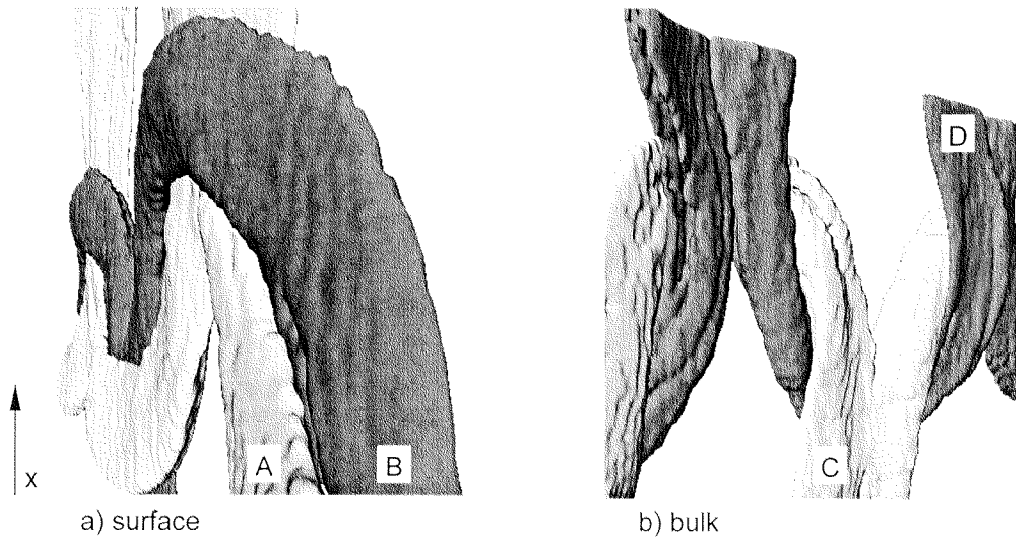


Figure 3.8: Surface (layer 1) and bulk loops (layer 4) in a perspective view. Near the intermeshing contact areas, bundles were observed to be less planar than in the side limbs. The bundle axis of loop heads was found to be approximately circular (see also figure 3.7).

The same surface and bulk layers as in figure 3.7 are shown as a view on the y-z plane (course is horizontal) in figure 3.9 a-b. Despite the fact, that two other knit layers (2 and 3) are located between surface and bulk layers, they showed direct contact areas with each other (see also figure 3.5). To better distinguish between surface and bulk layers, they are presented separately in figure 3.9 b, i.e. with more z-distance between them than in reality (figure 3.9 a).

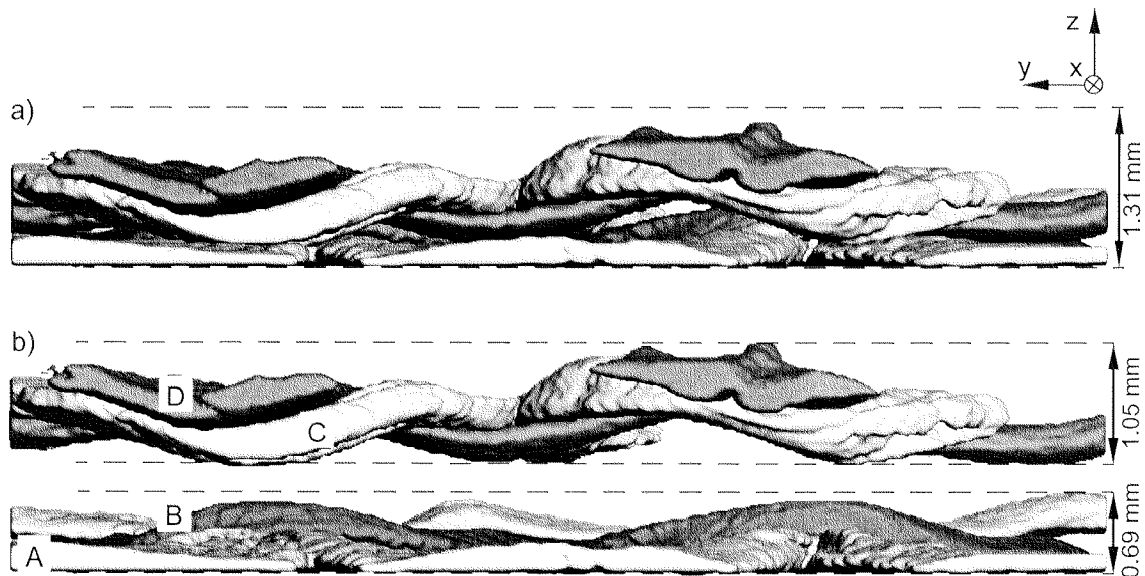


Figure 3.9: View on the y-z plane, i.e. course is horizontal. The first 3D plot (a) reproduces real proportions, the dashed line represents the thickness of the studied sample consisting of 8 knit layers. Considering the fact that two additional layers in between the presented surface and bulk layer are not drawn, it becomes clear that distinctive interlaminar planes do not exist in the studied knitted fabric reinforced composite. Loops belonging to different knit layers interpenetrate each other, thus suppressing interlaminar planes. To better distinguish the surface from the bulk layer, they are presented separately in (b). The z-spread of the knit layers was found to be 1.5 times higher in bulk layers than in surface layers. One bulk layers is spread over approximately 80% of the thickness of a sample consisting of 8 knit layers.

The theoretical thickness of a single knit layers is obtained by dividing the total sample thickness by the number of knit layers, i.e. 0.163 mm in the case of the investigated composite. The measured z-spread of a single knit layer located in the bulk was 1.05 mm, i.e. 6.5 times higher than its theoretical thickness. This means that a single bulk layer was spread in approximately 80%, a surface layer in 50% of the total sample thickness.

3.3.4. Quantitative analysis

As observed in figure 3.9, a difference in the z-spread of surface and bulk layers was found. To get a quantification across all knit layers, the z-spread of loop heads was measured (for definitions see figure 3.10). The studied composite volume contained many loop heads, but only very few entire loops. Therefore, the z-spread of loop heads instead of entire loops was investigated in order to increase the statistical relevance of the results.

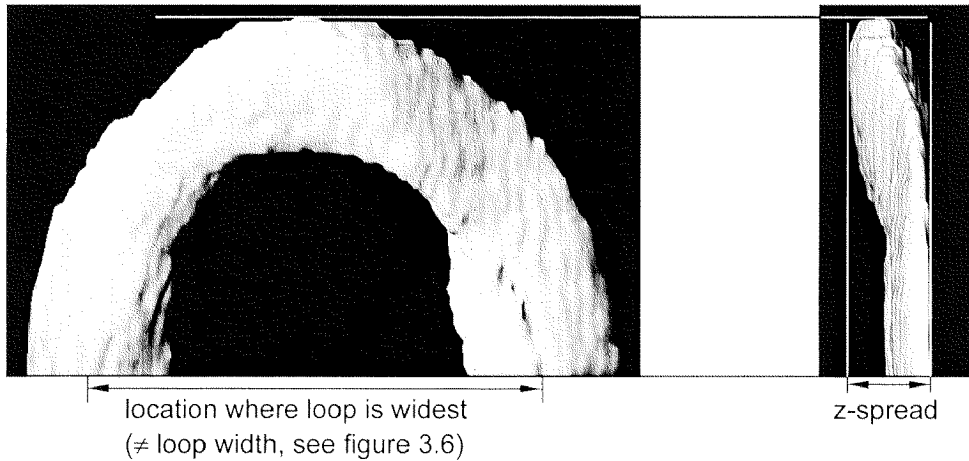


Figure 3.10: Definition of the z-spread of loop heads. This value could be determined for more than 20 loop heads within the investigated composite volume whereas measuring of z-spread of entire loops was possible only for very few loops, because it requires the entire loop geometry.

23 loop heads from all 8 knit layers were investigated to determine the z-spread of loop heads. Results were plotted in function of knit layers (fig. 3.11).

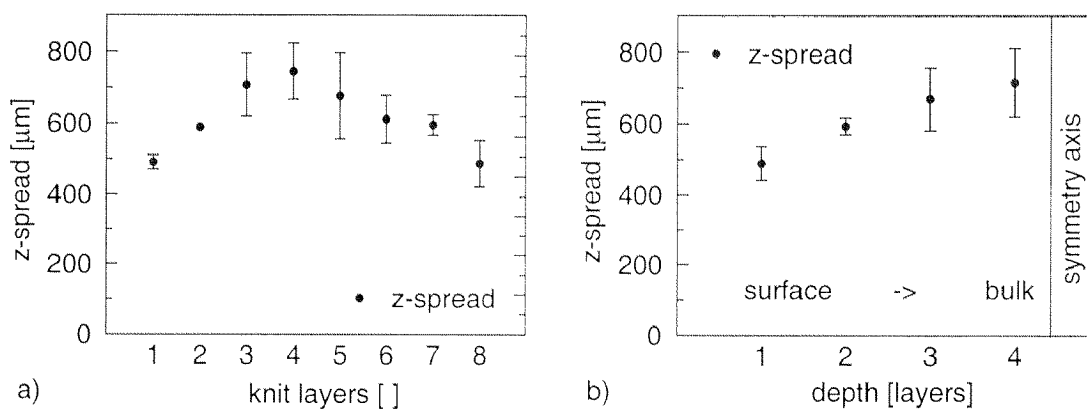


Figure 3.11: z-spread of loop heads from all 8 single knit layers of the investigated composite area (a). Results show symmetry with respect to the middle of the sample (layer 3, 4). Therefore, and to increase statistical relevance, results of layer 1 and 8, layer 2 and 7, etc. were averaged and plotted versus the sample depth of a symmetrical knitted fabric reinforced composite ($n > 4$).

Two characteristics can be determined from the quantitative analysis of the z-spread of loop heads across all 8 knit layers:

- A symmetrical behavior with respect to the middle of the sample depth was observed.
- The z-spread of loop heads increased from 0.49 mm (surface) to 0.71 mm (bulk). This is in accordance with the z-spread of entire surface (0.69 mm) and bulk(1.05 mm) layers (see figure 3.9), which corresponds to the same relative increase.

3.4. Conclusions

The following results summarize the 3D analysis of knitted CF reinforced PEEK:

- The in-plane bundle orientation was found to be well approximated by circles connected with straight lines (fig. 3.7).
- Planar bundles were observed. The highest ratio thickness/width was found in the side limbs ($\sim 4/1$) of the loops, the lowest in the intermeshing areas ($\sim 2.5/1$).
- Bundles from surface layers were found to be flatter and wider than bundles from bulk layers. This is a consequence of direct contact with the steel mold during consolidation (fig. 3.5, fig. 3.9). Adjacent side limbs fused together under the effect of pressure and temperature throughout hot pressing (fig. 3.7)
- The investigated bulk layer revealed a z-spread of 1.05 mm, i.e. it was spread in approximately 80% of the total sample thickness. The surface layer showed a smaller z-spread of 0.69 mm which corresponds to 50% of the total sample thickness.
- The z-spread of loop heads was symmetric with respect to the middle of the sample depth. It increased from 0.49 mm (surface) to 0.71 (bulk).

From these findings it can be concluded that distinctive interlaminar planes do not exist in the studied KFRC. The fact that a single bulk layer is spread over more than 6 times of its theoretical thickness confirms the assumption that an effective interpenetration occurred during consolidation. Because of this interpenetration, interlaminar fracture in between the knit layers is assumed to be very unlikely. In fact, delamination caused by shear stresses in perforation impact was found to occur across several knit layers (chapter 5).

The cross section data of fiber bundles and the loop geometry, observed as circular loop heads connected by straight side limbs, served as input for a mechanical model of KFRCs proposed by de Haan [46]. He found that both, the geometry of the loop and the dimensions of the fiber bundle cross sections are major structural parameters which determine the material response. This leads to the conclusion that the knowledge of the 3D structure is crucial for the description and prediction of the mechanical properties of KFRCs.

4. FAILURE BEHAVIOR I: CRACK GROWTH AND FRACTURE TOUGHNESS IN MODE I

4.1. Introduction

Various researchers studied interlaminar fracture, considering delamination as one of the most fragile properties of composite materials [36, 116-118]. Contrary to most 2D composites, the knitted fiber reinforced composite (KFRCs) studied in this work is not sensitive to delamination. Throughout consolidation the knit layers interpenetrate each other, leading to a composite material without distinctive interlaminar fracture planes. It was shown in chapter 3 that a single bulk knit layer in a KFRC consisting of 8 layers was spread over 80% of the sample thickness. This intense interpenetration across several knit layers excludes the existence of distinctive interlaminar fracture planes observed in most other 2D textile composites. Because of the absence of interlaminar planes, interlaminar fracture of KFRCs is strongly suppressed and, for the same reason, can hardly be investigated using common techniques such as double cantilever beam (DCB) or end notched fracture (ENF). Prior investigations on DCB experiments with knitted reinforced composites led to the conclusion that the fracture path does not remain between two knit layers. After a very short crack propagation length, bending failure instead of interlaminar crack propagation was observed [119].

Because of the interpenetration of knit layers, delamination is not considered to be one of the limiting failure characteristics of KFRCs. Out-of-plane, i.e. intralaminar fracture is assumed to be of higher importance to characterize failure properties and damage tolerance of KFRCs. This chapter is focussed on the mechanisms of out-of-plane crack growth in course and wale, investigated quantitatively and qualitatively. The latter requires the application of fracture mechanics to knitted fabric reinforced composites, the former was done using thermography and scanning electron microscopy (SEM). The aim of the study was, (a) to obtain values for the intralaminar fracture toughness of KFRCs and, (b) to gain an understanding of the mechanisms of crack initiation and propagation starting from a notched tip. Notches occur in many practical applications of composites and are likely sites for crack initiation. Understanding the response of a composite part to the presence of load and notches is important in order to select the appropriate design and material for a specific application.

The definition of loading angles relative to the reinforcing knit structure is given in figure 4.1. In the present work, two cases were studied: Load applied in course lead to cracks propagating in wale, defined as 90° testing (fig. 4.1). Consequently, 0° testing is referred to load in wale and crack propagation in course.

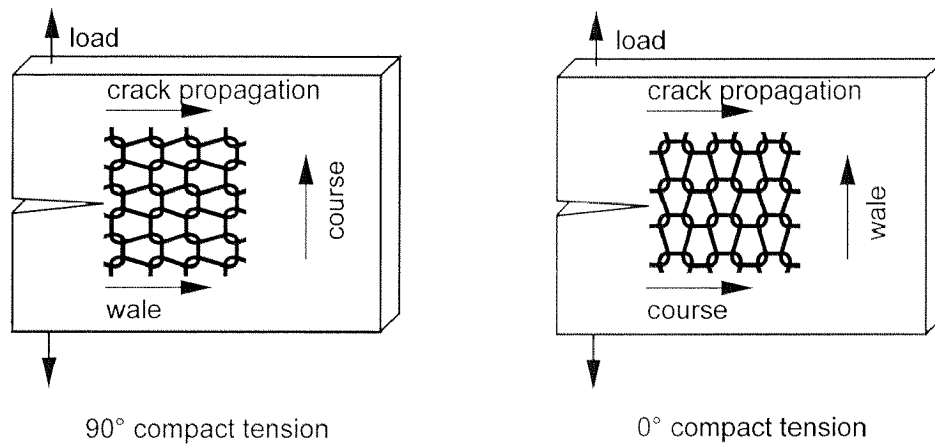


Figure 4.1: Definition of loading angles relative to the knit structure. Two cases were distinguished: load applied in course, leading to crack propagation in wale and vice versa.

Energy release rates G_{IC} and fracture toughness K_{IC} of knitted CF reinforced PEEK were determined in a modified compact tension experiment using linear fracture mechanics. Plastic deformation was neglected, because tensile and bending behavior of knitted CF reinforced PEEK was found to be predominantly elastic up to failure [46].

4.2. Methods

4.2.1. Thermography

Thermography is used to investigate and control composite manufacturing and quality [120-124]. It is applied in non-destructive testing (NDT), e.g. quality control of the final composite part (active thermography) and to study heat development in damage propagation in destructive mechanical tests (passive thermography). In this work, both methods were used. Passive thermography was applied to monitor heat emission of crack growth and active thermography to study the damage zone after testing.

Passive thermography

The fracture process was monitored online using passive thermography in order to study the damage development in mode I compact tension experiments. Passive thermography is based on the fact, that fracture processes lead to a local temperature increase. A thermal wave from the damage location to the sample surface increases the temperature at the surface which leads to the emission of a temperature dependent radiation according to Planck's law. This radiation is monitored by an infrared (IR) thermocamera and converted into an absolute temperature scale.

To study the failure process throughout compact tension testing, sequences with a maximum of 8 passive thermographs per second were recorded. The first thermograph recorded at the beginning of the experiment was subtracted from the followings in order to extract effects caused by the failure process.

Active thermography

Active thermography is applied to detect material defects, such as cracks and pores. The sample is irradiated with an external IR source. The dynamics of the reflected radiation distribution is measured by an infrared thermocamera. In the present study, this was done using an IR source with modulated radiation. The harmonic modulated, i.e. sinusoidal, radiation from the external IR source generates thermal waves at the surface of the sample from where propagation into the material occurs. This thermal wave is reflected at defaults (cracks, porosities, etc.) in the sample because of the changing physical heat parameters. The interference of incoming and reflected waves leads to a harmonic oscillating radiation pattern on the object surface.

Phase- and magnitude thermographs

Every pixel in the thermograph is calculated from a thermal signal from its corresponding location on the sample surface. The resulting thermograph of 272 x 136 pixels can be displayed based on magnitude or phase signal of the thermal wave.

The magnitude is determined from a signal difference, therefore, in a magnitude thermograph, the reflected ambient radiation is eliminated. The thermograph calculated from the phase is independent of surface effects like inhomogenous illumination, because it contains an additional division of the signal differences. Examples of each mode are presented in figure 4.2. Both images were taken of the same compact tension specimen.

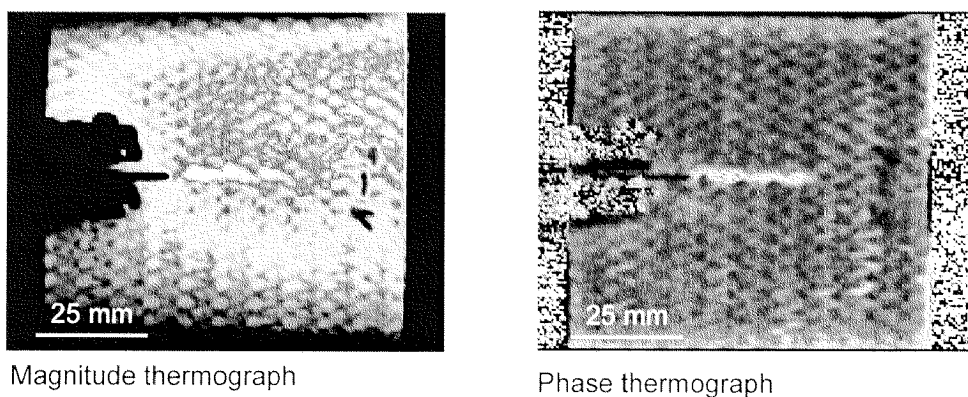


Figure 4.2: Magnitude (left) and phase thermographs (right). Elimination of the ambient radiation and calculation of the absolute surface temperature are advantages of magnitude thermographs. To avoid temperature gradients caused by non perpendicular irradiation, phase thermographs were used.

Experimental setup

An infrared thermocamera (Thermovision 900, Agema, Sweden) with a spectral wavelength range of 8 to 12 μm , a sensitivity of $\pm 0.08^\circ\text{C}$ and an accuracy of $\pm 1^\circ\text{C}$ was used. Thermographs containing 272 x 136 pixel were calculated. The camera was covered with aluminium paper to minimize the influence of ambient thermal radiation. The distance between sample surface and lens was 110 mm. The entire experiment was monitored online using a video cassette recorder (PANASONIC VCR AG-7350). A scheme of the experimental setup is presented in figure 4.3.

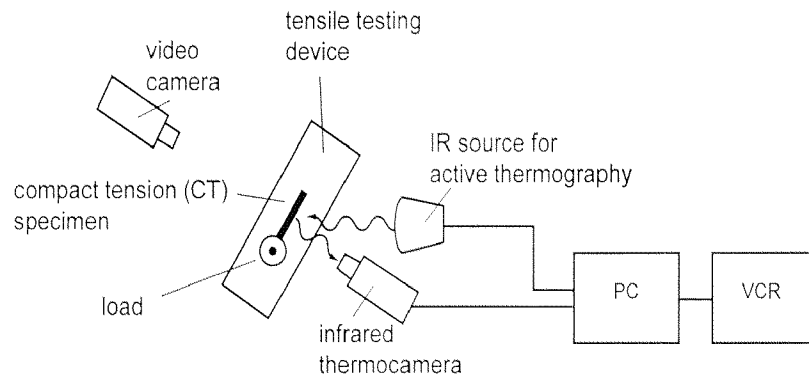


Figure 4.3: *Experimental setup of thermographic analysis in compact tension experiments of knitted CF reinforced composites. Whereas passive thermography was used online to study heat development of crack propagation, active thermography was performed on tested specimens to investigate the damage zone.*

4.2.2. Modified compact tension (CT) test

Manufacturing of compact tension samples

Knitted CF reinforced PEEK with a fiber volume fraction of 52.5% was manufactured as described in chapter 2.2. Panels consisting of 6 DL of knitted CF fabric leading to a thickness of 1.81 ± 0.05 mm were obtained. Compact tension samples of 136 mm length and 80 mm width were cut from the panels using a diamond coated circular saw (Reinhard, Switzerland). Holes of 12 mm diameter were drilled using a PCD (polycrystalline diamond) drill (HAM-PRAEZISION, Switzerland). A notch of 22 mm length and 0.22 mm width was brought in using a wire diamond saw (Well 3242, Switzerland).

Mixed mode device by Benitz and Richard [125]

Mode I energy release rates (G_{IC}) were determined by means of a modified mixed mode device designed by Benitz and Richard [125]. This device offers the possibility to perform experiments in mode I, mode II and mixed modes. However, in this work only mode I energy release rates were studied.

Technical schemes and pictures of the testing device used in compact tension are shown in figure 4.4. The testing device was bedded with needle bearings in order to reduce friction to a minimum.

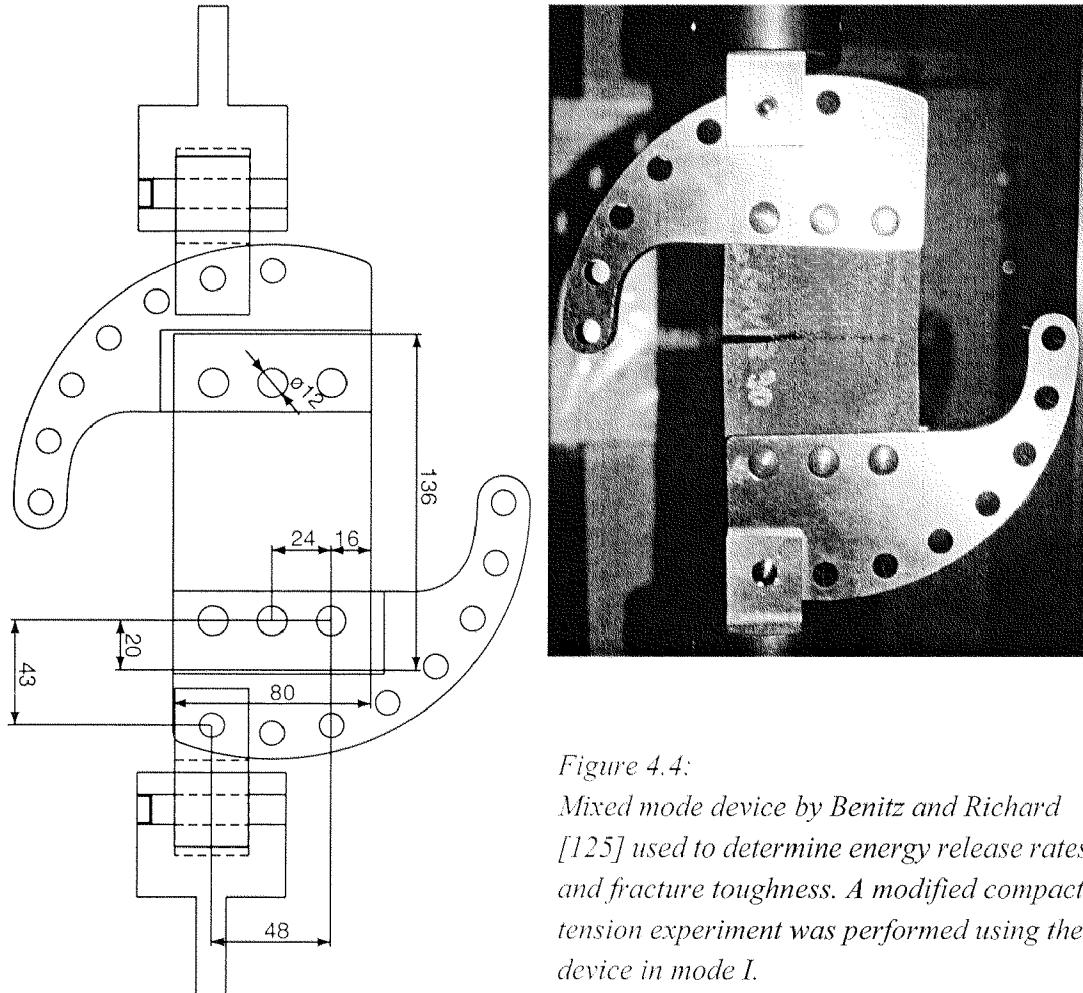


Figure 4.4:
Mixed mode device by Benitz and Richard [125] used to determine energy release rates and fracture toughness. A modified compact tension experiment was performed using the device in mode I.

The compact tension samples were loaded in a tensile testing apparatus (Zwick 1456, Germany) applying a crosshead speed of 0.5 mm/min. Displacement was recorded at the load points. Load point displacement was used to calculate the energy released throughout crack propagation. The compliance of the mixed mode device and of the tensile testing apparatus (= system compliance) were taken into account by measuring force vs. displacement using a very stiff steel sample and subtracting this curve from the actual experimental data (fig. 4.5). The elastic behavior of the knitted CF reinforced PEEK compact tension samples was addressed in the experimental relation between crack length and sample compliance described below (compliance method).

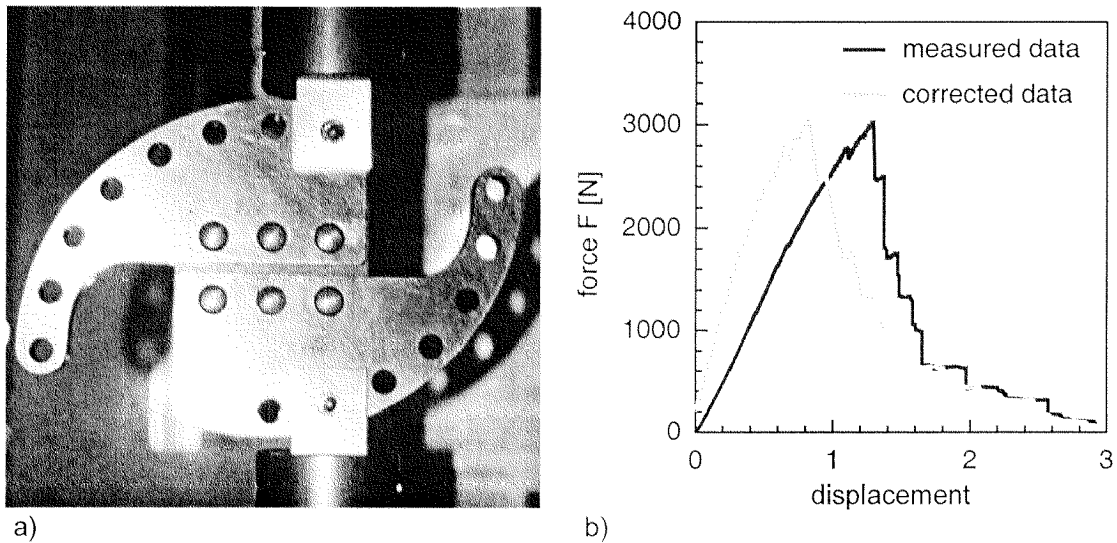


Figure 4.5: Measuring (a) and subtracting (b) of system compliance from the actual experimental data. The system consists of tensile testing apparatus and mixed mode device. The system compliance was measured using a very stiff steel sample (a). A force-displacement plot before and after system compliance correction is presented in (b).

Compliance method

Most fracture mechanics methods require the in-situ measurement of the crack length during crack propagation. However, crack propagation in knitted CF reinforced PEEK was wavy and accompanied by crack splitting (fig. 4.6). Crack splitting occurred to different extents on both sample surfaces. Therefore, calculation of energy release rates on the basis of a measured crack length would lead to errors. A better approach was found in the compliance method. An experimental relationship between elastic sample compliance and different notch lengths was determined. This way, an apparent crack length could be deduced from the compliance at every point of the load-displacement curve. The apparent crack length is the theoretical concept of a single, linear defect, entirely responsible for the increasing compliance. If crack splitting didn't occur, the apparent crack length would correspond to the real, linear crack length. In the case of crack splitting, the apparent crack length is a combination of macroscopic crack length and microscopic crack splitting, thus taking into account both effects. Since linear fracture mechanics is based on the assumption of a single, linear crack, the apparent crack length is the correct value to calculate energy release rates G_{IC} . For the sake of simplicity, the apparent crack length will be called *crack length a* in this work.

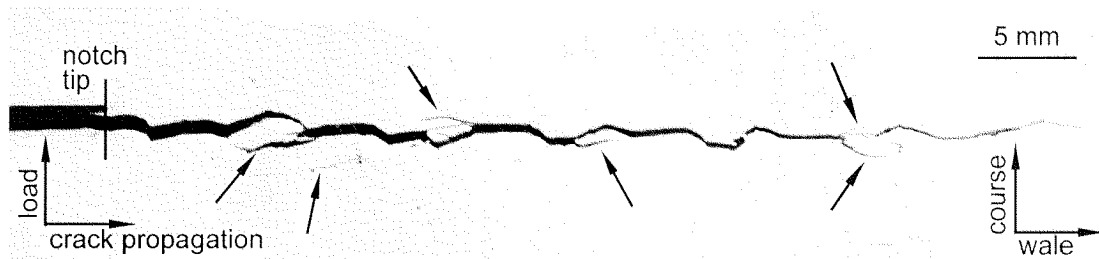


Figure 4.6: *Macroscopical crack in 90° compact tension testing (load in course, crack in wale) reflected the knit structure since it propagated predominantly along the fiber bundles. It was accompanied by crack splitting (arrows). By establishing a experimental relationship between crack length and sample compliance both effects are taken into account for the calculation of energy release rates G_{IC} .*

An analytical and experimental study of the compliance method is given in [117, 126]. In these papers a finite element method (FEM) analysis of the elastic behavior of CFRP double cantilever beam samples was performed to establish an analytical relation between crack length and compliance. Due to the shape and the complex anisotropic properties of the knitted CF reinforced PEEK compact tension samples, the present study is restricted to an experimental approach.

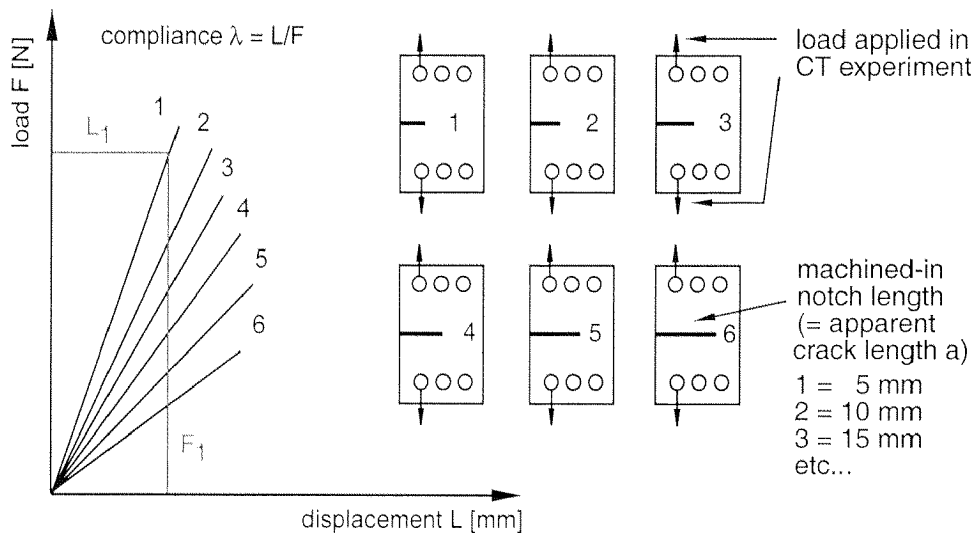


Figure 4.7: *Principle of the compliance method as applied in this work. In order to establish an experimental relation between apparent crack length and compliance, the latter was measured using samples with different notch lengths brought in by means of a diamond saw.*

The experimental relation between crack length and compliance was established by measuring the elastic response of compact tension samples with machined-in notches of different lengths (fig. 4.7). To measure the compliance, notches of different lengths (steps of 5 mm, covering the range 0 to 55 mm) were brought into a CF/PEEK compact tension sample with a diamond saw and the elastic compliance of the sample was recorded and plotted versus the notch length (fig. 4.8).

In order to derive the crack length at every crack propagation step from the load-displacement curve of a compact tension experiment, notch length vs. compliance was fitted using the function:

$$a = \frac{u_1 \cdot \lambda}{u_2 + \lambda} + u_3 \quad (1)$$

where a = crack length (= notch length) [mm]
 λ = compliance [mm/N]
 u_{1-3} = fitting parameters

Equation 1 was used as a mathematical function, fitting the crack length vs. compliance data with a correlation factor of $R^2 > 0.95$ (fig. 4.8).

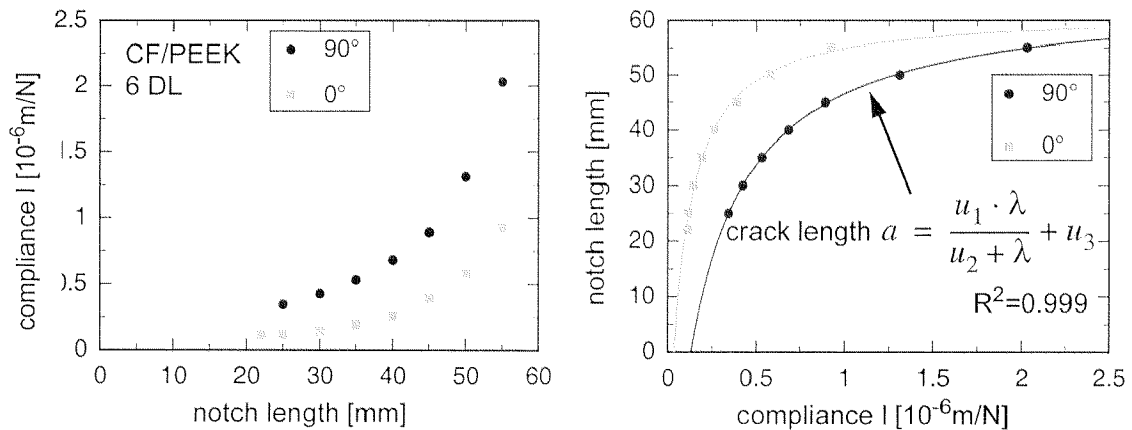


Figure 4.8: Notch length plotted vs. compliance. The measured data points were fitted in order to establish a relationship between crack length and compliance which allows to determine the crack length without actually measuring it.

A disadvantage of the experimental compliance method as applied in this work, is the fact that establishing of the crack length vs. compliance relation and the actual compact tension experiment cannot be performed on the same samples.

Energy release rates

Energy release rates were calculated according to linear fracture mechanics:

$$G_{IC} = \frac{\Delta E_{crack}}{\Delta a \cdot B} \quad (2)$$

where ΔG_{IC} = Energy release rate [J/mm^2]
 ΔE_{crack} = Energy [J], released in a crack propagation step of Δa
 Δa = crack growth [mm]
 B = sample thickness [mm]

The crack growth $\Delta a = a_2 - a_1$ (difference in crack length before and after a crack propagation step) was determined directly from the load-displacement curve of the compact tension test using the experimental relation between crack length and compliance (see figure 4.9).

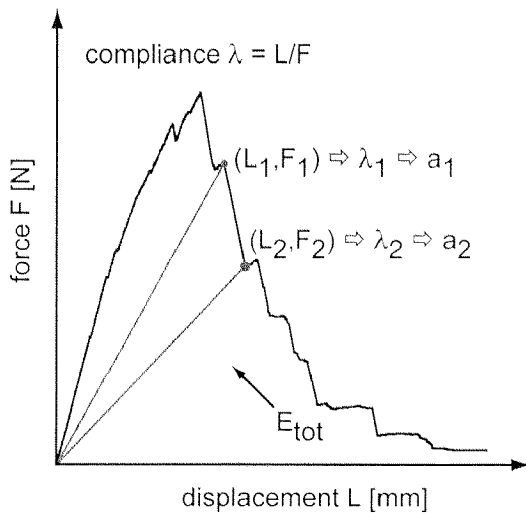


Figure 4.9:
 Calculation of the energy released in a crack growth step (ΔE) and of the related crack growth (Δa) determined directly from the load-displacement plot recorded in a compact tension experiment. The equations are based on linear fracture mechanics, assuming that plastic deformation can be neglected.

The energy released in a crack propagation step (ΔE) was also deduced directly from the load-displacement curve (fig. 4.9). The total energy change ΔE_{tot} of a crack propagation step can be expressed as follows:

$$\Delta E_{tot} = \Delta E_{elastic} + \Delta E_{crack} \quad (3)$$

where $\Delta E_{elastic}$ is the elastic energy stored in the compact tension sample. ΔE_{tot} can be written as:

$$\Delta E_{tot} = \int_{L_1}^{L_2} F dL = \frac{1}{2}(F_1 + F_2)(L_2 - L_1) \quad (4)$$

The elastic energy stored in the tensile testing apparatus and the mixed mode device is already taken into account by subtracting the system compliance from the experimental data (see figure 4.5). $\Delta E_{elastic}$ is equal to the difference in potential energy of the two points (L_1, F_1) and (L_2, F_2) on the load displacement curve:

$$\Delta E_{elastic} = \frac{1}{2}L_2F_2 - \frac{1}{2}L_1F_1 \quad (5)$$

ΔE_{crack} is the energy released by the crack, i.e. the value to be determined:

$$\Delta E_{crack} = \Delta E_{tot} - \Delta E_{elastic} = \frac{1}{2}(L_2F_1 - L_1F_2) \quad (6)$$

With ΔE_{crack} and Δa , calculation of energy release rates G_{IC} is completed applying equation 2.

Energy release rates were calculated for cracks covering a range from $a_0 = 22$ mm (brought-in notch length) up to $a = 50$ mm (90° testing) and $a = 35$ mm (0° testing), respectively. Beyond this range, the compliance method could not be applied because of extensive out-of-plane deformation.

Fracture toughness K_{IC}

With the determined energy release rates G_{IC} , fracture toughness K_{IC} was assessed using:

$$K_{IC} = \sqrt{G_{IC} \cdot E^*} \quad (7)$$

where K_{IC} = fracture toughness [$\text{MPa}\cdot\text{m}^{1/2}$]
 G_{IC} = energy release rate [J/m^2]
 E^* = effective modulus [GPa], calculated after [127]:

$$\frac{1}{E^*} = \frac{1}{\sqrt{2E_1E_2}} \sqrt{\frac{E_1}{E_2} - \nu_{12} + \frac{E_1}{2G_{12}}} \quad (8)$$

where E^* = effective Modulus [GPa]
 E_1 = Young's modulus (direction of crack growth) [GPa]
 E_2 = Young's modulus (load direction) [GPa]
 G_{12} = shear Modulus [GPa]
 ν_{12} = Poisson ratio []

Depending on the test direction (90° or 0° , see figure 4.1) different moduli were applied for E_1 and E_2 . In 90° testing, Young's modulus of knitted CF reinforced PEEK in wale

was used for E_1 and modulus in course for E_2 . Consequently, E_1 was set as modulus in course, E_2 as modulus in wale for 0° testing.

Determination of poisson ratio ν and shear modulus G_{12} is described in [46]. Table 4.1 summarizes the input values and results of equation 8.

	E_1 [GPa]	E_2 [GPa]	G_{12} [GPa]	ν []	E^* [GPa]
90°	49	15	7.2	0.57	18
0°	15	49	7.2	0.57	38

Table 4.1: *Input values for the calculation of the effective modulus E^* after [127]. The effective modulus used to assess fracture toughness K_{IC} depends on the loading angle applied in compact tension experiments.*

4.3. Results and discussion

4.3.1. Thermography

The thermographs presented in this section were recorded from compact tension experiments with a slightly different load situation than the setup applied for energy release rates determination, described in chapter 4.2.2. Load points were placed in the middle of the sample and not over the notch, therefore causing larger crack propagation steps accompanied by more pronounced load drops. The observed phenomena were identical in both experimental setups. However, with the load points in the middle of the sample, the degree of damage was larger due to the more unstable crack propagation.

Load in course, crack in wale direction (90°)

Sequences. The following thermographs (fig. 4.10) were recorded in passive mode shortly before and at the first major crack growth.

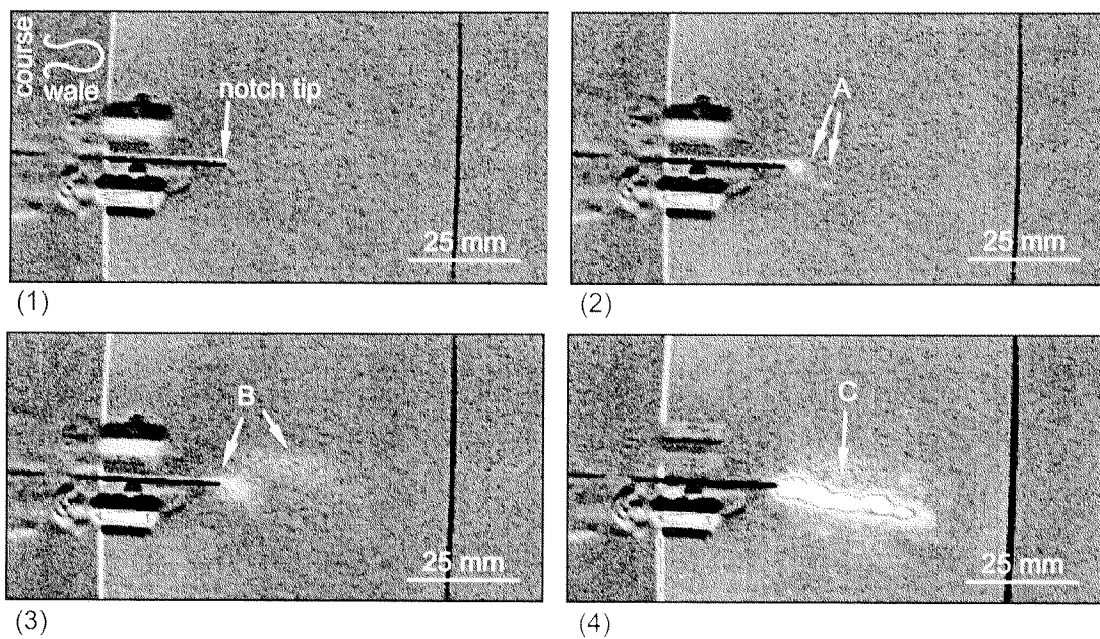


Figure 4.10: Sequence of thermographs recorded in passive mode shortly before (1) and at the first major failure event. The artifacts left of the notch tip were caused by extensometers. In (2) first failure events (A) are visible very close to the notch tip. In (3) other minor damage were observed further away from the notch tip (B), shortly before the first major crack growth (C) occurred in (4).

Minor damage events, observed shortly before the first major crack propagation, are assumed to be caused by fiber failure located in a distance of 0 to 10 mm from the notch tip. In the force displacement plots, these events could be correlated with small load drops before maximum load was reached (fig. 4.11). Intensive heat emission as shown in

figure 4.10 (4) was always caused by major, macroscopic crack growth. Thermographs as shown in figure 4.10 (3) were not accompanied by visible crack propagations, but rather correlated with crack splitting (fig. 4.6).

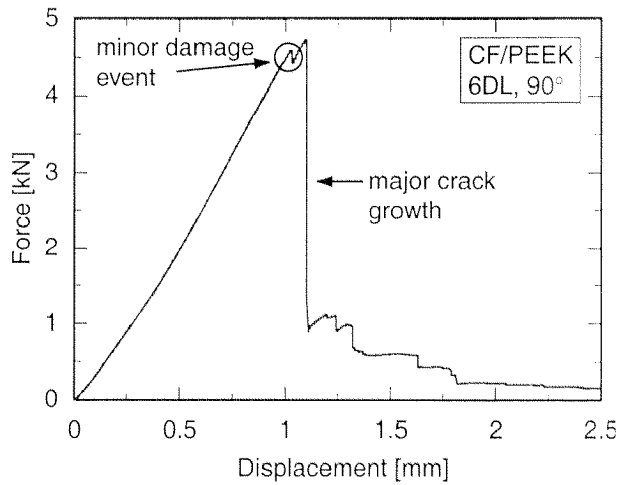
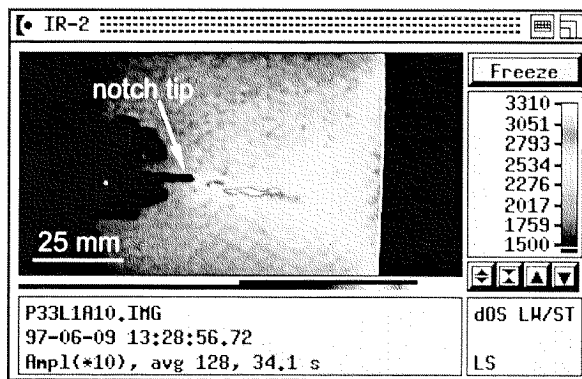


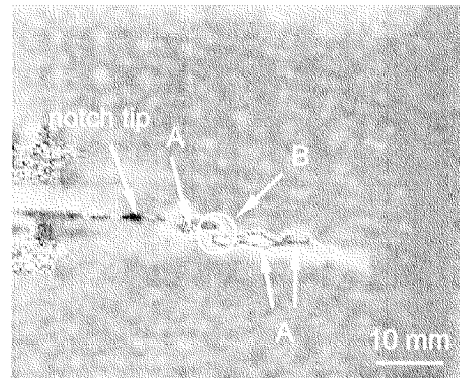
Figure 4.11:

Load-displacement curve of a compact tension experiment applying load in course (90°). Minor and major load drops were correlated with thermographs (fig. 4.10). Minor load drop occurring before load drop from F_{max} are assumed to be caused by fiber failure located in the vicinity of the notch tip. Load drop from F_{max} was correlated with major crack growth and intensive heat emission.

Active thermography. The damage zone was investigated using active thermography. Magnitude- and phase thermographs were taken to investigate shape and orientation of the damage zone (fig. 4.12).



Magnitude image



Phase image

Figure 4.12: Magnitude- and phase image of a tested knitted CF fabric reinforced PEEK compact tension specimen loaded in course. Temperature gradients caused by non-perpendicular irradiation of the sample are leveled out in the phase image. The crack plane was found to be parallel to fiber bundles oriented in wale direction, i.e. side limbs (A). Bridging to a different row of side limbs (B) was observed in some 90° compact tension specimens. The fracture path was found to follow the fiber bundle matrix interface.

Load in wale, crack in course (0°)

Sequences. Compact tension experiments with samples loaded in wale (0°) lead to higher maximum loads, because of the higher density of bundles oriented in load direction. Figure 4.13 shows a sequence of thermographic pictures, taken before and at the first major crack growth. In 0° testing, spots as shown in figure 4.13 (B), arising from surface displacement, were observed in the thermographs. As described in chapter 4.3.1, the first thermograph in the sequence was subtracted from the others in order to extract failure events. Because of this subtraction, surface locations with changing thermal emission become apparent in the thermographs. The spots in (B), fig. 4.13, did neither disappear nor move and became more intensive throughout the experiment. This indicates that they were caused by deformation rather than damage. In 0° testing concentrated deformation including an out-of-plane component is expected in the intermeshing areas, whereas in 90° testing deformation is homogeneously distributed between fibers and matrix. Out-of-plane deformation at the sample surface affects the thermal emission at the locations of deformation. Therefore, the spots in (B) are assumed to be caused by out-of-plane deformation of the intermeshing areas. Deformation of intermeshings occurred to a much lesser extend in 90° testing (fig. 4.10), which explains the fact that the spots were observed in 0° testing only.

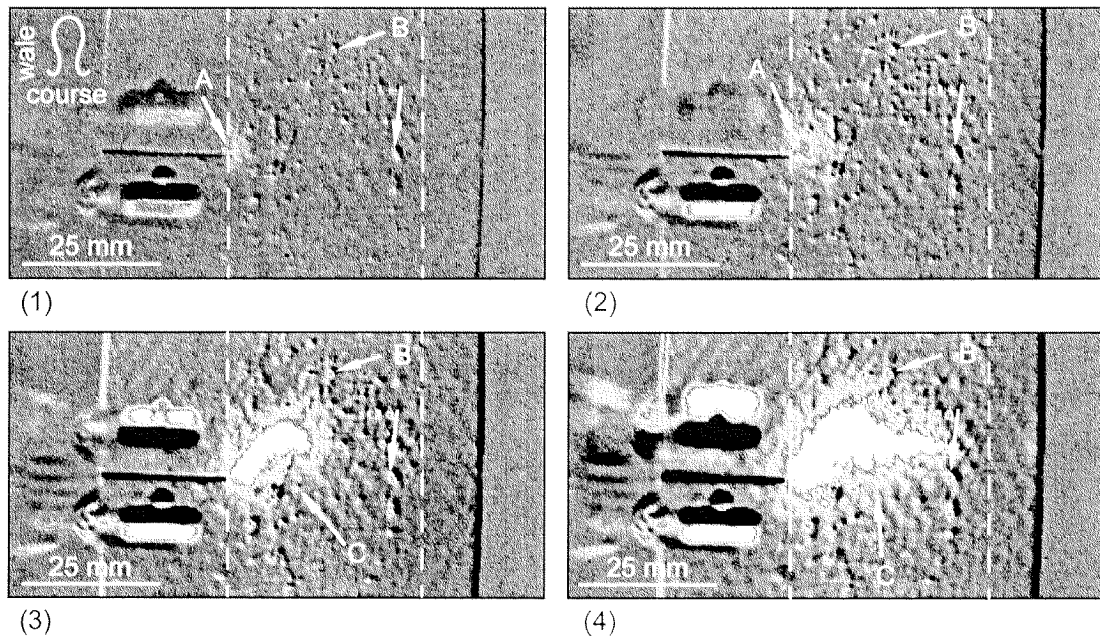


Figure 4.13: *Passive thermographic sequence of a compact tension experiment applying load in wale (0°). Minor damage events (A) and major crack growth (C) were correlated with the respective load displacement curve. Compared to 90° testing (see figure 4.10) the failure process generates more thermal radiation which is distributed in a larger damage area. The spots in area (B) are assumed to be caused by deformation of intermeshing areas located at the sample surface.*

Active thermography. Magnitude- and phase thermographs taken after 0° testing are shown in figure 4.14. The fracture path was found to follow loop heads (A). Bridging (B) occurred from one row of loop heads to the next.

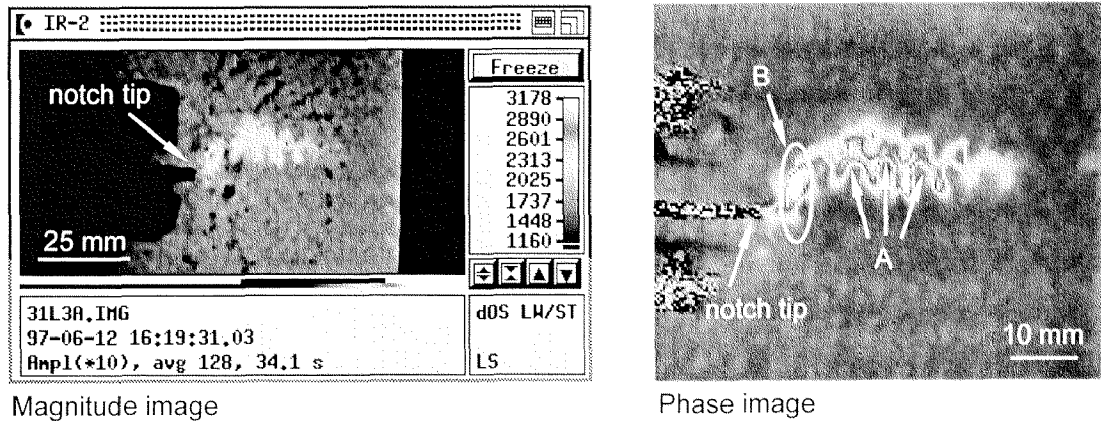


Figure 4.14: Active thermography of tested 0° compact tension sample. The fracture path was observed to follow the loop heads along the bundle/matrix interface (A). In some cases bridging to another row of loop heads occurred (B). The damage zone is significantly larger than in the case of 90° compact tension testing (see figure 4.12).

A more detailed description of failure mechanisms in mode I is given in chapter 4.4, combining the findings from thermography with numerical results and SEM investigations.

4.3.2. Energy release rates G_{IC}

Load in course, crack in wale (90°)

Figure 4.15 (top) shows a representative, system compliance corrected load-displacement curve of a 90° compact tension experiment. A criterion for significant crack growth was defined in order to calculate energy release rates G_{IC} (equation 7). Load drops of more than 80 N were found to be a reasonable value for significant crack growth. Minor damage occurred throughout the entire experiment after load surpassed 1000 N. However, these minor events were neither accompanied by significant load drops nor by macroscopical crack growth. Calculation of G_{IC} was limited to significant crack growths.

In figure 4.15 (bottom), energy release rates G_{IC} are plotted versus the crack length. Crack lengths at every significant crack growth were determined using the compliance method.

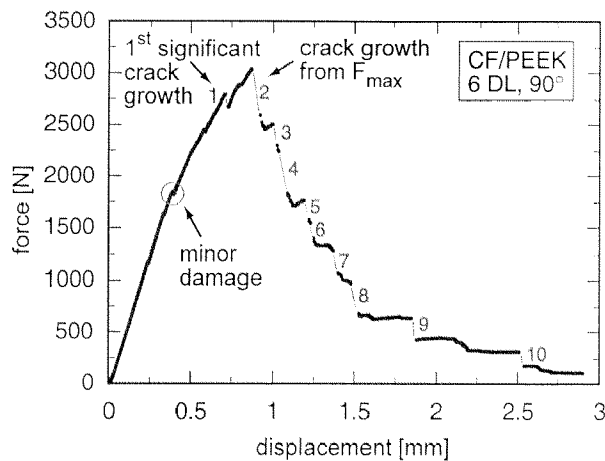
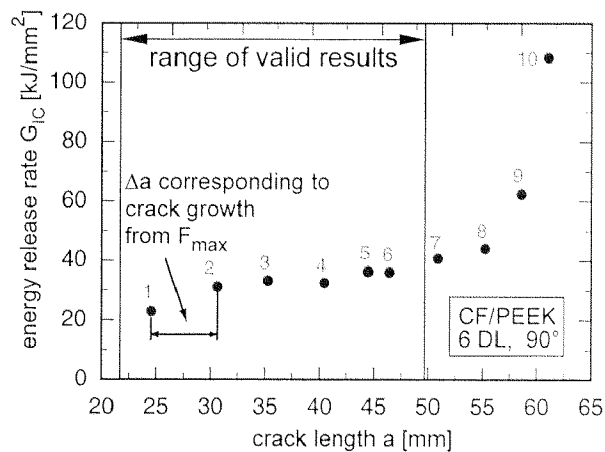


Figure 4.15:

Typical load-displacement curve of a 90° compact tension experiment. The load drops indicate crack growth. Depending on the location of the notch tip, small crack propagations were observed before the maximum force was reached. The criterion for significant crack growth, i.e. calculation of G_{IC} , was defined at load drops > 80 N.



Energy release rates were calculated (equation 7) from every significant crack growth and plotted versus crack length (corresponding to length reached after the respective crack growth). Values below a crack length of 50 mm are taken into account. Beyond this limit, results are invalid due to extensive out-of-plane deformation of the sample.

Significant load drops were found to be equivalent to a crack propagation step Δa of maximum 8 mm. When crack length surpassed 50 mm, values for G_{IC} increased heavily. This is a consequence of extensive out-of-plane deformation of the sample. When exceeding 50 mm, the crack tip was getting too close to the opposite border of the compact tension sample and linear fracture mechanics assumptions are no longer fulfilled.

Selection of specific energy release rates. In order to compare G_{IC} of different samples, specific values on the G_{IC} vs. crack length curves were chosen. Two crack propagation steps could be distinguished unambiguously on every load-displacement curve of a compact tension test. One is the load drop from F_{max} , the other is the first significant crack growth ($\Delta N > 80$ N) on the load-displacement plot. In most cases, the first significant load drop was found to be followed by load drops from F_{max} as shown in figure 4.15. In some cases, however, these two values corresponded to one single load drop or a third significant crack growth occurred in between (fig. 4.16).

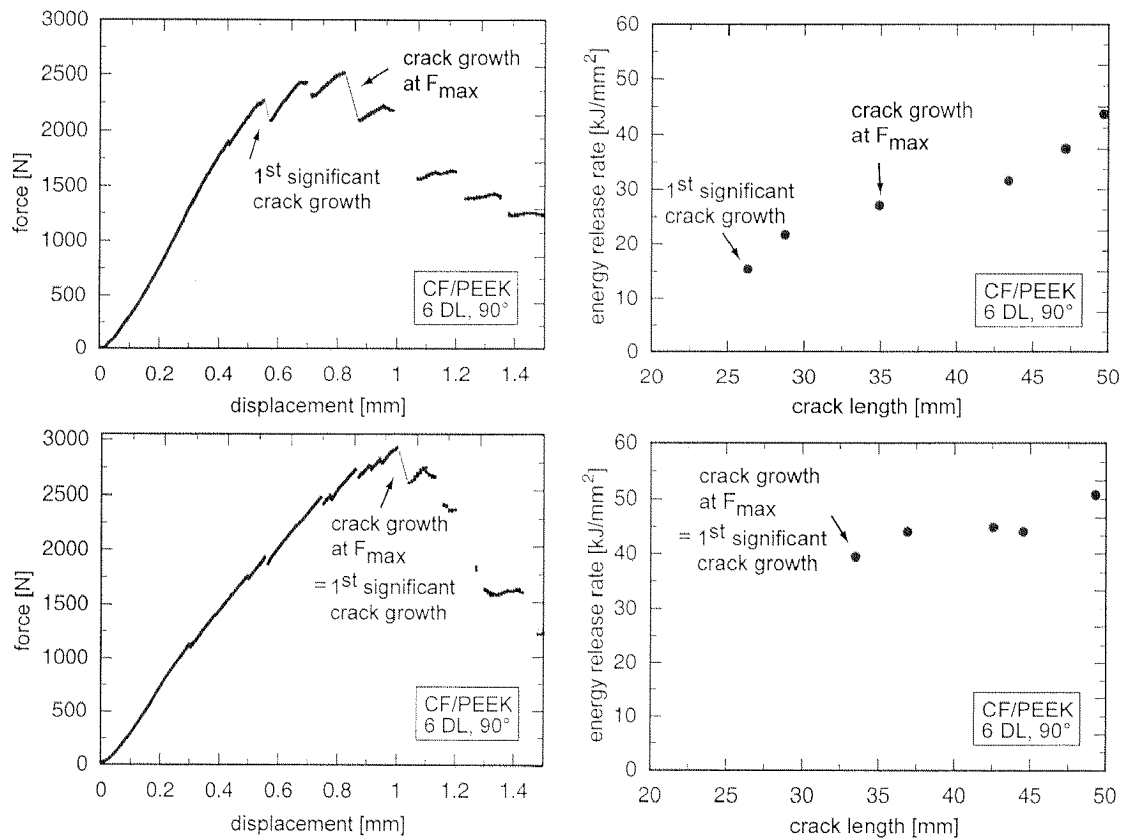


Figure 4.16: Load-displacement and G_{IC} vs. crack length plots of compact tension experiments in 90° direction. Top: The first significant load drop ($\Delta N > 80N$) is not directly followed by crack growth occurring at F_{max} . In the resulting energy release rates vs. crack length curve, the respective G_{IC} values differ significantly. Bottom: The first significant load drop occurred at F_{max} i.e. only one specific energy release rate was determined from this curve.

A significant difference was found between the energy release rates referring to the first significant load drop and those determined at F_{max} . Results from 6 independent compact tension experiments are summarized in table 4.2.

	G_{IC} (1 st significant) [kJ/mm ²]	G_{IC} (F_{max}) [kJ/mm ²]
average	22.5	31.7
standard deviation, % in ()	9.1 (40%)	6.9 (22%)

Table 4.2: Energy release rates at the first significant crack growth ($\Delta N > 80N$) and at crack growth from F_{max} . A lower average of G_{IC} at 1st significant crack growth was found while its standard deviation was higher.

A possible explanation of the differences in G_{IC} at the first significant load drop and at F_{max} is found when considering the notch tip position in different compact tension samples. The SEM analysis of the fracture surfaces (chapter 4.3.4) indicated that crack growth is mainly controlled by the distribution of bundles oriented in load direction. The crack is assumed to be stopped in locations with a high density of these pinning bundles. The notch tip position in compact tension samples is randomly distributed relative to these locations. Depending on the notch tip position, the first significant crack could also occur in areas with a few pinning bundles, whereas crack growth from F_{max} would only start from locations with a high density of pinning bundles. The distribution of pinning bundles is defined by the 3D reinforcement structure (see chapter 3) and is independent of the notch tip position. Therefore, G_{IC} from F_{max} is assumed to be a material parameter whereas G_{IC} of the first significant crack growth depends on the notch tip position relative to the reinforcement structure. Two observations confirm this assumption. First, the value found for G_{IC} at the first significant crack growth is lower and second it revealed a higher standard deviation (table 4.2). This is not surprising, when assuming its dependence of the randomly distributed notch tip position.

Load in wale, crack in course (0°)

The analysis of 0° testing was done similarly to the 90° case presented above. Similar behavior was observed at substantially higher loads, leading to superior energy release rates. Figure 4.17 shows results determined from a 0° representative compact tension experiment.

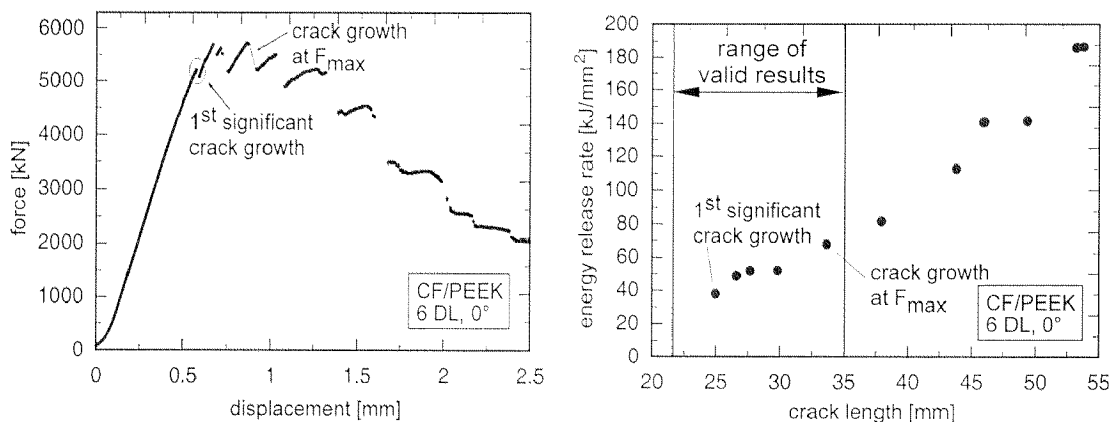


Figure 4.17: Force vs. displacement curve of a compact tension experiment applying load in wale (0°). The respective G_{IC} vs. crack length plot reveals rapid increase of the G_{IC} values in function of the crack length. This is due to extensive out-of-plane deformation of the compact tension sample which limited the validity of the 0° testing to a maximum crack length of approximately 35 mm.

Out-of-plane deformation (fig. 4.18 b) was observed to be higher than in 90° testing because of the higher load levels. This limited the validity of the determined energy

release rates to a maximum crack length of approximately 35 mm (fig. 4.17, right). Fracture paths that were neither straight nor perpendicular to load were often observed in 0° testing.

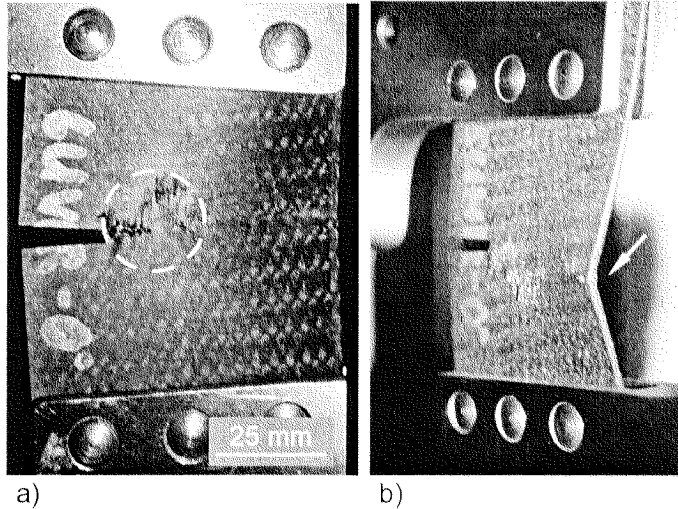


Figure 4.18:
Compact tension samples loaded in wale direction (0° testing). Non-planar, large, ($\varnothing > 15$ mm) fracture zones with bridging (a) occurred more frequently than linear fracture paths. Extensive out-of-plane deformation (b) limited the validity range more than in 90° compact tension testing.

Table 4.3 summarizes the results found for G_{IC} in 0° testing. Similar to 90° testing, energy release rates at the first significant load drop are substantially lower than those at F_{max} .

	G_{IC} (1 st significant) [kJ/mm ²]	G_{IC} (F_{max}) [kJ/mm ²]
average	53.5	73.7
standard deviation, % in ()	12.3 (23 %)	14.9 (20%)

Table 4.3: Energy release rates at the first significant crack growth ($\Delta N > 80N$) and at crack growth from F_{max} . It is assumed that the difference is caused by the diverse mechanism of the two criteria.

Again, energy release rates at the first significant load drop are substantially lower than those at F_{max} . Similar to the 90° situation, this can be explained by the fact that the notch tip is randomly distributed relative to the textile structure. The first significant crack growth is dependent on the notch tip whereas crack growth from F_{max} is assumed to be a material parameter.

4.3.3. Fracture toughness K_{IC}

Fracture toughness K_{IC} was calculated using energy release rates G_{IC} and equation 8 (see chapter 4.3.2). The results are presented in table 4.4.

K_{IC} [MPa·m ^{1/2}]	90° (1 st)	90° (F _{max})	0° (1 st)	0° (F _{max})
average	19.7	23.6	44.7	52.5
stdev, % in ()	3.8 (19%)	2.7 (11%)	5.2 (12%)	5.3 (10%)

Table 4.4: Fracture toughness K_{IC} of knitted CF fabric reinforced PEEK. 1st stands for the first significant load drop, F_{max} for peak load in the load displacement curve of the compact tension experiments.

K_{IC} of F_{max} will be used to compare the fracture toughness of different materials, because it is a material parameter, whereas K_{IC} of the first significant crack growth is influenced by the notch tip position relative to the reinforcement structure (see chapter 4.3.2). K_{IC} of F_{max} corresponds to the ultimate fracture toughness, i.e. the critical failure criterion in an application.

A comparison of K_{IC} values is given in table 4.5. Knitted CF reinforced PEEK is in the same range as 3D woven CF/Epoxy and aluminum cast alloys. The fracture toughness of APC(ITA)/IM8 (UD) reinforced composites is defined by the fiber/matrix interface (when load is applied perpendicular to the fibers). Therefore, it is much lower as in the knitted CF reinforced PEEK samples presented here.

material	K_{IC} [MPa·m ^{1/2}]	source
APC(ITA)/IM8 (UD)	3.5	[127]
PEEK	7	[128]
CF/Epoxy (3D woven)	20 - 30	[129]
Knitted CF reinforced PEEK (90°)	24 ± 3	present work
Knitted CF reinforced PEEK (0°)	53 ± 5	present work
Aluminum cast alloy (AISI7Mg0.3)	23	[130]
Ti6Al4V (equiaxed)	44 - 66	[131]

Table 4.5: Fracture toughness K_{IC} of different composite, polymer and metallic materials. The knitted CF reinforced PEEK studied in this work reveals high fracture toughness, specifically in comparison with other composite materials.

4.3.4. SEM analysis

After compact tension testing, samples were separated, platinum sputtered (10 mA for 600 s) and investigated in a scanning electron microscope (SEM).

Load in course, crack in wale (90°)

The damage zone caused by crack growth parallel to wale direction was found to be relatively straight and linearly shaped. An overview of a fracture plane is shown in figure 4.19, details are shown in figure 4.20. The following observations were made in these SEM micrographs:

- The crack followed the surface of side limbs (B). Fiber bundles perpendicular to load (belonging to loop heads or feet) showed tensile failure (A).
- Fiber bundles represented the smallest unit in the damage zone. Fibers isolated from bundles were not observed.
- Small fiber pull-out lengths were observed on the fracture surface of bundles failed in tension. This indicates good fiber/matrix adhesion.
- The crack front is supposed to be “pinned” at locations with a high density of bundles perpendicular to load. Between these pinning bundle groups, the crack propagated along the side limbs (B).
- The fracture surface does not reflect the knit layer structure. The studied sample consisted of 12 individual knit layers which cannot be distinguished from each other at the fracture surface.
- All detected damages were found within one row of loops. Therefore, the width of the damage zone on each side of the fracture plane is supposed to be in the order of the loop width, i.e. approximately 5 mm.

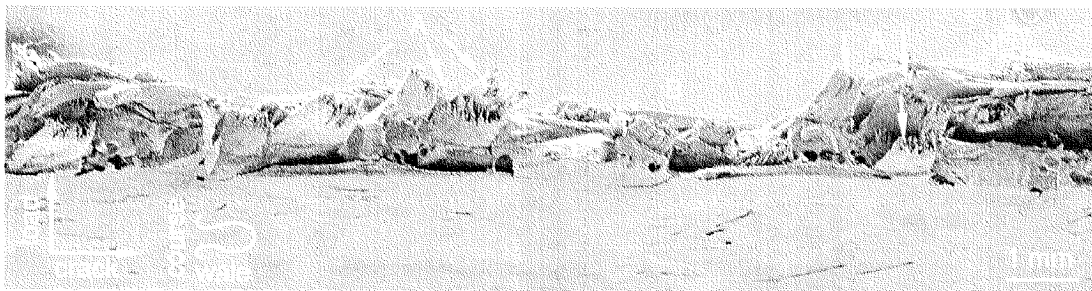
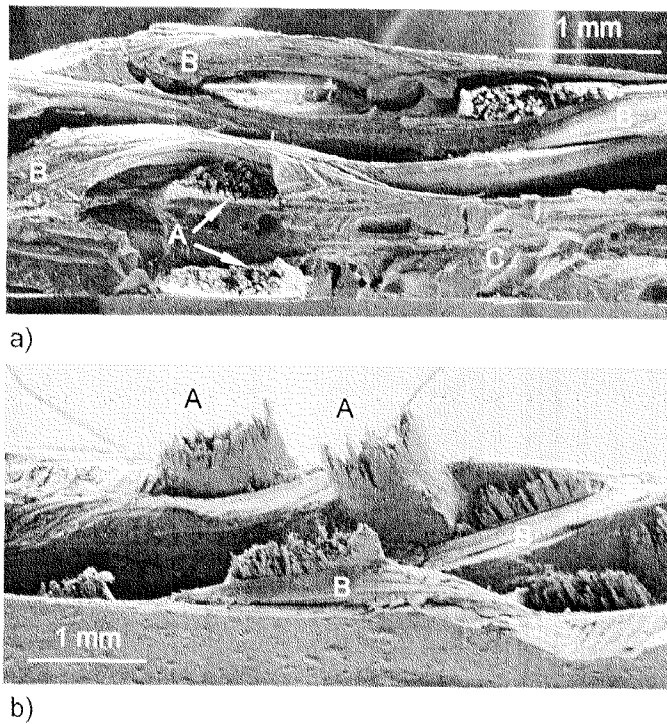


Figure 4.19: SEM micrograph of a fracture plane in wale after total failure (load in course). In areas (A) several bundles are oriented in load, while in (B) bundle surfaces of side limbs are predominant. At locations with a high bundle density perpendicular to load (A) the crack front is assumed to be “pinned”. Between these pinning bundle groups, fracture is unstable and follows the side limbs.

Figure 4.20 represents more detailed views of the damage zone resulting from compact tension test in 90°.



*Figure 4.20:
Fracture plane resulting
from a 90° compact tension
experiment. The 12 knit
layers of this sample cannot
be distinguished from each
other (a). The fracture
surface consists of loop
heads or loop feet failed in
tension, i.e. pinning bundles
(A), surfaces of side limbs,
i.e. guiding bundles (B) and
few locations with matrix
concentration (C).*

The micrographs presented in figure 4.21 a-c show an area around a fiber bundle (loop head or feet) oriented in direction of the applied load. A section with considerable matrix deformation is shown in a). Plastic deformation of the matrix indicates slow, stable crack growth. Brittle matrix failure is apparent in c) which is a sign of fast, unstable crack propagation. The transition from slow to fast crack growth is shown in b). This observation is coherent with the following mechanism:

Crack propagation was slow up to the fiber bundle oriented in load. At the bundle the crack front was stopped until critical tensile load was reached, leading to tensile failure of the fiber bundle. The instantly released energy of that failure process caused fast, unstable crack growth.

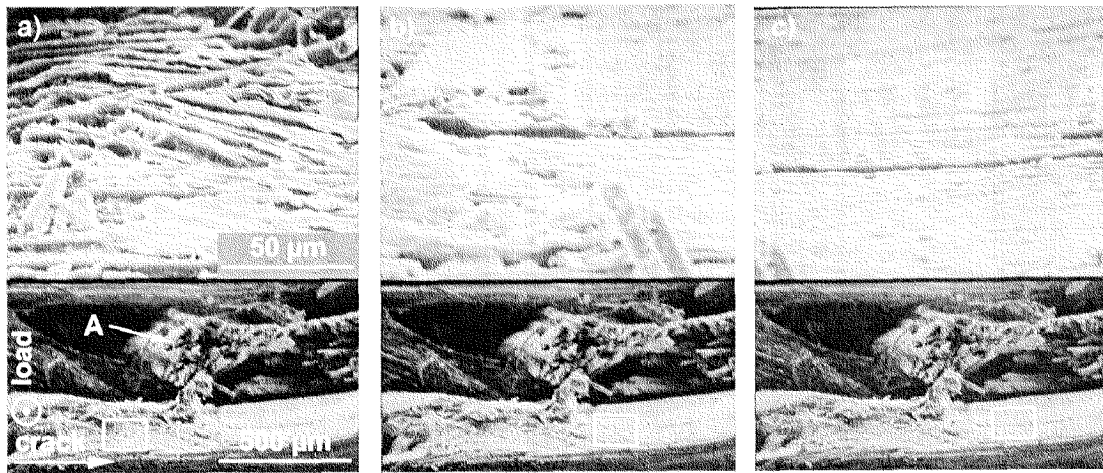


Figure 4.21: Matrix deformation on a bundle/matrix interface area around a fiber bundle (A) oriented perpendicular to crack growth indicated, that crack propagation speed up to the bundle (a) was lower than after failure of the bundle (c). The transition phase is shown in (b).

Load in wale, crack in course 0°

In 0° testing, loop side limbs are oriented in load whereas loop heads and feet are perpendicular to it. In general, the systematics of the 0° fracture planes was similar to that of 90° testing. Bundles were found to be the smallest isolated units in a fracture surface. The fracture planes consisted of bundles oriented in load which failed in tension and bundle surfaces oriented in crack propagation direction. However, in 0° testing bundles failing in tension are side limbs and bundle surfaces oriented in crack propagation direction belong to loop heads and feet, i.e. vice versa to 90° testing. Because of the higher side limb density, more bundles are available to pin the crack (fig. 4.23). This is assumed to be the reason for the higher fracture toughness K_{IC} found in 0° testing (table 4.5).

The damage zones resulting from crack propagation in course were larger than those of propagation in wale. Similar to 90° testing, the detected damage zone remained within one row of loops. Since the width of a row of loops in 0° testing is the distance from feet to head (\neq loop height, see chapter 2), the width of the damage zone was found to be in the order of approximately 10 mm on each side of the macroscopic fracture path.

Bridging over several rows of loops was observed more frequently than in 90° testing. This can be understood considering that a fracture path in wale (parallel to side limbs) is energetically favorable to a fracture path in course where the density of pinning bundles is higher.



Figure 4.22: Overview of a fracture path resulting from compact tension applying load in wale. Because of bridging (E), the fracture path involves several loop rows (D). Side limbs (A) pinned the crack and failed in tension. Loop heads (B), oriented parallel to the fracture path, guided the crack.

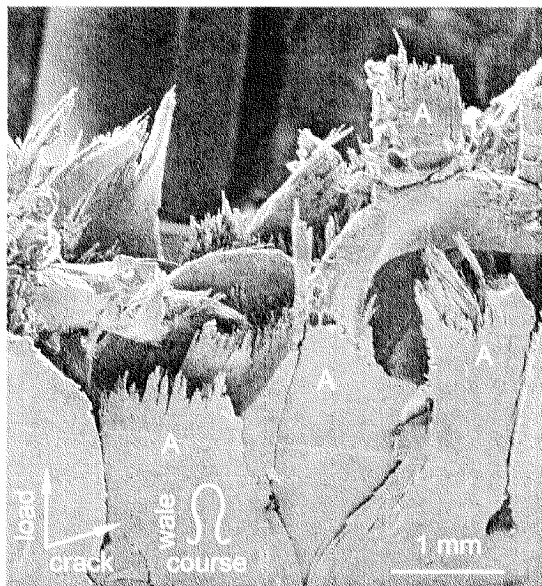


Figure 4.23: The SEM micrograph shows fiber bundles oriented in load, i.e. side limbs of the loop (A). The density of bundles perpendicular to crack propagation is higher in 0° than in 90° testing. This is assumed to be the reason of the higher fracture toughness determined in 0° testing (table 4.5). The width of the damage zone was found to be in the order of 10 mm (distance from loop feet to head).

4.4. Conclusions

The investigation of the failure behavior of knitted CF reinforced PEEK by means of compact tension testing, thermography and SEM analysis of the fracture zones lead to the conclusions presented below. They are summarized with respect to crack growth, fracture path and damage zone. A phenomenological model, describing the failure process of mono- and multilayer KFRCs is proposed.

Crack growth. On a macroscopic scale, stable crack growth was observed. Crack propagation steps of 4 to 8 mm in wale direction (90° testing) and 2 to 6 mm in course direction (0° testing) occurred, respectively. Crack growth was unstable between the propagation steps which could be shown by the devolution of the load-displacement curves (load drops) and by the microscopical structure of the fracture surface. Fiber bundles perpendicular to crack propagation defined the limits of the unstable propagation steps. These bundles stopped and pinned the crack front until a critical load at the crack tip was reached which re-initiated crack propagation by tensile failure of the pinning bundles (see figure 4.24). Minor damage events, observed by thermography shortly before the first major crack propagation, are assumed to be caused by fiber failure located in a distance of 0 to 10 mm from the notch tip.

Fracture path and damage zone. The fracture path was defined by the reinforcement structure. The crack was observed to follow the bundle/matrix interface of bundles oriented in crack propagation direction. These guiding bundles consisted of side limbs in 90° testing and of loop heads/feet in 0° testing. The pinning bundles, oriented perpendicular to the fracture path, failed due to tensile load. In some cases, predominantly in 0° testing, bridging of the fracture path along the pinning bundles to the next row of loops was observed.

The width of the visually detectable damage zone was in the order of one row of loops on every side of the fracture path (fig. 4.24). In 90° testing, the width of a loop row equaled approximately the loop width (≈ 5 mm), whereas in 0° testing it corresponded to the distance between loop feet and loop head (≈ 10 mm). Within the damage zone, bundles were the smallest isolated units observed. The bundles remained compact and revealed short fiber pull-out lengths. This indicates good fiber/matrix adhesion.

Model of out-of-plane failure in mode I. The studied KFRC compact tension samples consisted of 12 knit layers. Throughout consolidation, the individual knit layers were displaced against and interpenetrated with each other (chapter 3). Therefore, the knit layers were not aligned one behind the other but distributed within the composite. The failure behavior can be better understood considering the interpenetrated multilayer structure of the studied KFRC.

A scheme of fracture on the level of a monolayer structure is presented in figure 4.24. As described above, the crack (A) is pinned by bundles oriented in the direction of the applied load. Because of the higher density of pinning bundles, higher fracture toughness is to be expected in 0° testing. The width of the visually detectable damage

zone equals approximately one row of loops on each side of the fracture path (B). Because of loop orientation the damage zone is larger in 0° testing than in 90° testing.

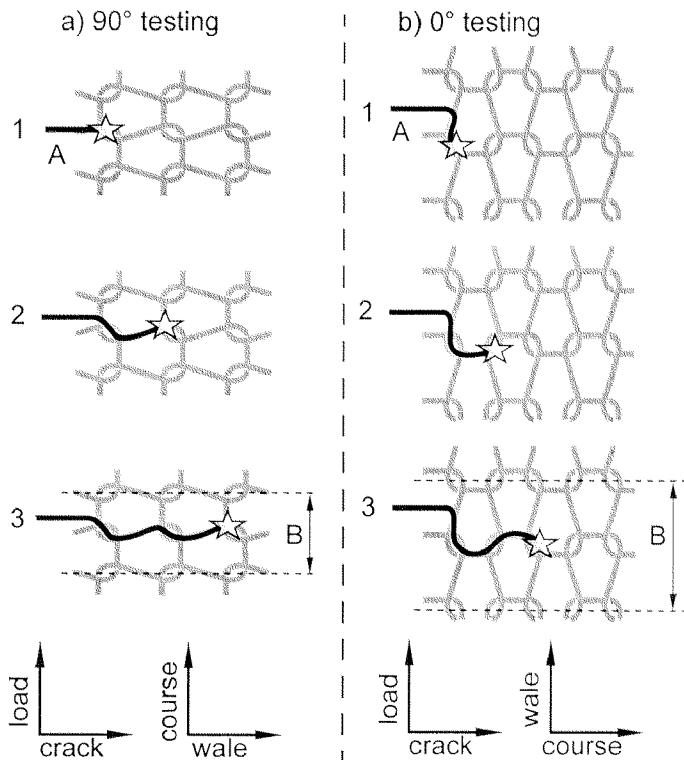


Figure 4.24: Phenomenological model of failure mechanisms in wale (a) and course (b) direction, illustrated on the level of a monolayer knit structure. The crack (A) follows bundles oriented in propagation direction (guiding bundles). At bundles oriented in load it is pinned and re-initiated when critical tensile load is reached in the pinning bundle. The width of the damage zone (B) is in the order of one row of loops on each side of the fracture.

A top view on the fracture surface of a multilayer KFRC is schematically drawn in figure 4.25 (a comparable SEM micrograph of the real structure is shown in figure 4.20). The fracture surface consists of pinning (A) and guiding (B) bundles. The individual knit layers cannot be distinguished because of interpenetration throughout consolidation.

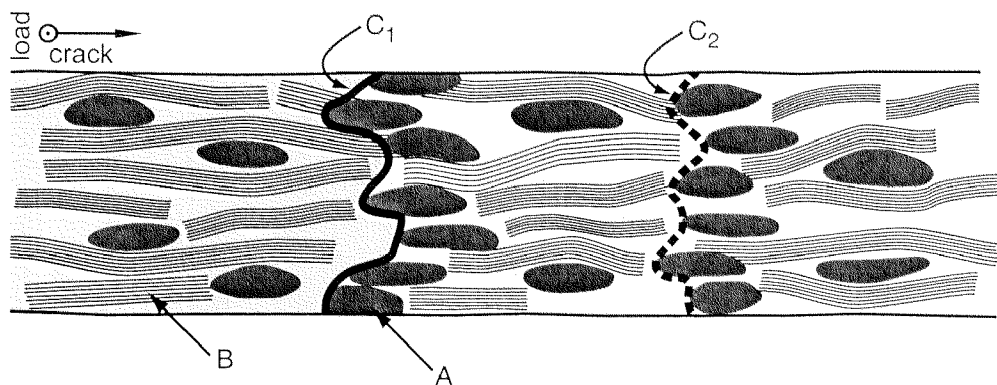


Figure 4.25: Fracture surface of an interpenetrated, multilayer KFRC failed in mode I (out-of-plane). Areas with a high density of pinning bundles (A) stop the crack front (C_1). When critical tensile load is reached unstable crack growth occurs along guiding bundles (B) to the next location with sufficient pinning bundle density (C_2).

The failure mechanisms of the individual knit layers described above are supposed to interact as follows: The crack propagates along guiding bundles and is stopped at locations with a high density of pinning bundles (fig. 4.25, C_1). When critical tensile load is reached in the crack front, tensile failure of the pinning bundles in C_1 occurs and the crack propagates unstably to the next location with sufficient fiber bundle density (fig. 4.25, C_2).

The proposed mechanism considers the density of guiding and pinning bundles. According to this mechanism, the total energy released in the fracture process can be subdivided in two parts, proportional to the density of pinning and guiding bundles:

$$G_{IC,total} = x \cdot G_{IC,pinning} + (1 - x) \cdot G_{IC,guiding} \quad (9)$$

where	x	=	portion of pinning bundles
	$1-x$	=	portion of guiding bundles
	$G_{IC, pinning}$	=	energy released in tensile failure bundles
	$G_{IC, guiding}$	=	energy released in bundle/matrix debonding

The energy released in bundle/matrix debonding is orders of magnitude lower than the energy released in tensile failure of fiber bundles. Therefore, the essential contribution to $G_{IC,total}$ is defined by $G_{IC,pinning}$.

A first confirmation of this model are the values found for $G_{IC,0^\circ}$ ($=74 \text{ kJ/mm}^2$) and $G_{IC,90^\circ}$ ($=32 \text{ kJ/mm}^2$). $G_{IC,0^\circ}/G_{IC,90^\circ}$ correspond to a ratio of 2.4/1. The ratio of pinning bundles in 0° testing to pinning bundles in 90° testing can be approximated with $2 \cdot (\text{loop height} / \text{loop width}) = 3/1$. Considering the contribution of bundle/matrix adhesion which is higher in 90° testing, the ratio 2.4/1 found in the experiment can be well understood with the proposed model.

General conclusions. In summary, the modified compact tests combined with an experimental compliance method was found to be a suitable method to determine G_{IC} and K_{IC} of KFRCs. Compared to other composite materials, knitted CF reinforced PEEK reveals a high fracture toughness. K_{IC} of $24 \text{ MPa}\cdot\text{m}^{1/2}$ was found in 90° , $53 \text{ MPa}\cdot\text{m}^{1/2}$ in 0° testing (table 4.5). The lower value is in the order of 3D woven CF/epoxy composite. High fracture toughness and macroscopically stable crack growth indicate that knitted CF reinforced PEEK is a structural composite with highly damage tolerant failure properties.

5. FAILURE BEHAVIOR II: INSTRUMENTED FALLING WEIGHT IMPACT

5.1. Introduction

Damage tolerance is described by Jones [132] as the ability of a structure to contain weakening defects under representative loading and environment without suffering excessive reduction in residual strength. Structures are designed to meet a specific set of criteria, but are frequently subjected to an unspecific range of miscellaneous events (e.g. accidental impacts, occasional overload, misuse and abuse) which fall outside of these design parameters and can lead to damage [133]. Metals react tolerantly to these events because of their inherent ability to yield. Typical composite materials do not exhibit this ability and fracture occurs if the elastic limits are exceeded. The control of damage tolerance in composites is therefore the control of the fracture process [133].

In the previous chapter static failure properties of knitted CF reinforced PEEK was studied by means of compact tension testing. A model describing out-of-plane failure in mode I was proposed. It was found that the investigated KFRCs exhibit high fracture toughness and macroscopically stable crack growth. The static failure properties were therefore observed to be highly damage tolerant in comparison with other composite materials. This chapter treats the dynamic failure properties, investigated by means of falling weight impact testing. The KFRCs studied in this work are considered for structural parts in applications in which impact events are to be expected [134]. Consequently, impact properties such as the absorbed energy upon penetration, peak failure loads and impact failure behavior of KFRC panels are of major importance. Impact testing causes pronounced interlaminar shear stresses. Therefore, another factor studied in this chapter was to determine if impact failure is accompanied by interlaminar fracture along knit layers. The different aspects addressed are summarized as follows:

- Impact performance of KFRCs compared to other composite materials.
- Damage development and failure behavior, specifically delamination of KFRCs in impact testing.
- Influence of panel thickness on impact properties of KFRCs.
- Influence of fiber and matrix material (CF/PEEK, GF/semicrystalline PET, GF/amorphous PET) on impact properties.
- Differences and common characteristics in static out-of-plane failure and dynamic impact failure behavior of knitted CF reinforced PEEK.

5.2. Methods

Instrumented falling weight impact testing is a commonly used method to study the impact performance of composite materials. A hemispherical tipped dart is released from a predetermined height to strike the specimen supported on a steel ring. A force transducer in the striker provides force-time data throughout the entire impact event. This basic force-time record is used to compute derived data, such as force-displacement, energy-time and velocity-time. The derived data is calculated on the basis of Newtonian mechanics, knowing the striker mass and its incident velocity when hitting the specimen. The basic physical equation is:

$$mg - F = m \frac{dv}{dt} \quad (10)$$

where: m = mass of the striker
 F = measured force
 g = specific gravitational force

Integration of equation 10 gives the information on velocity v , displacement x and energy E of the striker after initial contact with the specimen:

$$v = v_0 + gt - \frac{1}{m} \int_0^t F dt \quad (11)$$

where: v_0 = initial striker speed

$$x = vt + \frac{1}{2}gt^2 - \frac{1}{m} \int_0^t \int_0^t F dt \quad (12)$$

$$E = v_0 \int_0^t F dt + g \int_0^t Ft dt - \frac{1}{2m} \left(\int_0^t F dt \right)^2 \quad (13)$$

Perforation and low energy impact. Two impact modes were investigated in this work. In perforation impact testing, sufficient initial energy for the complete penetration of the specimen was applied, while the speed of the dart was intended to be reduced to a minimum. Another type of impact damage was caused by low energy impact testing, which required a significant reduction of the initial striker energy. This method does not involve specimen penetration and was performed to study failure initiation.

Characteristic parameters. In order to determine impact properties and to compare impact behavior of different materials, characteristic impact parameters were defined (see figure 5.1). The total dissipated energy (E_{tot}) is the sum of initiation (E_{init}) and propagation energy (E_{prop}). Initiation energy is determined at peak force (F_{peak}) whereas propagation energy is the energy absorbed in the specimen from peak force to completed perforation. In low energy impact testing only the total dissipated energy and peak force are considered.

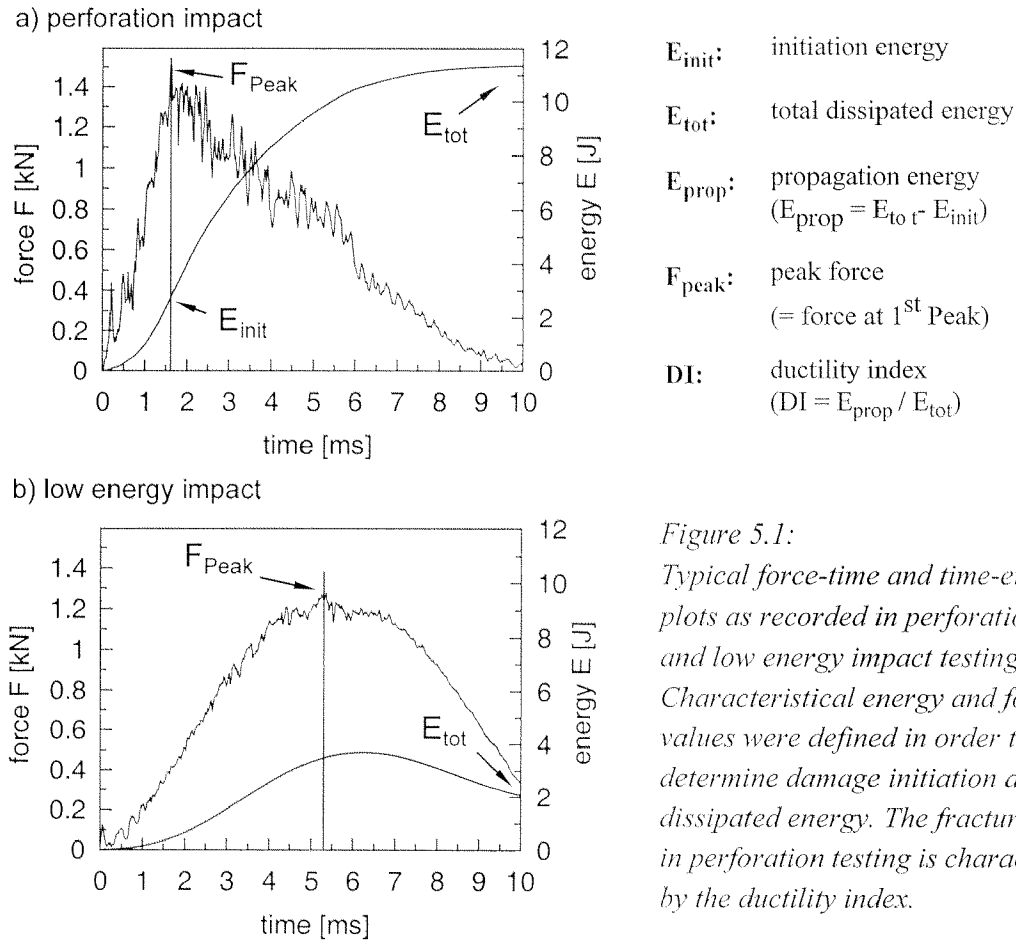


Figure 5.1:
Typical force-time and time-energy plots as recorded in perforation (a) and low energy impact testing (b). Characteristic energy and force values were defined in order to determine damage initiation and dissipated energy. The fracture mode in perforation testing is characterized by the ductility index.

Specimens and experimental setup. Knitted CF reinforced PEEK and knitted GF reinforced PET was manufactured as described in chapter 2. CF/PEEK panels were obtained, consisting of 4 and 6 DL with thicknesses of 1.31 and 1.81 mm, respectively. Amorphous GF/PET revealed a thickness of 1.35 (3 DL), semicrystalline GF/PET of 1.8 mm (4 DL).

Instrumented falling weight impact tests were performed using a “Fractovis” impact equipment with an AFS-MK4 modul of Ceast (Italy). The data acquisition frequency was 100 kHz. The clamping units were kept at nominal surface pressure of 6 bars. The inner diameter of the circular clamping unit was 100 mm, the free surface of the rectangular clamping unit measured 125 x 75 mm². The diameter of the hemispherical striker tip was 20 mm (fig. 5.2).

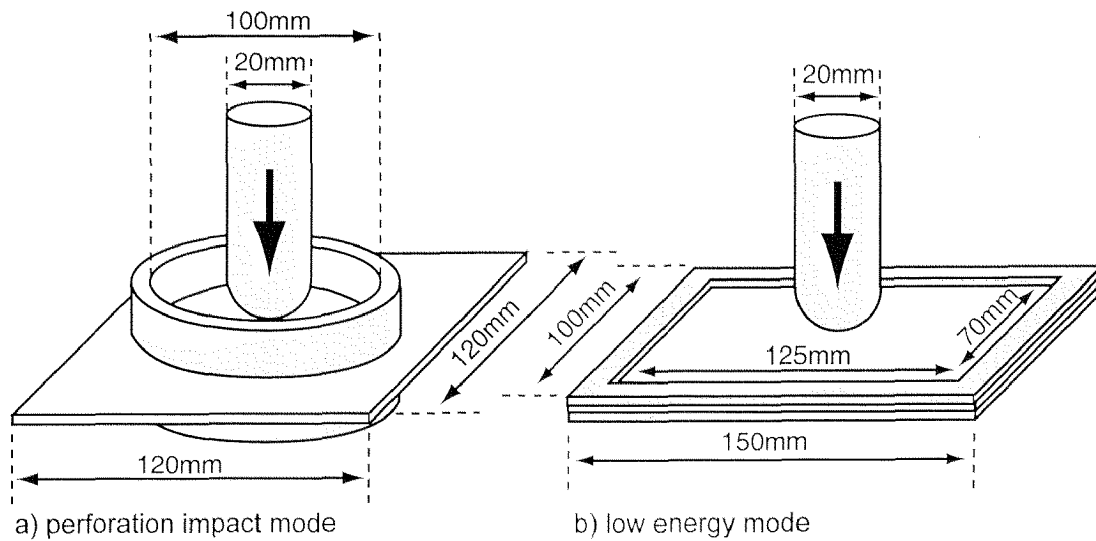


Figure 5.2: Experimental setup of falling weight impact testing. Circular clamping units were used for perforation (a), rectangular for low energy impact testing (b). The striker geometry was similar in both experiments.

Low energy and perforation tests were performed on panels with different thicknesses at room temperature under the conditions described in table 5.1.

material	thick-ness [mm]	mode	clamping unit [mm]	impactor mass [kg]	impactor speed [m/s]	impact energy [J]
CF/PEEK	1.26 (4 DL)	Perforation	circular, d = 100	3	2.83	12
CF/PEEK	1.81 (6 DL)	Perforation	circular, d = 100	3	3.65	20
CF/PEEK	1.26 (4 DL)	Low energy	rectangular 125 x 70mm	3	1.53	3.5
GF/PET (amorphous)	1.35 (3 DL)	Perforation	circular, d = 100	3	4.47	30
GF/PET (semicrystalline)	1.81 (4 DL)	Perforation	circular, d = 100	5.17	4.81	60

Table 5.1: Experimental conditions of low energy and perforation impact testing as applied in this study. Impact energy was controlled by the initial falling height of the impactor. In perforation impact, sufficient energy was applied to penetrate the specimen while the impactor speed was intended to be reduced to a minimum after perforation. In low energy mode, impact energies high enough to study failure initiation were chosen.

5.3. Results and discussion

5.3.1. Perforation impact

CF/PEEK

Impact data. CF/PEEK samples with different numbers of double layers were subjected to falling weight impact. Force/velocity vs. time and force/energy vs. displacement plots of 4 DL (1.26 mm) and 6 DL (1.81 mm) KFRC samples are shown in figure 5.3.

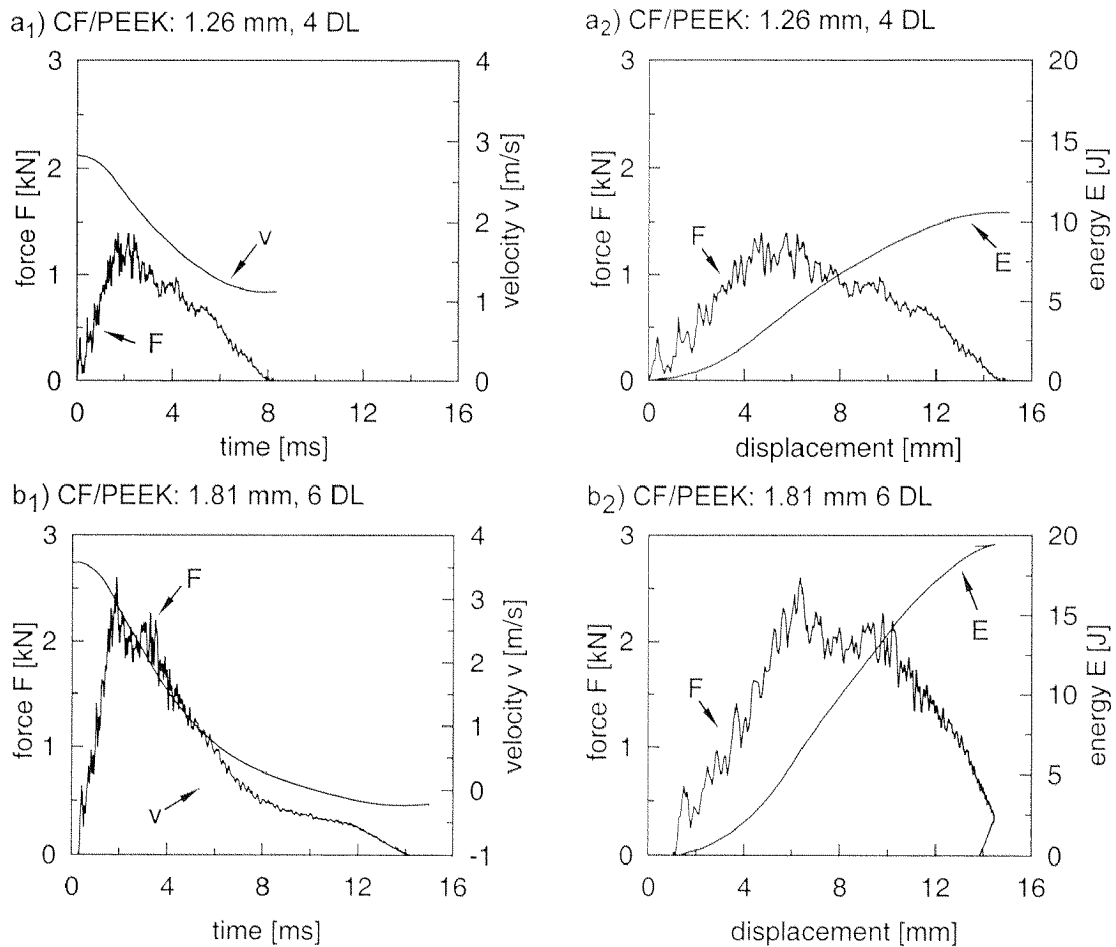


Figure 5.3: Force-time and force-displacements plots of perforation impacted knitted CF reinforced PEEK panels with different thicknesses. Impact energies were 12 and 20 J in the case of 4 and 6 DL, respectively (table 5.1).

Displacements required for complete perforation of the samples were approximately the same in both cases, which leads to the assumption that maximum displacement is related to the knit structure. Perforation time was longer in the case of the thicker specimen. This is attributed to the velocity of the striker which decreased below zero in perforation of

the 6 DL specimen (fig. 5.3, b₁). This means that the striker was slightly rebounded at the end of the impact test whereas it was not stopped by the perforation of the 4 DL specimen (fig. 5.3, a₁). The fact that maximum displacement of perforation was barely influenced by the thickness suggests that the loop size, more generally the knit structure is limiting the maximum deformation reached at complete perforation.

Pronounced load oscillations indicate considerable damage development immediately after impactor contact. In an earlier investigation on woven CF reinforced PEEK composites, the first peak in the force-time curve was at or close to maximum force and crack initiation was correlated with this point [135]. In the samples studied in this work however, it is suggested that cracking occurs well before the peak force is reached. The peak force is correlated with the production of a major defect across the specimen, as described in [136].

The peak force was found to be dependent of the panel thickness. The thickness specific peak forces, i.e. peak force divided by sample thickness of 4 and 6 DL CF/PEEK samples are given in table 5.2. A slightly lower specific peak force was found for the thinner samples. This could be a consequence of the lower initial velocity and/or the lower bending stiffness related to the thinner specimens.

	peak force [kN/mm]	initiation energy [J/mm]	propagation energy [J/mm]	dissipated energy [J/mm]	ductility index []
4 DL (1.26 mm) CF/PEEK	1.1 ± 0.1	2.8 ± 0.8	6.1 ± 0.7	9.0 ± 0.4	0.69 ± 0.08
6 DL (1.81 mm) CF/PEEK	1.4, 1.4	3.5, 4.4	7.1, 6.5	10.7, 10.9	0.7, 0.6

Table 5.2: Characteristical impact values of knitted CF reinforced PEEK (4 DL: n=4, 6 DL: n=2). All values are normalized by thickness. Better results are reached for 6 DL, more energy per thickness can be dissipated in the thicker samples.

The thickness specific energy transferred up to peak load, i.e. initiation energy was found to be slightly lower for 4 DL than for 6 DL samples. The same trend was observed for the total dissipated energy (table 5.2). The most likely reason for these vague tendencies are the higher shear component in thicker panels, leading to pronounced bundle release in the damage zone (fig. 5.5).

Damage zone. The macroscopical perforation impact damage is presented in figure 5.4. The fracture path was found to follow wale and course direction (arrows). Outside of the striker mark (A), visible damage was limited to a few millimeters and was mainly caused by localized buckling of the bundles. In order to investigate microscopical failure behavior the tested specimens were platinum sputtered (10 mA for 600 s) and investigated in a scanning electron microscope.

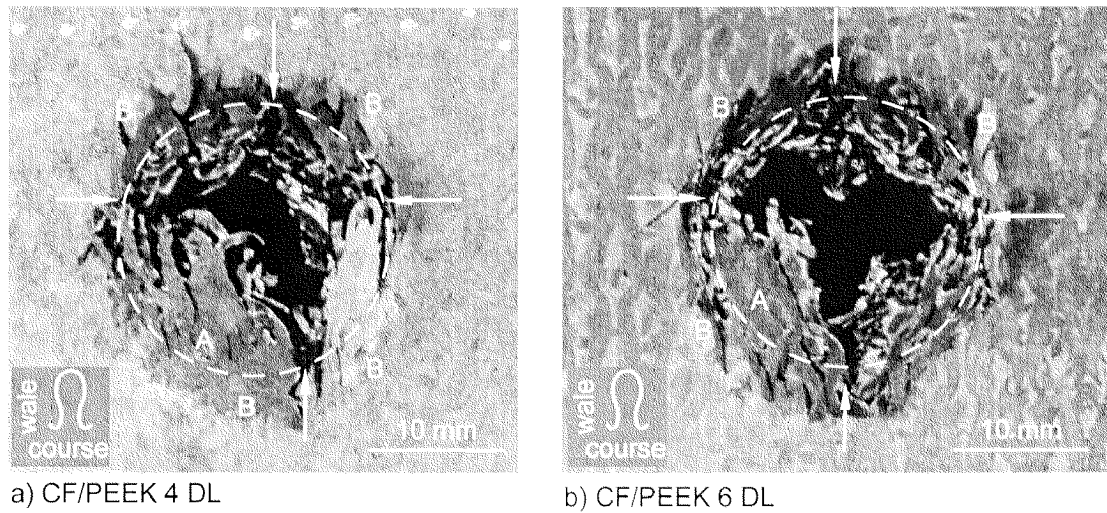


Figure 5.4: Perforation impact damage of knitted CF reinforced PEEK. The macroscopical fracture path followed the two principal directions wale and course (arrows). Visible damage mainly caused by localized buckling (B) remained within a few millimeters outside of the striker mark (A).

On the microscopical level, bundle released from their environment were observed in the damage zones (fig. 5.5). Similar to the results found in the investigation of out-of-plane failure (chapter 4), bundles represented the smallest units in the fracture surface.

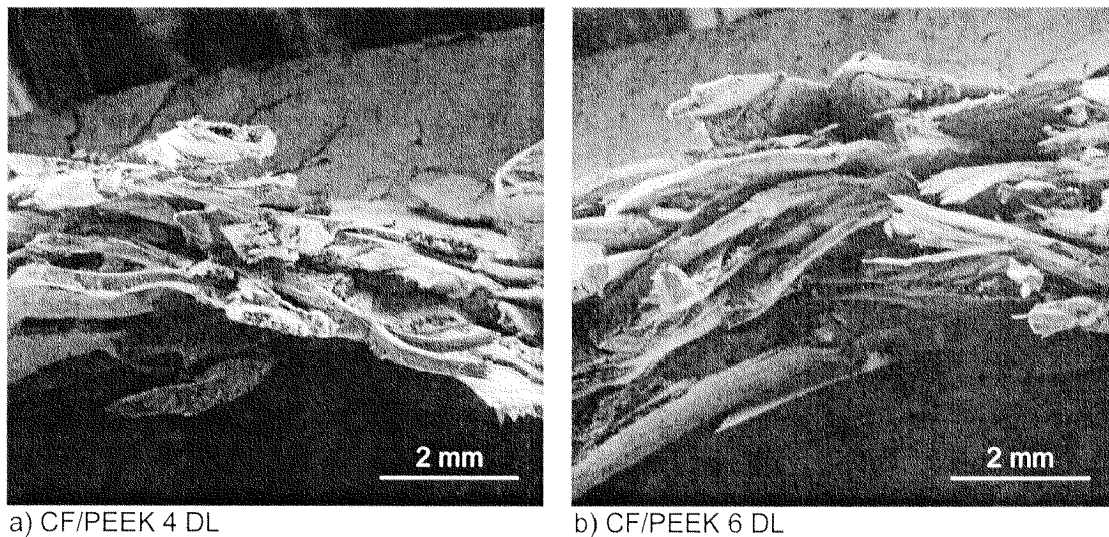


Figure 5.5: Damage zones resulting from perforation impact. Bundles released from their environment were observed in 4 DL (a) and 6 DL (b) samples. A higher tendency of bundle release was found in thicker samples.

The degree of bundle release was found to be tenuously higher in the thicker samples. This is supposed to be a result of the higher in-plane stresses and is consistent with the superior energy dissipation determined in thicker samples (table 5.2).

In order to investigate interlaminar fracture, the samples were cut through the primary damage zone, using a diamond saw. Delamination was observed in some cases (fig. 5.6 a, arrow). As observed in figure 5.4, damage did not propagate significantly outside of the buckling zone (C).

Delaminated parts were separated from the bulk and investigated by SEM (fig. 5.6 b, c). Interlaminar fracture surfaces did not remain in between two knit layers. Bridging to other knit layers was observed (B) and bundle failure was involved (A). The energetically most favorable interlaminar fracture path was not defined by knit layers. This is a further confirmation of the intensive interpenetration of knit layers observed in the studied KFRCs (see also chapter 3).

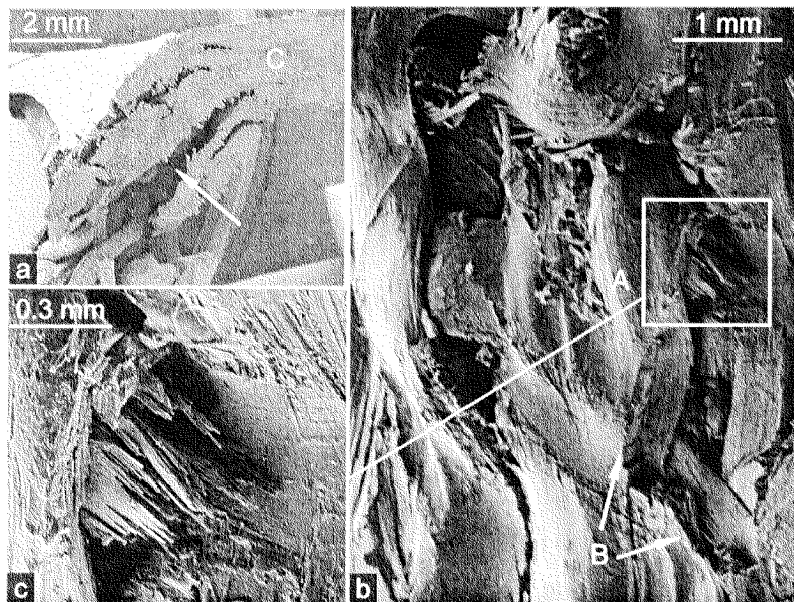


Figure 5.6: Interlaminar fracture caused by perforation impact (CF/PEEK, 6 DL). Interlaminar fracture only occurred in the primary damage zone (a, arrow). The resulting interlaminar fracture path (b) did not remain between individual knit layers. Bridging to other layers (B) and bundle failure (A) were involved.

GF/PET

Impact data. Knitted GF reinforced composite panels of different thicknesses, with amorphous and semi-crystalline PET matrix were subjected to perforation impact. Force/velocity vs. time and force/energy vs. displacement data is shown in figure 5.7.

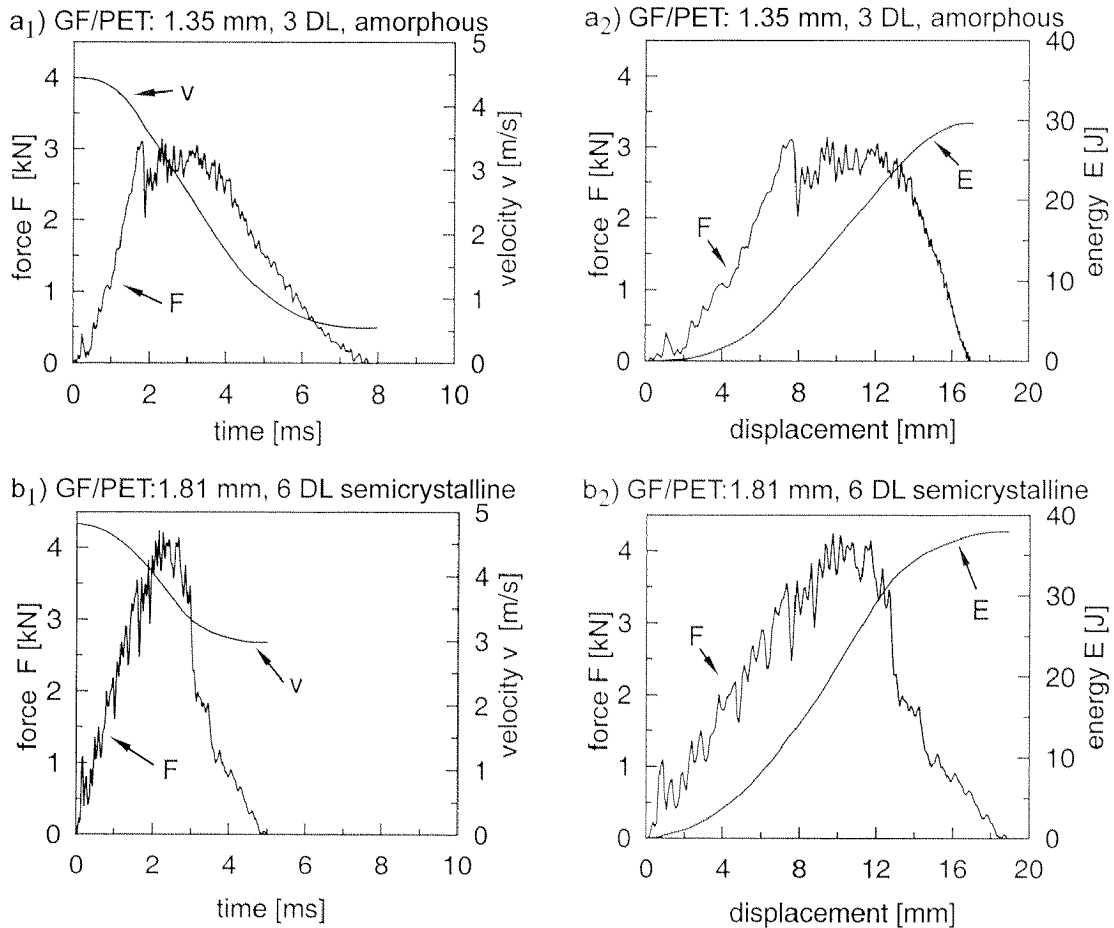


Figure 5.7: Perforation impact response of knitted GF reinforced PET. Up to peak force, the force-displacement curve of the amorphous sample was observed to be smoother than the force-displacement curve of semicrystalline GF/PET, which is an indication of a later damage initiation than in semicrystalline GF/PET. The striker displacement at completed perforation of the panels was approximately similar in both cases.

Maximum displacement at completed perforation was approximately similar for amorphous and semicrystalline GF/PET. Because the same maximum displacement value was also observed for CF/PEEK, this is supposed to be related with the reinforcement structure rather than fiber/matrix material.

The fact that more time was needed for perforation of the thinner, amorphous specimens was attributed with the speed of the striker. While it was almost reduced to zero in the case of the semicrystalline samples, more than 3 m/s were measured after perforation of the amorphous GF/PET panels.

The force-time curve devolution of the amorphous sample is relatively smooth up to peak force, followed by a load drop and numerous peaks, indicating damage initiation and propagation. In the case of semicrystalline GF/PET, a multi-peaked force-time curve

from the beginning on suggests very early damage initiation. In contrast to the amorphous samples, the load level was not maintained at peak force but dropped down to zero within 2 ms. This behavior is assumed to be related to the higher brittleness of the semi-crystalline PET matrix (see chapter 2, table 2.2).

The average thickness specific characteristic impact values of 5 independent impact experiments are given in table 5.3.

	peak force [kN/mm]	initiation energy [J/mm]	propagation energy [J/mm]	dissipated energy [J/mm]	ductility index []
amorphous GF/PET (3 DL, 1.35 mm)	2.4 ± 0.2	10.1 ± 1.0	11.3 ± 1.0	21.4 ± 0.5	0.53 ± 0.05
semicrystalline GF/PET (4 DL, 1.81 mm)	2.2 ± 0.1	11.6 ± 1.2	7.7 ± 1.7	19.3 ± 1.5	0.40 ± 0.07

Table 5.3: Characteristical impact values of perforation impact energy impacted knitted GF reinforced PET ($n=5$). For better comparability, the values are thickness normalized. The higher ductility index of amorphous GF/PET reflects the different failure characteristics.

Propagation energy was significantly higher in amorphous than in semicrystalline GF/PET, whereas peak force and initiation energy were similar for both materials. This leads to a higher ductility index for amorphous GF/PET which again reflects its less brittle failure characteristics.

Damage zone. The macroscopical damage caused by perforation impact in amorphous (a) and semicrystalline (b) knitted GF reinforced PET is shown in figure 5.8. The more ductile failure of amorphous GF/PET is evident (a). Damage outside of the impactor mark occurred in wale direction (A), which is the direction of the lowest resistance to crack propagation (see chapter 4). Bundles released from their environment (B) were predominantly observed in the semicrystalline samples (b). In comparison to the macroscopical impact zones of impacted CF/PEEK samples (fig. 5.4), more damage was observed outside of the striker marks (C).

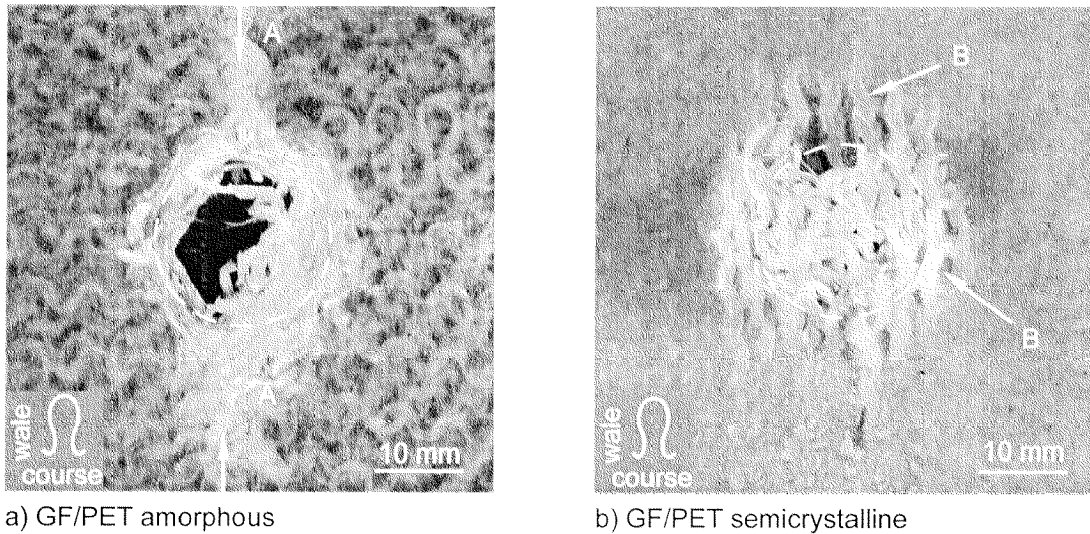


Figure 5.8: Macroscopical damage in perforation impacted knitted GF reinforced PET with amorphous (a) and semicrystalline matrix (b). Ductile failure with damage propagating in wale direction (A) was observed in the amorphous samples. In semicrystalline GF/PET, damage is mainly characterized by bundles released from their environment.

SEM micrographs of perforation impacted GF/PET samples are shown in figure 5.9. Interlaminar bundle release along bundle/matrix interfaces was found to be more dominant in semicrystalline GF/PET (A). This is assumed to be related with the higher interlaminar shear stresses in thicker samples. Fibers released from bundles (B) were observed in amorphous and semicrystalline GF/PET. This is in contrast to the fracture surfaces of CF/PEEK in which the smallest isolated units consisted of bundles (fig. 5.5).

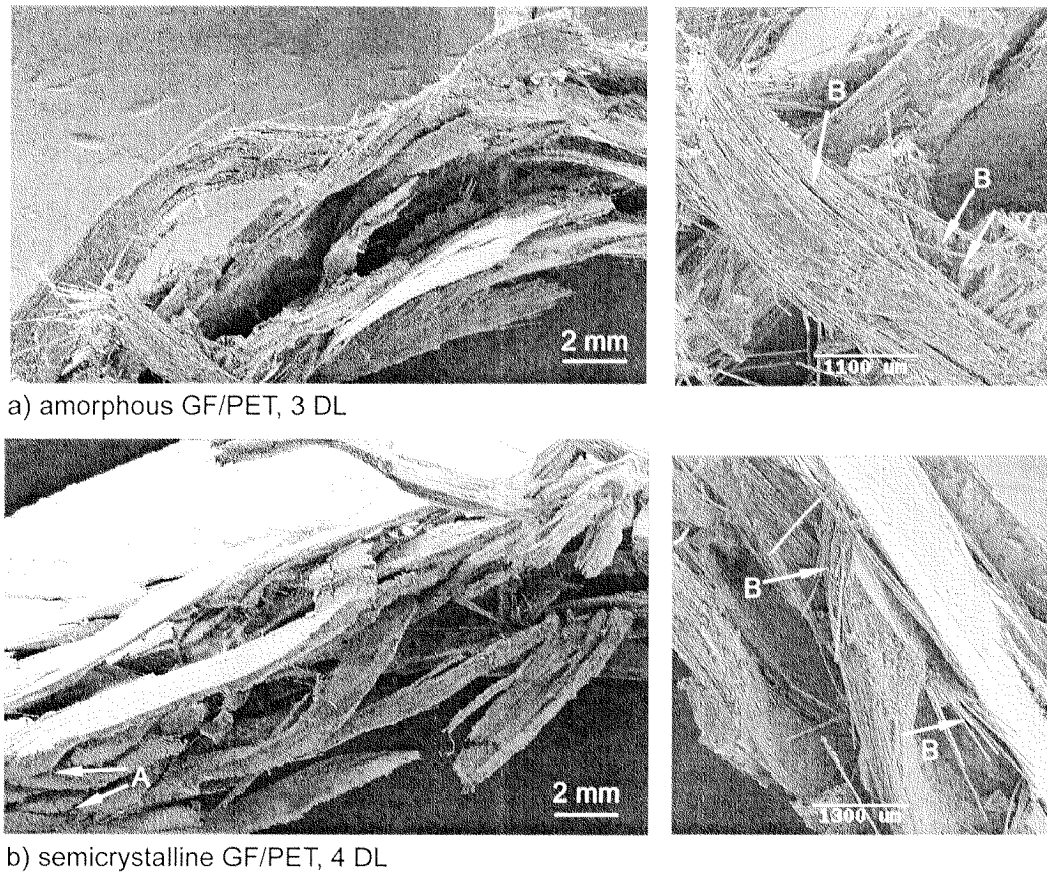


Figure 5.9: Microscopical fracture surfaces resulting from impact perforation of GF/PET. Fracture along bundle/matrix interface was observed to a higher degree in the thicker semicrystalline samples. Fibers released from bundles were observed in amorphous and semicrystalline GF/PET.

5.3.2. Low energy impact

Knitted CF reinforced PEEK samples consisting of 4 DL were subjected to low energy impact experiments. In this mode, the impactor hits the samples with an energy low enough (3.5 J) to be rebounded from the sample surface.

Impact data. Force-time and force-displacement plots are shown in figure 5.10. Load oscillations up to peak force and a non-symmetrical force-time plot (a) with respect to ascent and descent part indicate considerable damage development. The total dissipated energy corresponds to the area of the force-displacement plot hysteresis (b).

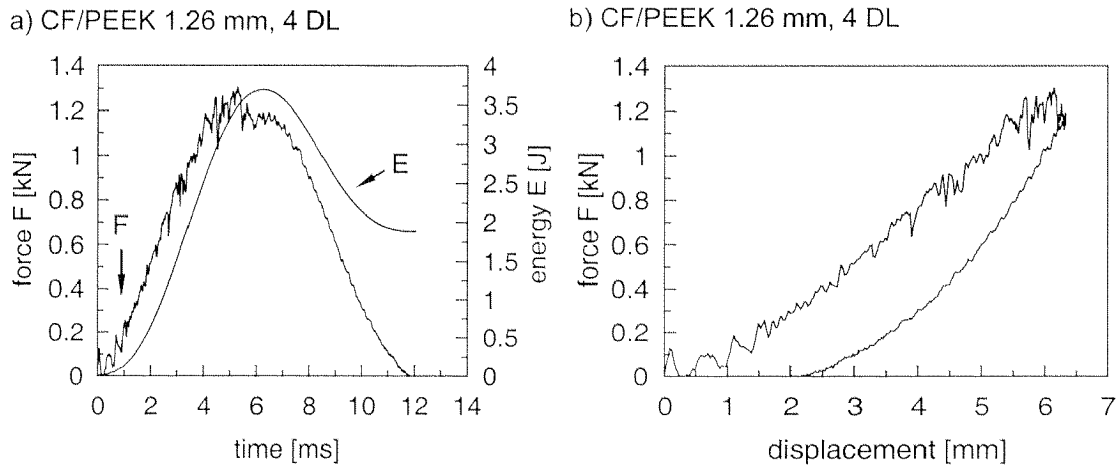


Figure 5.10: Force/energy-time (a) and force-displacement (b) curves of knitted CF reinforced PEEK composite panels (4 DL) subjected low energy impact. The non-symmetrical force-time plot (a) and load oscillations up to peak force indicate considerable damage development. The area of the force-displacement hysteresis (b) corresponds to the total dissipated energy.

The characteristic impact values of low energy impacted CF/PEEK are presented in table 5.4. The peak force reached in perforation and low energy impact were found to be approximately similar. This suggests that maximal force was dependent on material and sample thickness rather than on the applied impact energy.

	peak force [kN/mm]	dissipated energy [J/mm]
4 DL (1.26 mm) CF/PEEK	1.0 ± 0.1	1.4 ± 0.3

Table 5.4: Characteristic values of low energy impact. The thickness specific peak force was found to be in the same range than peak force reached in perforation energy testing (table 5.2). Peak force and dissipated energy were normalized by their thickness.

Damage zone. The tension surface (bottom) of a CF/PEEK sample is shown in figure 5.11. The cracks caused by low energy impact reflect the structure of the knitted carbon fiber bundles (A). This observation emphasizes the crucial role of the bundle/matrix interface in knitted GF reinforced PEEK: Damage was initiated at the bundle/matrix interface (fig. 5.11), and bundles were the smallest released units observed in perforation impact (fig. 5.5) and compact tension (chapter 4) fracture surfaces.



Figure 5.11: Tension surface (bottom) of a CF/PEEK sample subjected to low energy impact. The cracks were initiated along the bundle/matrix interface (arrows) and therefore, reflect the knitted CF bundle structure (A). This observation confirms the crucial role of bundle/matrix interfaces in knitted CF reinforced PEEK. Bundles released from their environment were the smallest units in all observed fracture zones (see also fig. 5.5, chapter 4).

5.4. Conclusions

5.4.1. Comparison of CF/PEEK and GF/PET

The most remarkable difference in the impact behavior of the two investigated KFRCs is the fact that twice as much energy was dissipated in knitted GF reinforced PET than in CF reinforced PEEK. Since both composites are based on a similar reinforcement structure, the reason is assumed to be related to fiber/matrix materials and/or fiber/matrix interface properties. The most obvious differences of the materials are the followings:

- The ratio tensile/compression properties of glass fibers is closer to 1 than that of carbon fibers (ratio < 0.5).
- Fiber/matrix interface strength of GF/PET is lower than that of CF/PEEK.
- CF/PEEK knits reveal a higher stiffness than GF/PET knits. In tensile test, E-moduli in wale direction of approximately 15 GPa and 49 GPa were found for GF/PET [106] and CF/PEEK [46], respectively.

The compression properties of the reinforcing fibers are considered to be of relatively low importance for the impact resistance of the studied KFRCs. Even though higher compression properties lead to better bending strength, the fibers failed in tension rather than in bending. This can be understood considering the high tensile stress in the damage area, induced by the small impactor compared to specimen size and by clamping of the specimens. The interface strength and stiffness however, are supposed to lead to the superior impact energy dissipation ability found for GF/PET: Up to a certain extend, poor interface adhesion leads to the absorption and distribution of the initial impact

energy and therefore increases the impact performance [137]. The total fracture surface area of an impact damage involving fiber/matrix interface (GF/PET: fig. 5.9) failure is higher than the fracture area resulting from bundle release only (CF/PEEK: fig. 5.5).

The lower stiffness of GF/PET knits results in higher deformation upon completed perforation. The higher degree of localized buckling of bundles in CF/PEEK (fig. 5.4: CF/PEEK, fig. 5.8: GF/PET) is assumed to be caused by its stiffness, being three times higher than the stiffness of GF/PET.

The role of the matrix can be assessed by the differences found for the amorphous and semicrystalline PET matrix. The impact response of amorphous GF/PET samples was characterized by few load oscillations up to peak force and damage development at peak force level. In semicrystalline samples, most damage was brought in before peak force was reached (fig. 5.7). These observations can be understood when considering the much higher elongation at break of amorphous (300%) compared with semicrystalline PET (70%). The early failure of the brittle semicrystalline matrix is reflected in the early oscillations of the force-time plot. In total, because of the pronounced bundle release in these samples (fig. 5.8), almost as much energy could be dissipated. However, late damage initiation, as found for the amorphous matrix system, is desirable.

5.4.2. Comparison with other composite materials

Numerous researchers studied the impact response of composite sheets [87, 88, 135, 136, 138-142]. Table 5.5 gives an overview of selected results reported in the literature. When comparing results the experimental conditions have to be taken into account. The impact response of fiber reinforced composites is highly dependent on experimental conditions such as clamping devices, impactor dimension and velocity at impact. It even has been stated that a comparison of results from different sources is "impossible" [143]. Nevertheless, table 5.5 is intended to give a survey of impact properties of different composite materials. Experimental parameters and source are indicated. The impact performance of the studied KFRCs is situated in the upper range of table 5.5.

Material	Fiber architecture	Fiber Cont.	thickness [mm]	Clamping unit (s= square, r=ring) [mm]	Impact mass [kg]	Max. speed [m/s]	Striker diameter [mm]	Peak force [kN/mm]	Dissipated energy [J/mm]	Ductility Index DI	Source
GF/PP	(±2.2)SS	35% v	3.3	50 (r)	—	5	12.7	0.43	32	0.67	[141]
GF/PP	cross-plyed (0/90)2S	35% v	3.3	50 (r)	—	5	12.7	0.42	25	0.40	[141]
GF/PET	knitted fabric reinforced	50% v	1.4 - 1.8	100 (r)	5.2	4.8	20	2.2 - 2.4	19 - 21	0.4 - 0.53	p.w.
GF/PP	quasi-isotropic (-45/+45/0/90)S	35% v	3.3	50 (r)	—	5	12.7	0.43	16	0.52	[141]
GF/PP	knitted fabric reinforced	31% w	2.5	90 (s)	3.53	4	12.7	1.48	14	—	[87]
GF/PP	swirl glass mat (GMT)	35% v	2.5 - 3.5	40 (r)	5.17	10	20	—	8	0.75	[88]
GF/PA66	short fibers injection moulded	33% w	2	50 (r)	8.5	3	12.5	0.25	1.2	0.77	[135]
CF/PEEK	knitted fabric reinforced	51% v	2.5 - 3.5	40 (r)	5.17	10	20	2.2	14 - 16	0.5 - 0.7	[88]
CF/PEEK (APC-2)	cross-plyed (0/90)4S	62% v	2.2	50 (r)	—	5	12.5	—	11.5	0.74	[135]
CF/PEEK	knitted fabric reinforced	52% v	1.3 - 1.8	100 (r)	3	3.7	20	1.1 - 1.4	9 - 11	0.6 - 0.7	p.w.
CF/PEEK (APC-2)	quasi-isotropic (-45/90/+45/0)2S	62% v	2.2	50 (r)	—	5	12.5	1.64	9.4	0.68	[135]
CF/PEMA	knitted fabric reinforced	35% v	2.5 - 3.5	40 (r)	5.17	10	20	1.2	8 - 10	0.6 - 0.8	[88]
CF/Epoxy	cross-plyed (0/90)4S	62% v	2.1	50 (r)	—	5	12.5	—	8.0	0.65	[135]
APC-2 /AS4	quasi-isotropic laminates	60% v	2	130 (r)	0.65	5.9	6.35	—	7.5	—	[142]
CF/Epoxy	quasi-isotropic (-45/90/+45/0)2S	62% v	2.2	50 (r)	—	5	12.5	1.35	7.3	0.76	[135]
CF/Epoxy	quasi-isotropic laminates	60% v	2	130 (r)	0.65	5.9	6.35	—	5	—	[142]

Table 5.5: Impact performance of various composite systems tested with different experimental conditions (— not available, p.w.: present work).

5.4.3. General conclusions

The falling weight perforation impact response of knitted fabric reinforced CF/PEEK and GF/PET was studied. Furthermore, CF/PEEK was subjected to low energy impact. Damage zones and fracture surfaces were inspected with respect to macro- and microscopical damage.

CF/PEEK panels consisting of 6 DL exhibited a slightly higher thickness specific total dissipated energy than the thinner CF/PEEK composite, consisting of 4 DL (table 5.2). This is assumed to be related with a higher shear component in thicker panels at given clamping and striker dimensions. With respect to the damage zone, this effect could be confirmed with more pronounced bundle release observed in the thicker CF/PEEK samples (fig. 5.5).

Delamination along the reinforcing knit layers did not occur, neither in GF/PET nor in CF/PEEK. In general, energy was dissipated by bundle release (CF/PEEK) and failure of the fiber/matrix interface (GF/PET). In cases in which delamination was detected, the interlaminar fracture propagated across several knit layers by bridging. The interlaminar fracture surface shown in figure 5.6 exhibits layer bridging involving even bundle failure. The fact that the energetically most favorable fracture plane is not observed between two knit layers is a confirmation of the effective interpenetration observed in the analysis of the 3D structure of KFRCs (chapter 3).

A common aspect in static and dynamic failure behavior of knitted CF reinforced PEEK is the fact that the smallest isolated units in damage zones are represented by bundles released from their environment (fig. 5.5, chapter 4). Damage was initiated along bundle/matrix interfaces which was shown in the fracture surface resulting from low energy impact (fig. 5.11). In contrast to GF/PET, fibers released from bundles were not observed. This is assumed to be a consequence of the higher fiber/matrix interface strength of CF/PEEK compared to GF/PET. Whereas high interface strength represents an advantage for the static properties, it was found to reduce the energy dissipation ability in perforation impact. A comparable effect is caused by the higher stiffness of CF/PEEK which is assumed to facilitate localized out-of-plane buckling of the bundles in perforation impact (fig. 5.4). The smaller deformation at a given impact force is supposed to lead to early bending failure and therefore, reduces total dissipated impact energy. The more compliant behavior of GF/PET, in contrast, enables a better distribution of the impact stress on a larger area, which was shown in the analysis of the damage zone. A larger damage zone and more fracture surface area were observed, thus indicating a higher dissipation of energy.

The most damage tolerant and therefore, the most desirable impact behavior was found in knitted GF reinforced, amorphous PET. Even though the total dissipated energy was approximately similar to semicrystalline GF/PET, damage initiation and propagation occurred at high force levels in amorphous GF/PET, whereas load oscillations initiated at striker contact indicate more brittle failure of semicrystalline GF/PET (fig. 5.10). For the automotive industry, in which weight-saving considerations are of minor and cost saving

of major importance, knitted GF/PET with amorphous matrix represents a very interesting material for impact relevant applications.

In summary, the impact resistance of the studied KFRCs was found to be high. Both, GF/PET and CF/PEEK exhibited good energy dissipation ability in comparison with other glass fiber and carbon fiber reinforced polymers. This is assumed to be related with the pronounced interpenetration of knit layers, thus increasing delamination resistance of the KFRC panels. Instead of delamination, bundles released from their environment were observed predominantly. Highest values for dissipated energy were found for amorphous GF/PET, exhibiting a relatively weak fiber/matrix interface, low stiffness in comparison to CF/PEEK and a matrix with high elongation at break.

6. INFLUENCE OF ENVIRONMENTAL EXPOSURE ON THE MECHANICAL PROPERTIES OF KFRCs

6.1. Introduction

The stability of fiber reinforced polymers (FRPs) to environmental exposure is of major importance. As described in chapter 1.2, the nature of FRPs makes them particularly sensitive to environmental influences, mainly because of two reasons: First, fiber/matrix interfaces are locations of stress transfer and therefore, a degradation of interfacial strength can lead to a significant decrease of the composite strength, even when fiber and matrix properties are not affected. Secondly, polymers are not impermeable to water molecules and many of them are known to be sensitive to the effect of moisture and temperature. Hygrothermal environments influence the mechanical behavior of FRPs mainly by fiber and/or matrix degradation and by fiber/matrix interface degradation.

Knitted GF reinforced PET and knitted CF reinforced PEEK are the two composite systems investigated in the presented work. The basic properties of fiber and matrix materials are given in chapter 2. The environmental stability of CF/PEEK knits was studied with respect to biomedical applications. Longterm exposure to simulated body fluid (SBF) at 37, 60 and 90°C was investigated. SBF contains physiological concentrations of mineral components from body fluids. SBF and body temperature (37°C) were chosen for comparison with body environments. Exposure for up to 50 weeks at higher temperatures were performed in order to accelerate potential effects of SBF to CF/PEEK. It is important to consider longterm stability of implant materials, since certain implants, e.g. hip joint prostheses, are intended to remain in the body environment over several decades. The hygrothermal stability of knitted GF reinforced PET was studied under relatively extreme environmental conditions (90°C, immersion in water). The decrease of mechanical properties was determined and conclusions are drawn with respect to structural applications of GF/PET in the automotive industry.

A further objective of this chapter was to evaluate the influence of matrix and fiber/matrix interface degradation on the macromechanical properties of KFRCs. In chapter 7, the influence of the same environmental conditions on micromechanical interface properties will be discussed and an attempt will be made to correlate macro- and micromechanical degradation.

6.1.1. Environmental stability of CF/PEEK

PEEK is a thermoplastic polymer which shows an excellent resistance to most inorganic and organic solvents. Since PEEK is evaluated for high performance applications, its performance in hostile environments has been investigated by many researchers. The presented study is focussed on the influence of hygrothermal environments with respect

to biomedical applications, therefore, effects of aviation fluids such as paint stripper, hydraulic fluids and jet fuel will not be discussed.

Thermal degradation. Longterm exposure to elevated temperatures below T_g is defined as physical aging. The mechanical properties of amorphous PEEK are reported to be influenced by physical aging. Relaxation mechanisms occurred between 50 and 140°C, leading to a higher tensile yield strength and a significant reduction of impact strength of unreinforced PEEK [144]. Longterm thermal aging (temperatures between T_g and T_m) is reported to cause a significant decrease in flexural strength of CF/PEEK (APC-1) unidirectional and cross-ply laminates only if exposed to 250°C for more than 16 weeks [145]. Effects of physical and thermal aging were studied by Leach and Cogswell [146]. Thermal aging lead to a 30% reduction of the transverse flexural strength of unidirectional CF/PEEK (APC-1) after 8 weeks at 220°C, whereas physical aging caused no significant difference to unexposed samples. Ma [147] studied impact performance and mode I fracture toughness of CF/PEEK (APC-2) after physical aging between 70°C and T_g for 14 days. Dissipated impact energy and fracture toughness were observed to decrease. The highest reduction was found for aging temperatures close to T_g .

Generally, it was found that physical aging ($<T_g$) shows only slight influences on the mechanical properties of CF/PEEK. Some minor effects determined in matrix dominated properties were related with the relaxation mechanisms of neat PEEK occurring below T_g [148]. In contrast, thermal aging ($>T_g$) greatly affected the matrix and composite properties. However, with respect to medical applications, the effects of temperatures above T_g are not discussed in the presented work.

Hygrothermal degradation. Equilibrium water absorption of unreinforced PEEK was found to be at approximately 0.2% by weight [149]. Immersion of quasi-isotropic CF/PEEK for 17 months lead to a water content of 0.34% [150]. Other work on APC-1 reported about 0.45% mass gain in boiling water after 3 weeks [151]. Little effect of water absorption on the properties of unreinforced PEEK are described in literature. Differences in strength remained within 5% after 322 days exposure to water at 100°C [148]. As for thermal degradation, matrix dominated mechanical properties were mostly affected by hygrothermal degradation. Ma [40] observed that tensile strength in longitudinal direction of CF/PEEK composites was not affected, while the flexural strength decreased to about 90% of the initial value after immersion in water at 80°C for 118 days. In contrast to this, no effect on the flexural properties after exposure to water at 70°C until equilibrium water absorption was determined in [151]. The immersion of unidirectional CF/PEEK (APC-2/AS4) in water at 23°C and 50°C exhibited no significant effects on the fatigue crack propagation in transverse direction [152].

Degradation at physiological conditions. Investigations including exposure to physiological solutions and to environments at 37°C were performed for the evaluation of CF/PEEK in biomedical applications. Storfer-Isser investigated the transverse properties of APC-2 after exposure to water at 37°C [41]. After 16 weeks, both, transverse tensile

and transverse compression properties were found to decrease to about 75% and 90% of the initial values, respectively. This reduction was related to changes in the crystallinity of the matrix. Maharaj investigated compressive and flexural properties of CF/PEEK in lactated Ringer's solution and observed no significant effects at 37°C, whereas a 16% reduction resulted from 1.5 years exposure at 90°C [32]. Meyer measured the ultimate bond strength of PEEK microdroplets on single carbon fibers after exposure to physiological saline at 37, 65 and 95°C for 5000 hours [28]. He found significant reduction of interfacial properties as a function of both, time and temperature. The same study was extended to material specific acellular inflammatory exudate harvested from rabbits [26]. The decrease of interfacial bond strength was attributed to diffusion of water and/or salt ions into the samples and interaction with the CF/PEEK interface. Zhang investigated the long-term compressive properties of CF/PEEK composites and found no significant effects after 5000 hours in physiological saline at 95°C [38].

Summarizing the reviewed studies, it is noted that the results are partly oppositional. Some studies reported a significant influence on flexural, impact and interface strengths of CF/PEEK, while other authors noted no effects under the same environmental exposure parameters. If effects on mechanical properties were observed, it is generally accepted, that matrix and matrix dominated properties were most affected by thermal and hygrothermal exposure.

6.1.2. Hygrothermal stability of GF/PET

The E glass fibers used in this work exhibit a high hydrolytic resistance [153]. Polarized water molecules are strongly bonded to SiO⁻ and AlO⁻ residues on glass fiber surfaces. Temperatures of 500°C are needed to remove the adsorbed water [154]. Therefore, with respect to hydrolytic degradation, the properties of matrix and fiber sizing are of higher importance than the fibers, because the latter are considered stable in hydrous solutions even at elevated temperatures. The fiber sizing is a well kept secret of the manufacturer. In most cases, sizing is a aqueous dispersion or solution, consisting of keing agents¹, filmformers², lubricants and other components [154]. In contrast to thermosetting matrices, the sizing is usually not intended to undergo chemical reactions with thermoplastic matrices because the latter are mostly unreactive. A more important contribution to the fiber/matrix bonding is the fact that thermoplasts wet and adhere to certain filmformers, e.g. epoxides or polyvinyl acetate. Since the sizing is mainly responsible for the fiber/matrix interface bonding, degradation of the sizing results in decreasing mechanical properties of glass fiber reinforced polymers.

Poly(ethylene-terephthalate) (PET) decomposes in water. At 25°C, the degradation process is very slow which is important with respect to the use of PET as water contain-

-
1. family of chemicals which can co-react with the resin during polymerization, thus forming a chemical bridge between fiber and matrix
 2. suspension of polymeric particles (often polyvinyl acetate) in aqueous medium

ers. Only approximately 0.1% of the ester groups decompose in ten years [155]. At higher temperatures, degradation is faster and accelerated in an autocatalytic fashion. The carboxyl end groups (-COOH) which are formed at the terminus of the polymer fragments and molecules of terephthalic acid may act as active catalysts of the degradation [155]. Zimmermann investigated the thermal and hydrolytic degradation of PET and found that a high initial -COOH contents increased the degradation speed significantly which is coherent with the concept of autocatalytic degradation [156]. This is important, considering that the initial -COOH content strongly depends on thermal degradation, occurring throughout composite processing at temperatures of 280 - 320°C. Jabarin emphasized the promoting effect of higher processing temperatures on the formation of -COOH groups [157]. An extended study on the effect of water sorption on PET and its long fiber composites at temperatures up to 87°C was performed by Bastioli [158]. He observed a quasi-equilibrium water uptake of approximately 1.1%, accompanied by a decreasing molecular weight (MW) to about 25% of the initial MW after 750 hours immersion in water at 87°C. Similar to the studies described above, Bastioli found a significant increase of carboxyl end groups. The degradation lead to a significant decrease of the fracture toughness of neat and glass fiber reinforced PET which was attributed to the embrittlement by hydrolysis. Water absorption at relative humidity (RH) from 32 to 90% at 23°C lead to a water uptake of 0.7% by weight, accompanied by a decrease of T_g , molecular orientation, yield stress and ultimate stress [159]. In summary, it is reported, that hygrothermal exposure of PET and its glass fiber composites leads to hydrolytic degradation of PET and therefore of the fiber/matrix interface. Effects on the fibers were not observed. The degree of degradation depends on environmental parameters and the initial chemical composition of PET.

6.2. Methods

CF/PEEK and GF/PET knitted reinforced composite panels were processed according to chapter 2.2. Four-point (4-pt) bending was performed to determine standard mechanical properties, i.e. strength and elastic modulus. Experimental parameters of the 4-pt bending test as applied in this work are described below. Failure behavior, fracture toughness and impact response were studied using out-of-plane compact tension (chapter 4) and falling weight impact (chapter 5). The results described in these chapters serve as reference for the comparison of unexposed and exposed samples. Characterization methods, sample dimensions and experimental set-ups are described in the respective chapters.

6.2.1. Environmental conditions

To investigate the environmental effects, samples were exposed to selected temperatures, media and exposure times as shown in table 6.1. Knitted CF reinforced PEEK is of interest for both, medical and technical engineering applications. Therefore, the influence of

immersion in simulated body fluid (SBF) as well as exposure to hot water was investigated. SBF is a hydrous solution with physiological concentrations of mineral components; its composition after [160] is summarized in table 6.2.

material	characterization	media	temperature [°C]	exposure time [weeks]
CF/PEEK	4-pt bending	dry	90	25
CF/PEEK	4-pt bending	SBF	37	25
CF/PEEK	4-pt bending	SBF	60	25
CF/PEEK	4-pt bending	SBF	90	25
CF/PEEK	4-pt bending	H ₂ O	90	12.5, 50
CF/PEEK	impact	H ₂ O	90	25
CF/PEEK	compact tension	H ₂ O	90	35
GF/PET	4-pt bending	H ₂ O	90	1, 2
GF/PET	impact	H ₂ O	90	1

Table 6.1: Characterization methods, media, temperatures and exposure times of the tested knitted CF reinforced PEEK and knitted GF reinforced PET samples.

ion conc. blood plasma [mmol/l]	ion conc. SBF [mmol/l]	chemicals used [mmol/l]	molecular weight [g/mol]	weighted-in quantity [mg]
2.5 (Ca ²⁺)	2.5 (Ca ²⁺)	2.5 (CaCl ₂)	111.0	277.5
1 (HPO ₄ ²⁻)	1 (HPO ₄ ²⁻)	1 (KH ₂ PO ₄)	100.1	96.7
142 (Na ⁺) 103 (Cl ⁻)	142 (Na ⁺) 148 (Cl ⁻)	137 (NaCl)	58.4	8006
1.5 (Mg ²⁺)	1.5 (Mg ²⁺)	1.5 (MgCl ₂ ·6H ₂ O)	203.2	304.8
5 (K ⁺)	5 (K ⁺)	3.0 (KCl)	74.6	223.7
27 (HCO ₃ ⁻)	4.2 (HCO ₃ ⁻)	4.2 (NaHCO ₃)	84.0	352.8
0.5 (SO ₄ ²⁻)	0.5 (SO ₄ ²⁻)	0.5 (Na ₂ SO ₄)	142.0	71
2.5 (Ca ²⁺)	2.5 (Ca ²⁺)	2.5 (CaCl ₂)	111.0	277.5

Table 6.2: Composition of simulated body fluid (SBF) as used in the present work. The ion concentrations of mineralogy components was similar to the concentration in human blood plasma.

All samples were fully immersed in the respective media. To prevent evaporation of the liquid during long-term exposure of the liquid the samples were stored in Pyrex™ glass dissicators. Prior to immersion all samples were dried in a vacuum oven for 5 days at 90°C and 50°C for CF/PEEK and GF/PET, respectively.

Moisture content with increasing immersion time was determined at different time steps, using an analytical scale (Chyo JL-200, Japan). Moisture content is defined as:

$$\text{moisture content [\%]} = \frac{\text{weight of immersed sample} - \text{weight of dry sample}}{\text{weight of dry sample}} \times 100\%$$

Before weighing, the samples were taken out of the dissicators, the surfaces were gently wiped off and dried for 15 minutes at room temperature.

6.2.2. Characterization

4-pt bending

Experimental setup. Using a diamond saw, samples of 25 mm width and 100 mm length were cut from the composite panels. The sample surfaces were grounded and polished to reduce border effects. To avoid data scatter caused by varying panel qualities, unexposed and exposed samples used for a specific environmental parameter set were taken from the same panels. 4-pt bending tests were performed according to ASTM D 790M [161] on a mechanical testing apparatus (Zwick 1456, Germany). The flexural properties were determined in wale direction. The elastic bending modulus was determined between 10 and 50% of the bending strength. Test parameters are summarized in table 6.3.

parameters	CF/PEEK	GF/PET
support span [mm]	72.4	60
load span [mm]	36.2	30
crosshead speed [mm/min]	5	3.5
radius of support span [mm]	5	3
radius of load span [mm]	7.5	3
average sample thickness [mm]	1.81	1.71
support span / sample thickness	40 / 1	35 / 1

Table 6.3: Experimental parameters of the 4-pt bending test, performed according to ASTM D 790 M [161].

Immediately before testing, the immersed samples were taken out of the dissicators and subjected to 4-pt bending without being dried.

Weibull statistics. In order to investigate the influence of exposure time and temperature on the scatter of 4-pt bending results, Weibull plots were generated to compare unexposed and exposed sample populations. A possible systematical change of the scatter in function of exposure parameters becomes apparent in a Weibull plot.

The Weibull strength distribution is given by equation 14 [162]

$$P = 1 - \exp \left\{ - \int_V \left(\frac{R - R_u}{R_0} \right)^m dV \right\} \quad (14)$$

where P is the probability of failure, V the volume, R the maximum tensile strength, R_u the threshold stress, R_0 the characteristic strength and m the Weibull modulus. Weibull statistics were developed to outrule the effect of sample volume on strength values; it allows the comparison of the strengths of different-sized specimen of the same material (equation 15) [162]

$$\frac{R_1}{R_2} = \left(\frac{V_{eff_2}}{V_{eff_1}} \right)^{1/m} \quad (15)$$

The Weibull modulus m characterizes the strength data scatter. A high Weibull modulus represents low data scatter. In ceramics, m is used to characterize the brittleness of a ceramic material. To calculate Weibull modulus and Weibull strength, the data was linearized by setting R_u to zero and linearizing equation 14 which lead to equation 16.

$$\ln \left(\ln \left(\frac{1}{1-P} \right) \right) = C + m \cdot \ln R \quad (16)$$

The measured strengths were sorted in an ascending order and to each strength was assigned a probability estimation of $P = (i - 0.5) / N$, where i was the i^{th} specimen and N the total number of specimens. The Weibull modulus is the slope of the least square linear fitting curve of the data in a $\ln(\ln 1 / (1 - P))$ versus $(\ln R)$ Weibull-plot and the tensile strength is the intercept, the stress for which $\ln(\ln 1 / (1 - P)) = 0$

$$R = e^{-c/m} \quad (17)$$

6.3. Results and discussion

6.3.1. Mass gain

CF/PEEK

Moisture content of knitted CF reinforced PEEK in function of the immersion time in water at 90°C is presented in figure 6.1. Different mass gain behaviors were observed in different samples.

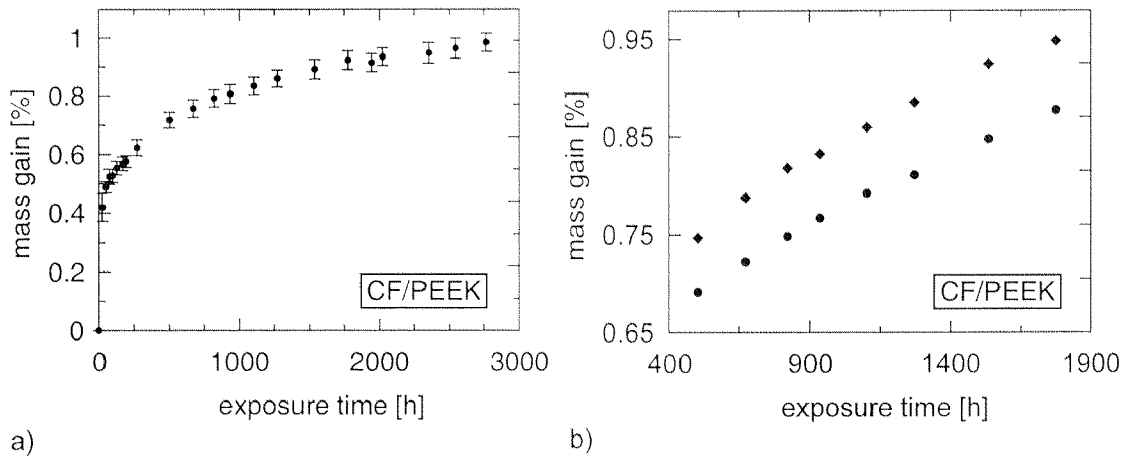


Figure 6.1: Mass gain of knitted CF reinforced PEEK (impact samples) versus exposure time in H_2O at 90°C ($n=6$). Plotting the mass gain of two randomly chosen individual samples on a smaller scale (b), it was noticed that the mass gain was substantially divergent for different samples. After 3000 hours saturation level was not reached.

The mass gain of 4-pt bending samples, after 3000 h in water at 90°C (fig. 6.1) was about 1% by weight, a value higher than ever observed in other studies (see chapter 6.1.1). Further, a saturation level was not reached after 3000 hours (≈ 17 weeks). Obviously, another water absorption process accompanied the equilibrium absorption of PEEK. In table 6.4, the maximum mass gain reached after different immersion periods is presented. Values as high as 1.68% per weight were determined in 4-pt bending samples after immersion in water at 90°C for 50 weeks.

characterization method	exposure time [weeks]	sample dimensions [mm x mm]	mass gain [%wt]
impact	17	150 x 100	0.98 ± 0.03
compact tension	25	136 x 80	1.49 ± 0.04
4-pt bending	50	100 x 25	1.68 ± 0.24

Table 6.4: Mass gain of different CF/PEEK sample series throughout exposure in H₂O at 90°C. Even though mass gain increased with time, the data could not be related to a standard physical absorption law. The higher standard deviation observed in the 4-pt bending samples series is assumed to be related with the smaller sample size.

The following reasons are assumed to be responsible for the deviating mass gain behavior:

- The sample series originate from different hot pressed panels. Considerable differences in both, mechanical properties and porosity were found in panels resulting from different manufacturing batches.
- The sample properties were also found to diverge within individual hot pressed composite panel of 300 x 300 mm². Samples from the middle of the sample showed higher mechanical properties and lower porosity than samples from the border area.
- The ratio of sample circumference to sample surface is different in impact, compact tension and 4-pt bending samples. Because of border effects, a higher ratio is supposed to lead to higher mass gain, which is coherent with table 6.4.

The porosity contents of the studied knitted CF reinforced PEEK was found to be between 1.2 and 3.3% [46]. The fact that mass gain was significantly higher than equilibrium water absorption of PEEK, and that it deviated in function of the sample series, are indications of a correlation between water absorption and porosity contents. The mass gain is supposed to be caused by physical absorption of water in the PEEK matrix and by diffusion of water into the pores. This explains the high water absorption reached and its deviating behavior depending on the sample series.

GF/PET

Significantly shorter exposure times were applied for knitted GF reinforced PET (see table 6.1). Mass gain versus exposure time to water at 90°C is plotted in figure 6.2. A saturation level of approximately 0.75% was reached. However, PET exhibits hydrolytic degradation in water at 90°C (see chapter 6.1). Therefore, saturation could also be a consequence of a competing mass loss because of matrix degradation. In preliminary studies, the weight of GF/PET samples was observed to decrease below their initial value after an exposure time of 500 hours.

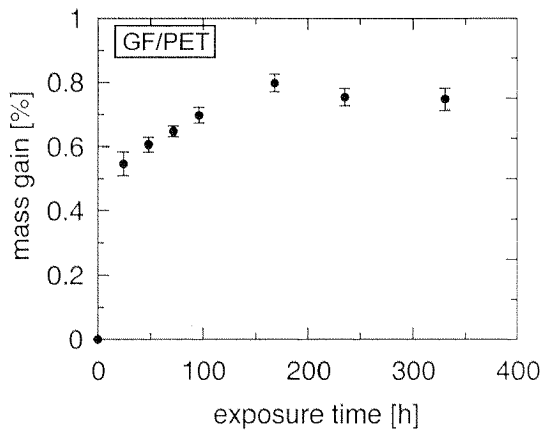


Figure 6.2:
Mass gain of knitted GF reinforced PET in function of exposure time to water at 90°C ($n = 4$). A saturation level of roughly 0.75% was reached after approximately 100 hours. The saturation level is supposed to be related with a competing mass loss process, caused by hydrolytic degradation of PET.

6.3.2. Effects on the mechanical properties of knitted CF reinforced PEEK

4-pt bending

Statistics. The 4-pt bending strength is assumed to obey a Weibull distribution (see chapter 6.2.2). The results of all unexposed samples were statistically evaluated using a Weibull plot (fig. 6.3). A Weibull modulus of $m = 15.0$ and a characteristic strength¹ of 557 MPa was determined.

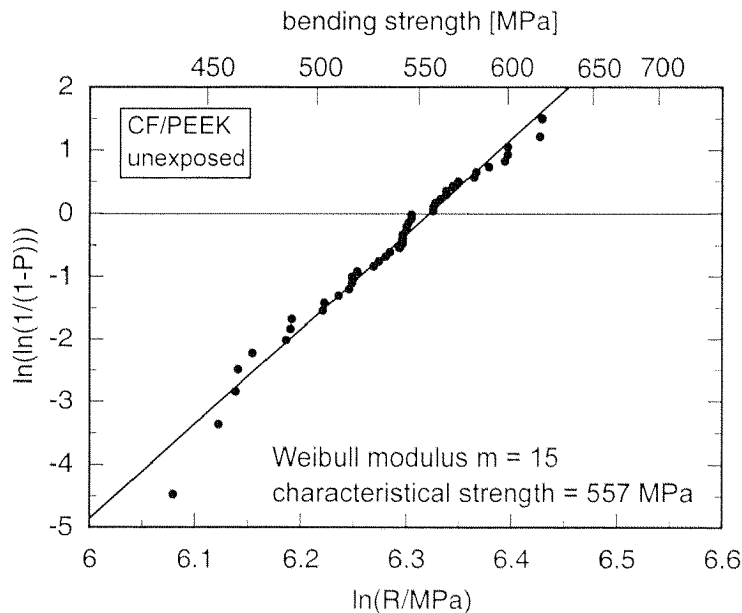


Figure 6.3:
Weibull plot of the 4-pt bending strength determined in 44 unexposed samples. A Weibull modulus m of 15 and a characteristic strength of 557 MPa (corresponding to a failure probability of 63%) were determined.

The Weibull modulus m quantifies the data scatter of the measured bending strength. High values for m corresponds to a low data scatter. In comparison, the Weibull modulus of common engineering ceramics is approximately $m = 10$. The value of $m=15$ was

1. The characteristic strength is defined as the failure probability P of $(1-1/e)$, i.e. 63% in the Weibull statistics.

determined for the bending strength of unexposed CF/PEEK samples originating from different manufacturing batches and from different locations within a composite panel. As mentioned in chapter 6.2.2, samples which were used to evaluate the effect of a specific environmental parameter were taken from the same panel in order to reduce data scatter. Therefore, the resulting Weibull moduli were higher than the one determined from all unexposed samples. Weibull statistics were exclusively performed to evaluate the influence of the exposure on the data scatter. The 4-point bending strength and E-modulus were determined using standard average and standard deviation. Therefore, Weibull plots in the following sections are given without indication of m and characteristic strength.

Influence of temperature. The main purpose of the investigation of physically aged dry samples, was to distinguish between the influence of temperature and the effect of water. Bending strength and E-modulus before and after physical aging at 90°C for 25 weeks are plotted in figure 6.4. Weibull plots are shown, because a systematical change of the data scatter as a consequence of the exposure would split the Weibull data into two groups, exhibiting different slopes of linear approximation.

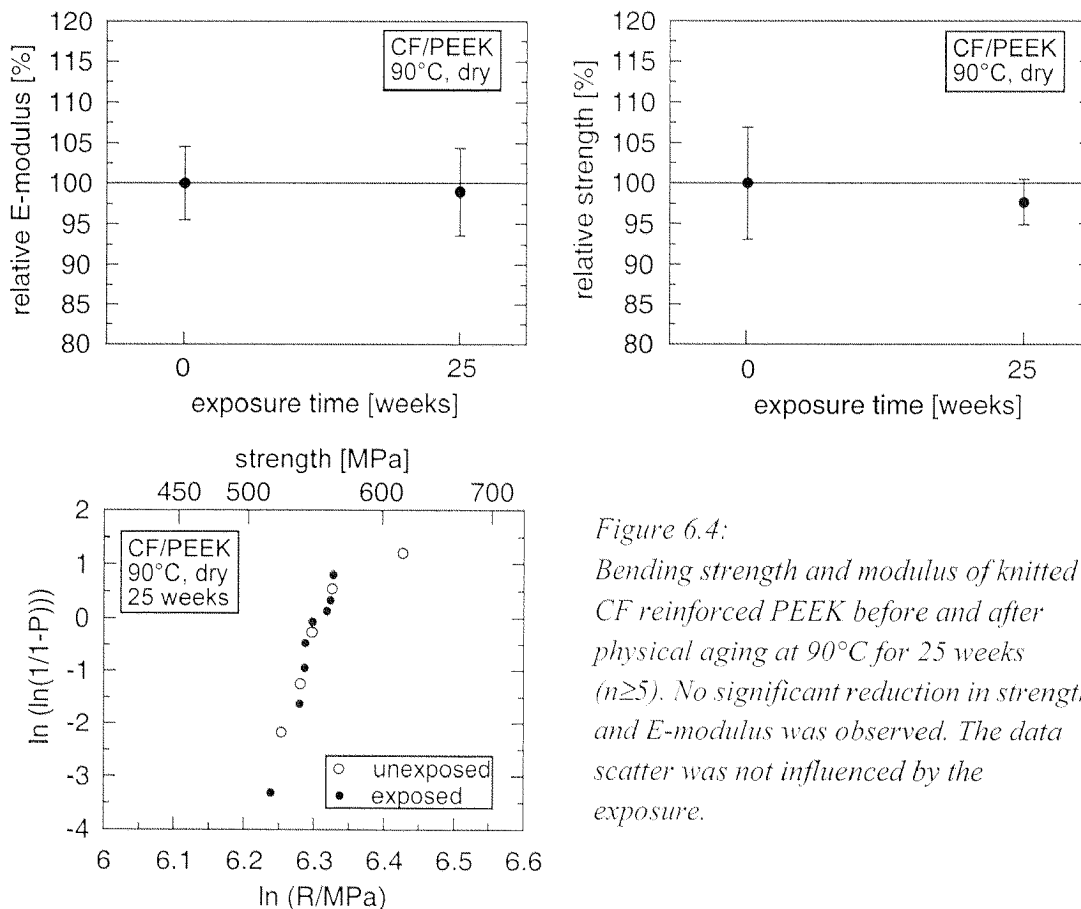


Figure 6.4: Bending strength and modulus of knitted CF reinforced PEEK before and after physical aging at 90°C for 25 weeks ($n \geq 5$). No significant reduction in strength and E-modulus was observed. The data scatter was not influenced by the exposure.

No significant decrease of the flexural properties was found. Physical aging showed no substantial effect on flexural properties of CF reinforced PEEK. Neither data scatter nor

changes in bending strength and E-modulus were found after 25 weeks of exposure to air at 90°C.

Influence of water. Bending strength and E-modulus before and after exposure in water at 90°C for 12.5 and 50 weeks are shown in figure 6.5.

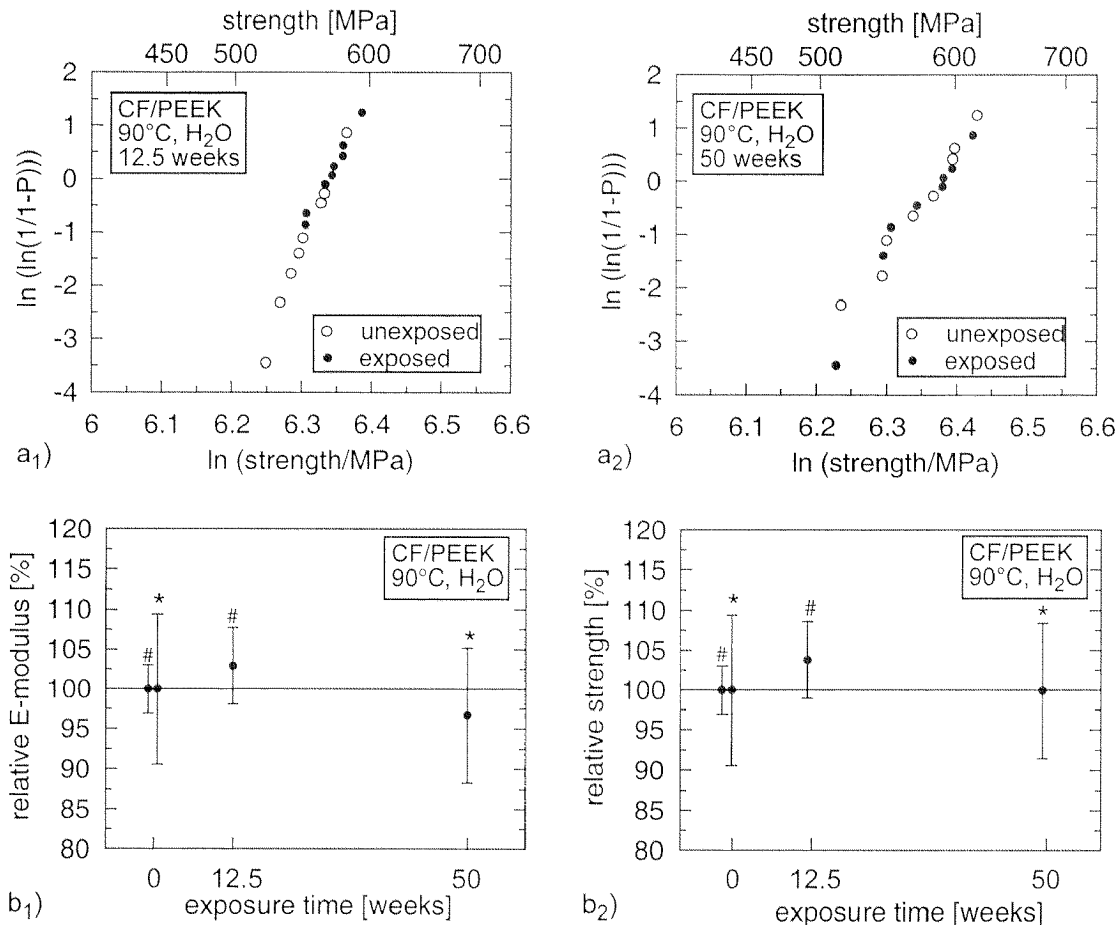


Figure 6.5: Bending strength and E-modulus of knitted CF reinforced PEEK before and after immersion in H_2O at 90°C for 12.5 and 50 weeks ($n=8$). The indices * and # refer to the respective unexposed samples. No significant decrease of E-modulus (b₁) or strength (b₂) was observed. The data scatter was not systematically influenced by the exposure (a₁₋₂).

Similar to the physical aging in air, immersion in water did not influence the bending properties of CF/PEEK knits.

Influence of SBF at different temperatures. Regarding the medical applications of CF reinforced PEEK, immersion in SBF was the most important environmental effect studied in this work. In figure 6.6, the effect of exposure to SBF on the flexural properties of knitted CF reinforced PEEK is shown.

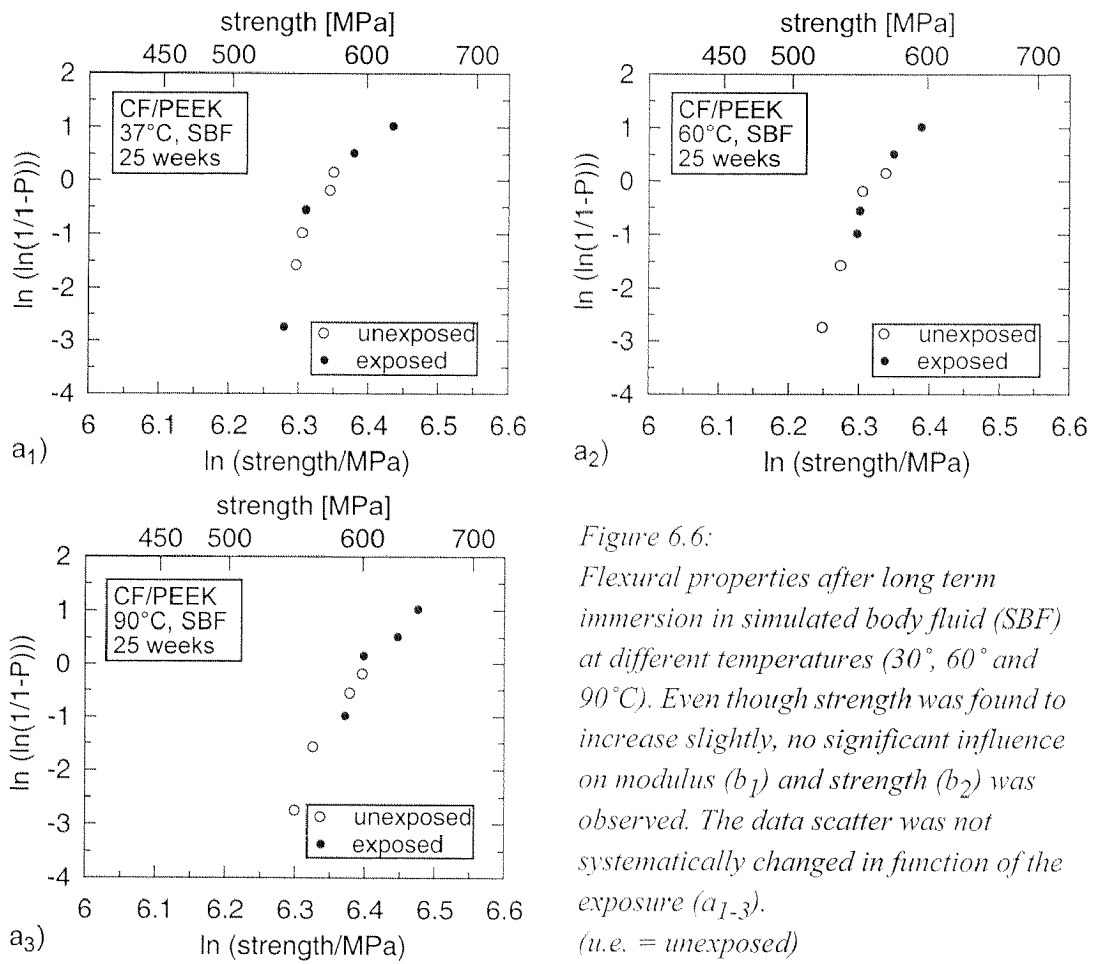


Figure 6.6:
Flexural properties after long term immersion in simulated body fluid (SBF) at different temperatures (30°, 60° and 90°C). Even though strength was found to increase slightly, no significant influence on modulus (b_1) and strength (b_2) was observed. The data scatter was not systematically changed in function of the exposure (a_{1-3}).
(u.e. = unexposed)

The results revealed no significant effects of long term immersion in SBF. At elevated temperatures, a slight increase of the strength was observed (fig. 6.6, b₂). However, the effects remained within standard deviations and therefore were considered to be insignificant.

Damage zone. Figure 6.7 shows SEM micrographs of tested 4-pt bending specimens (tensile surface). Unexposed (a) and exposed (50 weeks in H₂O at 90°C) samples (b) exhibited no detectable differences in fracture behavior. At the fracture surfaces of bundles (A), matrix adhering at the fiber surface and short fiber pull-out lengths (arrows in a₂ and b₂) were observed. This is an indication of high fiber/matrix interface adhesion.

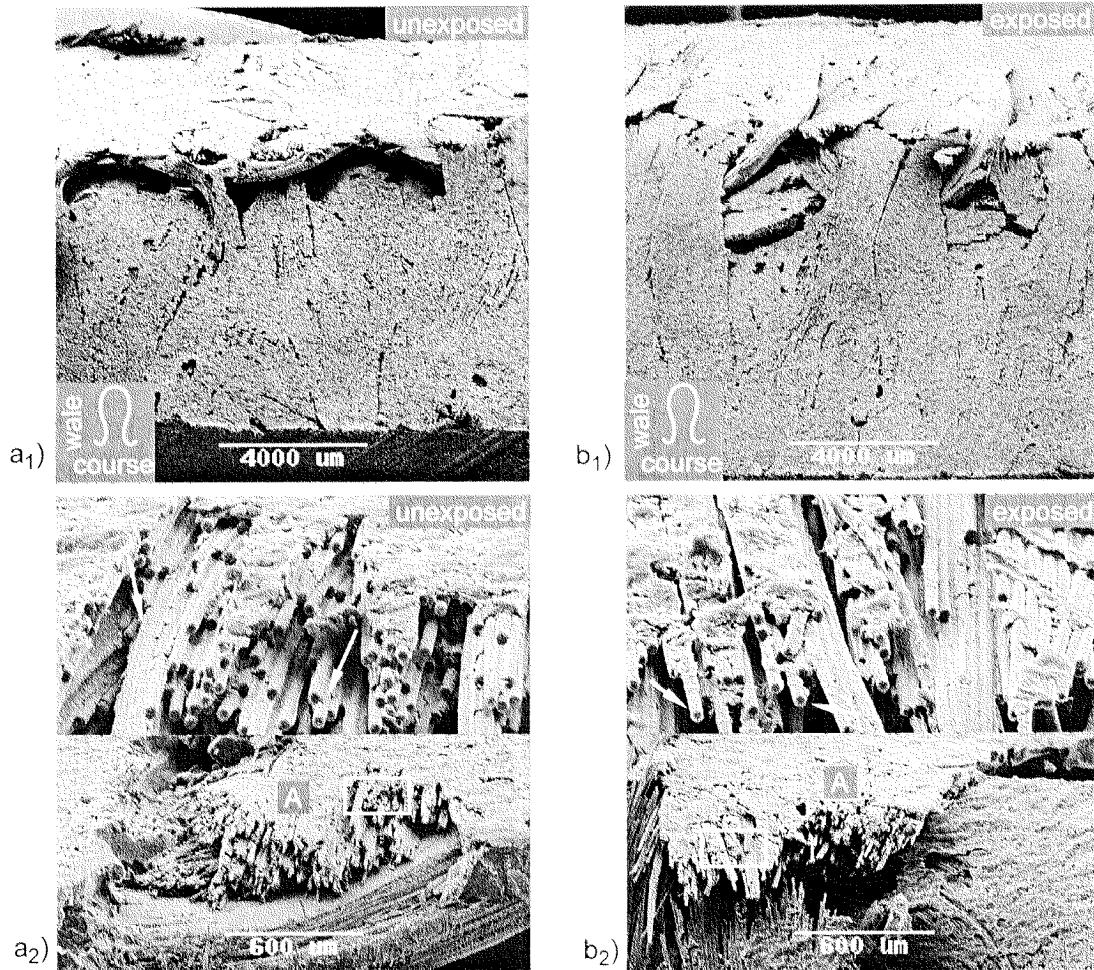


Figure 6.7: SEM investigation of tested 4-point bending samples (tension surface). After 50 weeks in H₂O at 90°C (b), no significant differences in the phenomenological fracture behavior was found. Matrix adhering at the fiber surface and short fiber pull-out lengths were observed, before and after exposure (arrows in a₂ and b₂). This is an indication of high interfacial adhesion.

Compact tension

Energy release rate G_{IC} and fracture toughness K_{IC} of knitted CF reinforced PEEK exposed to H₂O at 90°C are presented in figure 6.8. See chapters 4.3.2 and 4.3.3 for definitions of terms and discussion of the unexposed results. Table 6.5 gives an overview of all results, before and after immersion.

CF/PEEK	unexposed G_{IC} [kJ/mm ²]	exposed G_{IC} [kJ/mm ²]	unexposed K_{IC} [kJ/mm ²]	exposed K_{IC} [kJ/mm ²]
1 st significant crack growth (90°)	23 ± 9	19 ± 5	20 ± 4	18 ± 2
crack growth at F_{max} (90°)	32 ± 7	28 ± 5	24 ± 3	22 ± 2
1 st significant crack growth (0°)	54 ± 12	68 ± 6	45 ± 5	50 ± 2
crack growth at F_{max} (0°)	74 ± 15	98 ± 16	52 ± 5	61 ± 5

Table 6.5: Energy release rates G_{IC} and fracture toughness K_{IC} before and after immersion in H_2O at 90°C ($n \geq 4$). See chapter 4.3.2 for definition of 1st significant crack growth and crack growth from F_{max}

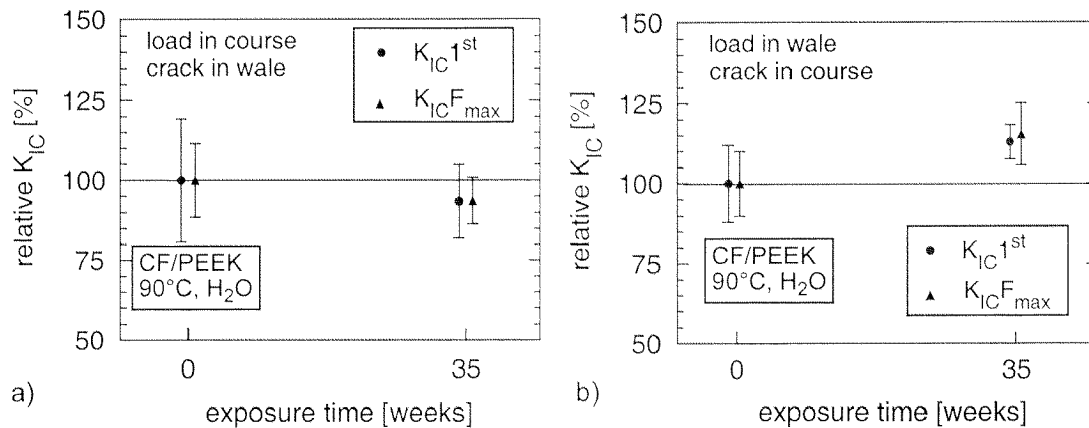


Figure 6.8: Relative changes of the fracture toughness K_{IC} before and after immersion for 35 weeks in H_2O at 90°C. Even though a slight increase in the case of the 0° samples (b.) was observed, the differences remained within standard deviation. For absolute values of K_{IC} and G_{IC} , see table 6.5.

All changes observed remained within standard deviation. While the fracture toughness slightly decreased in 90° testing (load in course, crack in wale), a tendency to higher values was observed in 0° testing (load in wale, crack in course). However, the differences were not significant.

The failure behavior in compact tension testing and the resulting damage zone and fracture surface of exposed CF/PEEK samples were similar to those of the unexposed samples. It is referred to chapter 4 for a detailed study of the observed phenomena.

Impact

Impact performance of KFRCs was studied in chapter 5. Definitions of terms and discussion of failure mechanisms are presented in chapter 5.

Perforation testing. The characteristic impact values of as received and exposed samples are summarized in table 6.6. A small amount of samples were tested successfully ($n=2$). Small differences were observed in initiation energy and propagation energy between unexposed and exposed samples. However, the influence of exposure on perforation impact behavior is considered irrelevant, due to the small amounts of successfully tested samples.

	peak force [kN/mm]	initiation energy [J/mm]	propagation energy [J/mm]	dissipated energy [J/mm]	ductility index []
6 DL (1.81 mm) unexposed	1.4, 1.4	3.5, 4.4	7.1, 6.5	10.7, 10.9	0.7, 0.6
6 DL (1.87 mm) exposed	1.3, 1.4	5.7, 5.1	4.6, 3.7	10.3, 8.9	0.5, 0.4

Table 6.6: Characteristic impact values of knitted CF reinforced PEEK, exposed and unexposed ($n=2$). All values were thickness normalized. A slight shift from propagation to initiation energy was observed as a consequence of the exposure. This led to a slightly lower ductility index. However, due to the small amount of successfully tested samples, this tendency is considered irrelevant.

The investigations of the perforation impact damage zones showed no detectable difference in macroscopical and microscopical failure behavior of unexposed and exposed samples.

Low energy impact. Results of as received and exposed samples are summarized in table 6.7.

CF/PEEK	peak force [kN/mm]	dissipated energy [J/mm]
4 DL (1.26 mm) unexposed	1.0 ± 0.1	1.4 ± 0.3
4 DL (1.28 mm) exposed	1.0 ± 0.1	1.6 ± 0.4

Table 6.7: Low energy impact response of as received and exposed knitted CF reinforced PEEK ($n = 5$ for exposed, $n = 3$ for as received). No significant differences were observed.

All values determined in low energy reflected no significant influence of hygrothermal degradation. The threshold value for damage initiation (peak force) and dissipated energy remained unchanged. Similar as in perforation impact testing, no difference in macroscopical failure behavior was observed in SEM investigations of the damage zone.

Discussion

Physical aging and hygrothermal exposure to water and SBF exhibited no significant effects on the mechanical properties of knitted CF reinforced PEEK, determined in 4-pt bending, compact tension and impact testing. In all characterization methods, failure behavior and damage zones were found to be unaffected by the exposure. However, some tendencies were observed in the numerical results of unexposed and exposed CF/PEEK. To evaluate if these trends are consistent or not, they are discussed and compared with results reported in literature.

Increasing mechanical properties could be explained by relaxation mechanisms of the PEEK matrix, as observed in [144]. However, relaxation is a consequence of temperature and therefore, occurs to the same extent during exposure at 90°C, regardless of the environment. Relaxation mechanisms could explain the slight increase of 4-pt bending strength (fig. 6.6, b) but is in contrast with the unchanged 4-pt bending strength of physically aged CF/PEEK. Reduced interface strength after exposure to physiological saline as determined in [26, 28], is oppositional to the increased 4-pt bending strength after immersion in SBF (fig. 6.6, b). A decrease of the transverse properties of unidirectional CF/PEEK, caused by immersion in water at 37°C was reported in [41]. This would be in accordance with the slightly decreasing fracture toughness determined in 90° compact tension but is in contrast with the bending strength which was found to remain unchanged after long term exposure to water at 90°C.

The observed tendencies are contradictory. Therefore, and because all changes remained within standard deviation and a 5% limit of the initial value, it is concluded that longterm exposure to SBF and water at elevated temperatures shows no effect on the mechanical properties of knitted CF reinforced PEEK.

6.3.3. Effects on the mechanical properties of knitted GF reinforced PET

4-pt bending

Because of the larger panel dimensions (700 x 500 x 1.8 mm, see chapter 2.2), all knitted GF reinforced PET samples could be taken from the same composite panel. Therefore, results of the exposed GF/PET samples can be referred to one single unexposed batch, unlike the CF/PEEK results presented in the previous chapter. Weibull statistics (chapter 6.2) were performed on the bending strength of exposed knitted GF reinforced PET (fig. 6.9). The samples were immersed in H₂O at 90°C for 1 and 2 weeks, respectively.

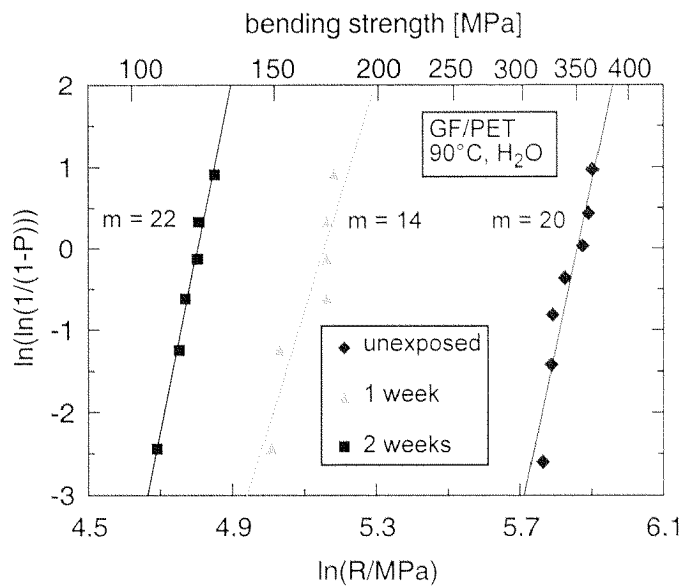


Figure 6.9:

Weibull plot of unexposed and exposed GF/PET bending samples. Significant decrease of bending strength (i.e. shift from right to left) in function of exposure time was observed. The Weibull modulus m , which quantifies the data scatter, did not change systematically. This is an indication that degradation effects occurred universally among all tested samples.

Elastic modulus and strength were calculated using standard average and deviations. The absolute values are given in table 6.8, the relative properties, as a function of the exposure time, are shown in figure 6.10.

exposure time [weeks]	bending E-modulus [GPa], [%]	bending strength [MPa], [%]
unexposed (n = 7)	21.1 ± 0.7, (100)	328 ± 8, (100)
1 week (n = 6)	19.0 ± 1.2, (87)	167 ± 13, (50)
2 weeks (n = 6)	17.8 ± 0.9, (81)	119 ± 6, (35)

Table 6.8: Bending strength and E-modulus were found to decrease significantly after exposure in H₂O at 90°C for 1 and 2 weeks, respectively. The loss of properties was more pronounced for E-modulus than for strength.

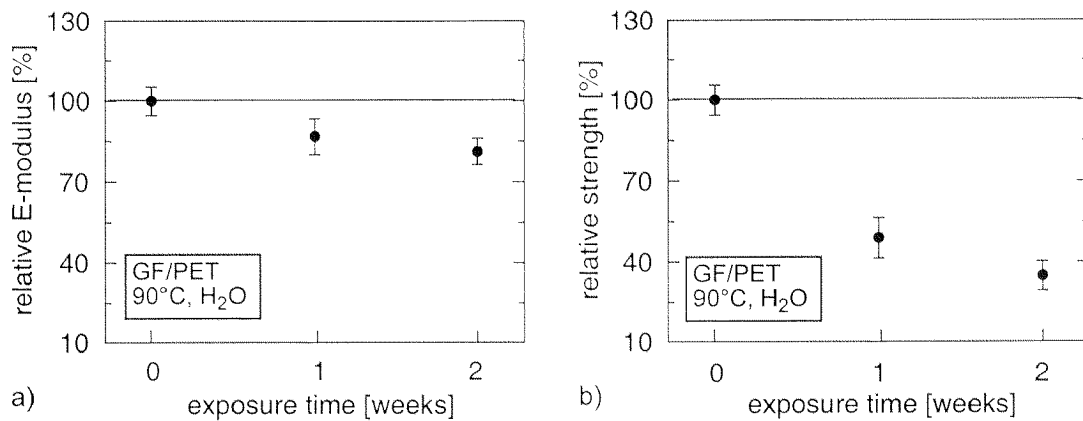


Figure 6.10: Relative bending properties of unexposed and exposed GF knitted reinforced PET (1 and 2 weeks in H_2O at $90^\circ C$, respectively). Significant decreases were found in modulus and, to a higher degree, in strength.

The flexural properties were found to be significantly reduced by environmental exposure. It is important to note that the E-modulus also decreased, although to a smaller extent than strength.

Damage zone. Differences in the microscopical failure of unexposed and exposed GF/PET fracture surfaces were studied. After bending failure, the samples were manually separated to allow investigation of the bulk of the fracture zone. Figure 6.11 shows SEM micrographs from the tension surface of unexposed (a) and exposed (b, 2 weeks, H_2O , $90^\circ C$) 4-pt bending samples. Bundles failed in tension (A), exhibited relatively short pull-out lengths in unexposed GF/PET (a_1). A high amount of fibers in exposed samples were completely released from the matrix (b_1 , B). Transverse splitting of loop heads (C) was observed in the exposed samples only (b_1). This was an indication for reduced fiber/matrix interface strength. In high magnification SEM micrograph (b_2), fiber surfaces free from matrix (E) were noticed in exposed GF/PET (b_2). Matrix fragments were still adhering to the fiber surfaces of unexposed samples (a_2 , D). Although the fibers in exposed samples (b_2) were free from matrix (E), the fiber surface and its failure behavior did not exhibit signs of fiber degradation. The influence of exposure is assumed to be limited to matrix and fiber/matrix interface degradation.

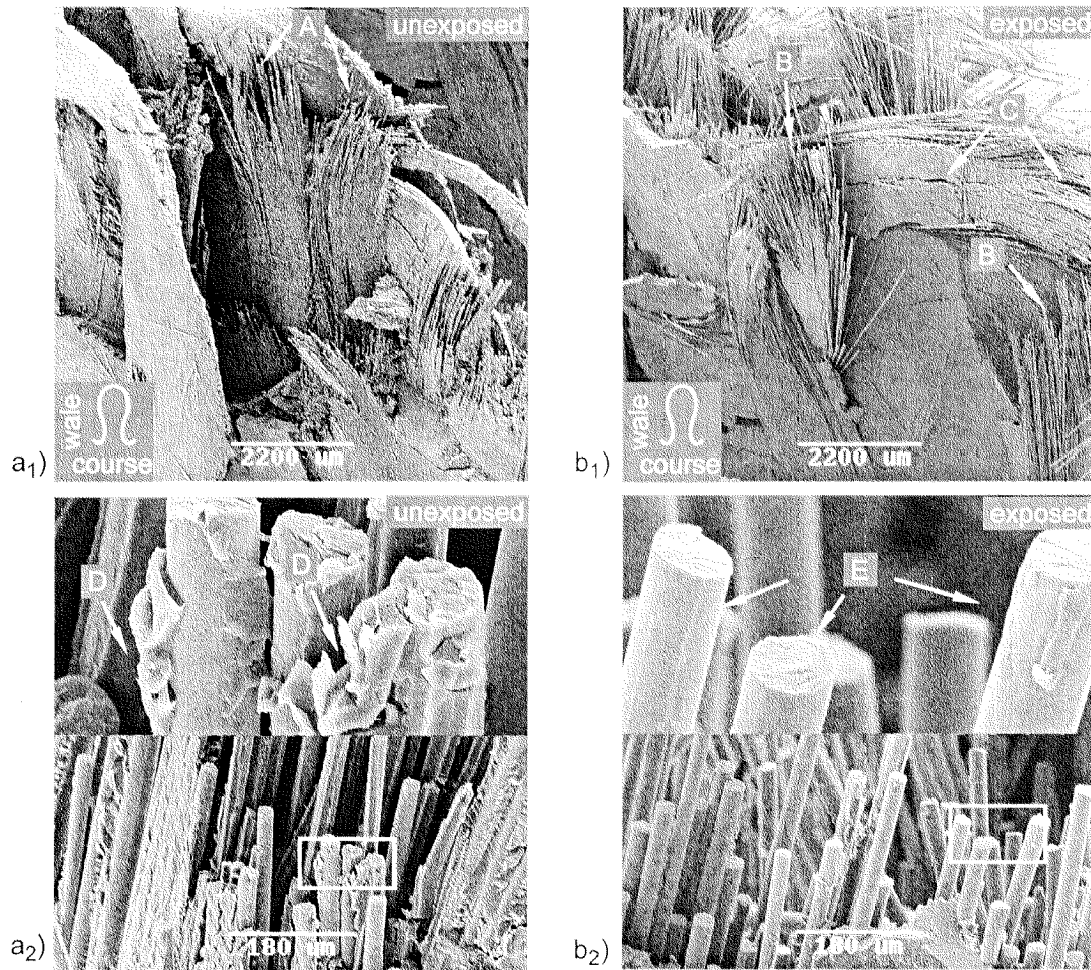


Figure 6.11: Fracture surfaces of unexposed (a) and exposed (b) 4-pt bending samples. After failure, the samples were manually separated to allow investigation of the bulk of the fracture zones. In unexposed GF/PET, short fiber pull-out lengths were observed in bundles failed in tension (A). Transverse splitting of loop heads (C) and long fiber pull-out lengths (B) were found in exposed samples (2 weeks, H_2O , $90^\circ C$), thus indicating a reduced fiber/matrix interface strength. This is coherent with the observation of fiber surfaces clean from matrix (E) in exposed GF/PET, whereas pulled-out fiber surfaces in unexposed samples exhibited more adhering matrix fragments (D).

Impact

In contrast to CF/PEEK, after only one week exposure to H₂O at 90°C significant differences were observed in the excess energy impact test results of unexposed and exposed knitted GF reinforced semicrystalline PET. Characteristical impact values are presented in table 6.9.

semicrystalline GF/PET	peak force [kN/mm]	initiation energy [J/mm]	propagation energy [J/mm]	dissipated energy [J/mm]	ductility index []
4 DL (1.76 mm) unexposed	2.2 ± 0.1	11.6 ± 1.2	7.7 ± 1.7	19.3 ± 1.5	0.4 ± 0.1
4 DL (1.68 mm) exposed	1.3 ± 0.2	9.8 ± 0.9	4.7 ± 0.7	14.4 ± 1.2	0.3 ± 0.1

Table 6.9: Thickness normalized characteristic impact values of excess energy impacted knitted GF reinforced PET, as received ($n=3$) and exposed (7 days in H₂O at 90°C, $n=4$). A significant reduction of peak force, propagation and dissipated energy resulted from the exposure.

Significant reduction was observed in peak force, propagation and dissipated energy. The respective force-time and force/energy-displacement plots are shown in figure 6.12.

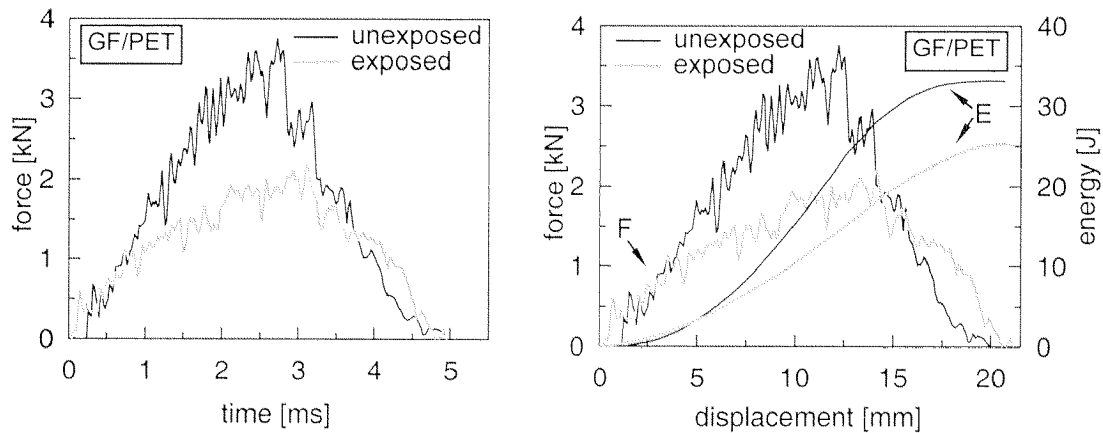


Figure 6.12: Perforation (excess energy) impact response of unexposed and exposed (1 week in H₂O at 90°C) knitted GF reinforced PET. The exposed composite revealed a substantially different impact behavior: The amount of total dissipated energy upon perforation was substantially lower in the exposed samples.

Exposed samples showed a significantly lower peak force, which was reached at higher impactor displacement compared to unexposed samples. This can be understood if con-

sidering the low matrix and fiber/matrix interface properties in exposed GF/PET samples. The stress is transferred from one fiber to the next over interface and through the matrix. With lower matrix interface properties, stress transfer is less efficient and failure occurs at lower forces. Maximum displacement upon penetration was similar in unexposed and exposed samples, because it is assumed to be defined by the knit structure, as described in chapter 5.

Damage zone. The macroscopical perforation impact damage of an unexposed (a) and an exposed (b) semicrystalline GF/PET sample are shown in figure 6.13.

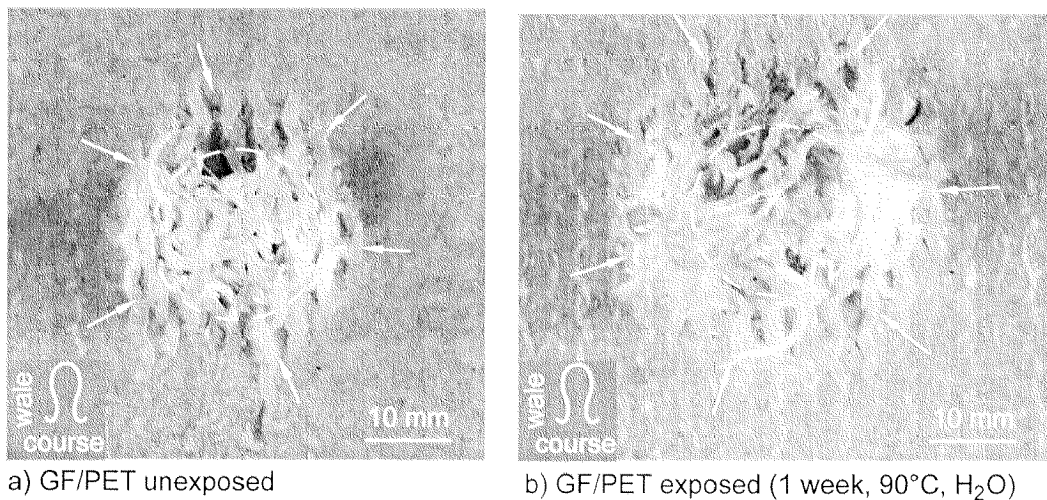


Figure 6.13: Macroscopical perforation impact damage of unexposed (a) and exposed (b) semicrystalline GF/PET. A significantly larger damage zone (arrows) resulted from perforation of the exposed sample. More fibers, released from the composite, were observed in the damage zone of the exposed samples.

A considerable larger damage zone and a higher quantity of fibers released from the matrix were observed in exposed samples. Therefore, the total fracture surface area, consisting of released fiber and released bundle surfaces, was assumed to be larger in exposed GF/PET. In contrast to the findings of chapter 5, a larger damage zone did not result in an increase of dissipated energy. It is concluded that degradation exceeded the limits in which the dissipated impact energy is positively influenced by the higher total fracture surface

Discussion

Hygrothermal exposure of knitted GF reinforced PET lead to a significant reduction of its mechanical properties, determined by 4-pt bending and perforation impact testing. The decrease was related to severe matrix and fiber/matrix interface degradation.

The fracture surfaces in exposed samples of both, 4-pt bending (fig. 6.11) and impact damage zones (fig. 6.13), exhibited significantly higher fiber pull-out lengths and

more fibers free from matrix fragments than in unexposed samples. These indications of reduced fiber/matrix interface strength were coherent with force-displacement plots (fig. 6.12) and characteristic values (table 6.9) of perforation impact experiments. Less efficient stress transfer and low matrix properties lead to lower peak forces and dissipated energy determined in exposed GF/PET.

The bending strength was reduced to 35% after two weeks of immersion in H₂O at 90°C (fig. 6.10, b). The elastic modulus of the same samples decreased to about 80% of the initial value. This result might be surprising when considering that the elastic modulus is usually not influenced by degradation. An explanation is found when considering the experimental procedure which was applied in 4-pt bending tests. As described above, hygrothermal exposure is reported to cause embrittlement [158] and to decrease yield stress and ultimate strength [159] of PET. The elastic bending modulus of GF/PET knits was determined between 10 and 50% of the bending strength (secant modulus of elasticity). Due to the embrittlement, matrix damage in the exposed samples was observed throughout the entire 4-pt bending experiment, considerably before 50% of the bending strength was reached. The determination of the elastic modulus in a stress range of damage explains its decrease compared to unexposed samples which did not exhibit damage mechanisms at stresses below 50% of their bending strength.

6.4. Conclusions

In this chapter, the effects of hygrothermal exposure on mechanical properties of knitted CF reinforced PEEK and knitted GF reinforced PET were studied. CF/PEEK knits were immersed in water and SBF at 37, 60 and 90°C for exposure times up to 50 weeks. Significantly shorter exposure times were applied for GF/PET knits, which were immersed in water at 90 °C for a maximum of 2 weeks.

While a decrease of matrix and fiber/matrix dominated, transverse properties is reported in literature [40, 41, 148], longterm immersion of CF/PEEK in H₂O and SBF at elevated temperatures showed no significant effects on 4-pt bending strength, fracture toughness and impact performances. This is mainly attributed to the excellent environmental resistance of CF/PEEK. Another contribution may be brought in by the reinforcement structure. Even though the properties of KFRCs are matrix directed [46], there is no distinctive transverse direction as in unidirectional composites. Therefore, small decreases in matrix and/or fiber/matrix interface properties may not become apparent in the macroscopical mechanical properties of KFRCs. It is concluded that knitted CF reinforced PEEK is, therefore, highly appropriate for load bearing implants.

The significant decrease of 4-point bending strength and impact performance observed in knitted fabric reinforced GF/PET is caused by a severe hygrothermal degradation of the PET matrix and of fiber/matrix interface adhesion. With respect to automotive applications, the environmental sensitivity of GF/PET has to be addressed by avoiding moisture contact. Even though the hydrolysis of PET is slower at lower temper-

atures, the temperatures at which cars are regularly exposed to are relatively high (e.g. during insolation). Considering a 50% reduction of bending properties, determined after one week in water at 90°C, it has to be expected that over the life time of a car, moisture and service temperatures would cause degradation effects strong enough to reduce the performance of GF/PET to a critical level.

Matrix and fiber/matrix degradation exhibited major effects on the failure behavior of KFRCs. In chapter 5, it was found that the lower interfacial strength of GF/PET compared to CF/PEEK showed a positive influence on the impact energy dissipation ability of GF/PET knits. In the present chapter, it was observed that a further increase of the total fracture surface, caused by a decrease of matrix and interface properties, did not lead to a further raise of dissipated energy. The degree of degradation was found to exceed the limits in which the dissipated impact energy is positively influenced by the higher total fracture surface.

Finally, matrix and interface degradation were found to affect the elastic bending modulus (secant modulus) of the studied KFRCs. This could be related with matrix damage at very low bending stresses. It is concluded, that matrix failure caused a pseudoplastic deformation behavior of the knitted fabric reinforced composite. A similar effect due to plastic deformation of the matrix was observed in knits with viscoelastic matrices, e.g. CF/PA12 [46].

7. INTERFACIAL PROPERTIES OF KFRCs INVESTIGATED BY MEANS OF THE PUSH-OUT METHOD

This chapter is divided in three parts. In the first part, an energy-based model is introduced, which was developed to interpret data measured in fiber push-out experiments on KFRCs. A tool to extract the interfacial properties from the proposed model by using automated search algorithms is described in the second part of the chapter. The final part is focussed on the effects of environmental exposure on the interfacial properties of GF/PET. The chapter concludes with a correlation between macro- and micromechanical effects, caused by hygrothermal degradation of knitted GF reinforced PET.

7.1. An energy-based analytical push-out model applied to characterize the interfacial properties of knitted glass fiber reinforced PET [96]

7.1.1. Introduction

Impact and failure behavior of weft-knitted fiber reinforced thermoplastics were observed to be strongly dependent on the interface (chapter 5). Because of the complex fiber orientation distribution in knitted textile composites, interfacial properties cannot be quantitatively investigated using macroscopic testing. Commonly used micromechanical interface characterization methods, such as pull-out, fragmentation and microdroplet (microbond) tests, require the use of a single embedded fiber model [163]. These methods, however, do not take into account the effects of the fiber architecture and neighboring fibers. Additionally, the interfacial properties of thermoplastic composites are dependent on manufacturing parameters [164-166]. Therefore, it is desirable to investigate cut-outs of real composite parts.

The microindentation method push-out was chosen to study the interfacial properties of weft-knitted fabric reinforced PET. The microindentation method was first proposed by Mandell et al [167]. Marshall et al. [168, 169] and subsequent investigators [170-176] have pushed a individually selected fiber in and through its surrounding matrix by applying load on the free end with a flat ended probe or an indenter. The push-out test has attracted much attention because it is an *in-situ* testing method conducted on real composite, thus taking into account the factors neglected by the above described, commonly used micromechanical interface characterization.

In this work, a push-out device set up in a SEM was used. Due to high resolution and depth-in-field, this experimental setup allows the on-line observation of the initial debonding, push-in and the frictional controlled push-out process of an individually selected fiber.

To extract interfacial properties from the monitored data it is necessary to make assumptions about the nature of interfacial debonding and friction mechanics along the fiber/matrix interface. In this way, an analytical model for the push-out process can be fit to recorded load displacement curves using the desired interface properties as fitting parameters [177]. To obtain an accurate fit the number of fitting parameters has to be kept as small as possible.

In the proposed energy based analytical model the involved energy is divided into debonding energy, potential energy release of the debonded fiber and frictional energy necessary to slip a fiber along the fiber/matrix interface. The new principle of the proposed model is to find the optimal additional length of debonding by keeping the total of these three components minimal. Interfacial debonding can be treated with two different approaches. A critical shear strength criterion requires the calculation for the elastic stress field along the entire fiber. The shear stress distribution during the push-out process has been estimated in previous studies which have included different types and levels of approximations, such as modeling, shear-lag analysis, and interface sliding conditions [178, 179]. The concept of interfacial surface fracture energy where the debonded surface area of the interface is proportional to the applied energy at the crack front was chosen for this work. Advantages and disadvantages of both approaches, shear stress and energy criterion were discussed by Zhou et al [176]. There it was concluded that a model based on fracture mechanics approach is physically more appealing than one based on the shear strength criterion. Interfacial friction has been addressed by a number of investigators [168, 180-182]. Friction is generally treated as a combination of thermal induced residual stresses, interfacial clamping pressure due to fiber/matrix interaction and radial stresses caused by Poisson compression of the debonded part of the fiber. The first rigorous treatment of the concept of surface fracture energy in combination with friction was given by Gao [173].

7.1.2. Materials and methods

(A) Weft-knitted glass fiber (GF) reinforced poly(ethylene-terephthalate) (PET)

Manufacturing of weft knitted GF reinforced PET is described in chapter 2. Some mechanical properties of GF and PET, relevant for the method and model described in the present chapter are listed in table 7.1.

	Young's modulus E [GPa]	Poisson coefficient ν []	linear thermal expansion coefficient α [K^{-1}]
PET	2.3	0.33	7×10^{-5}
GF	73	0.22	5×10^{-6}

Table 7.1: Some material properties of glass fiber and poly(ethylene-terephthalate), relevant for the method and model described in this chapter.

(B) Push-out experiment

The push-out device used for this study (fig. 7.1) was developed by Touchstone Research Laboratory Ltd., (USA) and was set up in the chamber of a Carl Zeiss Scanning Electron Microscope (SEM). This device makes use of the high magnification and depth-in-field of the SEM to perform push-out experiments on small diameter fiber composites while observing any failure processes occurring at the top of the free specimen surface. The loading device uses a ball screw mechanism driven by a microstepping motor with a controllable displacement rate as low as $0.06 \mu\text{m/s}$. Loading of the indenter and displacement of indenter from sample holder were digitally monitored with a load resolution $<0.001 \text{ N}$ and a displacement resolution $<0.001 \mu\text{m}$.

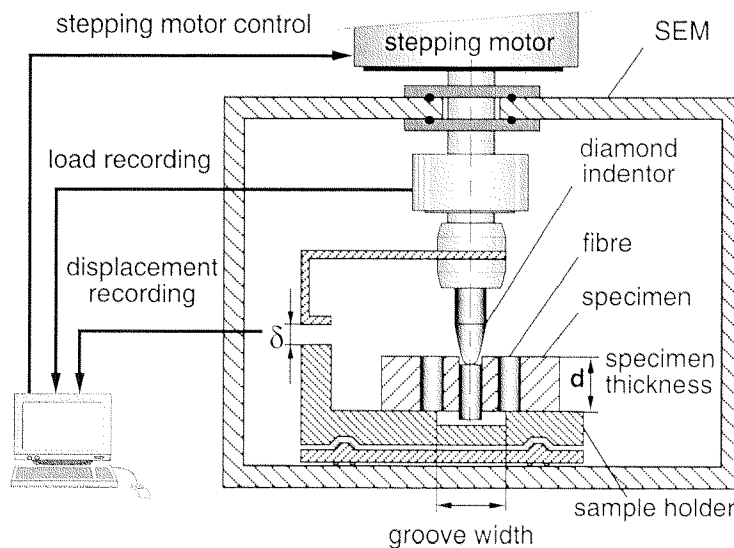


Figure 7.1: Push-out device set up in a SEM chamber, using the advantage of the high magnification and depth-in-field of the SEM. Digital data monitoring equipment is connected to the indenter. The loading device uses a ball screw mechanism driven by a microstepping motor with a controllable displacement rate as low as $0.06 \mu\text{m/s}$

An embedded hot stage allowed the characterization of interfacial properties of the composite GF/PET in function of temperature. The tests were conducted isothermally at temperatures of 23, 40 and 60°C . Specimens of the weft-knitted composite GF/PET, 200-300 μm in thickness were grounded with size 1200, 2400 and 4000 SiC grinding paper

for, respectively, 1, 1, 2 min and lapping finished for 1 min. The final specimen thickness' were: 55, 100, 103 and 104 μm . For use in the SEM the specimens were gold sputtered at 15 mA for 90 s. Specimens were mounted on sample holders with groove width of 60 and 250 μm . Fibers orientated perpendicular to the specimen surface were located and aligned with a diamond indenter, Gyger (Switzerland) inside the SEM chamber by adjusting the position of the x, y and z-axis controllable sample holder (fig. 7.2). A fiber was pushed at a displacement rate of 0.24 $\mu\text{m/s}$. Initial debonding at the top of the specimen surface was indicated by a thin charge line. Concurrently, indenter load and displacement were digitally monitored with a sample rate of 4 Hz until debonding of the interface was complete and the fiber was pushed through the matrix against friction resistance (fig. 7.2).

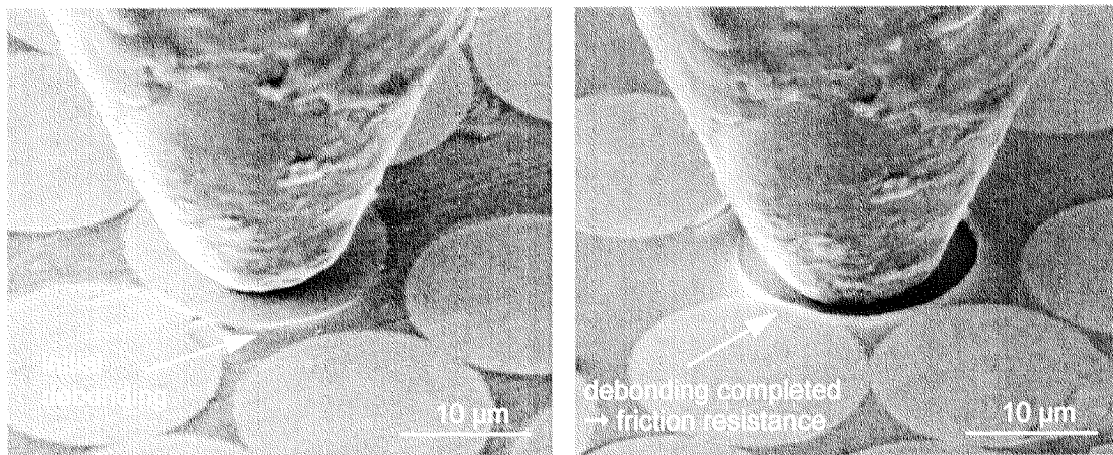


Figure 7.2: In a push-out experiment on a cut-out of GF/PET knit the thin charge line along the top of the interface indicates interface debonding at the surface at an applied force of 0.1 N (left). After complete debonding, the fiber was pushed through the matrix against friction resistance (right).

The total system compliance ($\mu\text{m/N}$) of indenter, device, specimen and sample holder was recorded for each specimen using a 50 μm diameter flat ended indenter. The compliance was then subtracted from the recorded load displacement curve (fig. 7.3). Fifty-eight push-out experiments were conducted on 5 different specimens. From the corrected load displacement curves interfacial properties were extracted using the energy based analytical model proposed in this work.

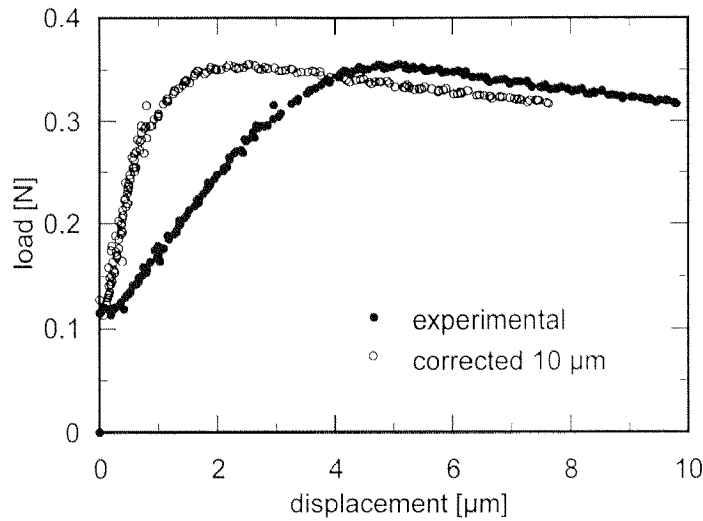


Figure 7.3:
 Experimental monitored and compliance corrected ($10 \mu\text{m}/\text{N}$) load-displacement curves of a push-out experiment conducted on a $103 \mu\text{m}$ GF/PET specimen of fiber diameter $17.7 \mu\text{m}$. Displacement rate was $0.24 \mu\text{m}/\text{sec}$ and test temperature set at 23°C .

(C) Crack initiation

In order to determine the location of crack initiation at the interface, a FEM study was performed using the software package PATRAN, MSC (USA). To include the influence of the neighboring fibers, a three cylinder model was used. This concept of a third cylinder around the loaded fiber containing the material properties of the composite was developed by Zhou [174] in his analytical treatment of the single fiber push-out. In this work, a preliminary FEM study was conducted to get a qualitative estimate of the shear stress distribution along the interface. The distinct purpose of this analysis was to answer the question of where debonding would be initiated with the specific conditions of the used GF/PET composite.

The early stage of the push-out process was simulated when the fiber is loaded and the interface is still completely bonded. This allowed an accurate study of the stress state without including the complex effects of crack progression and frictional sliding of the fiber along the debonded fiber/matrix interface. The FEM model represented a 90° section around a loaded fiber. The geometric setup, meshing and the boundary conditions are shown in figure 7.4.

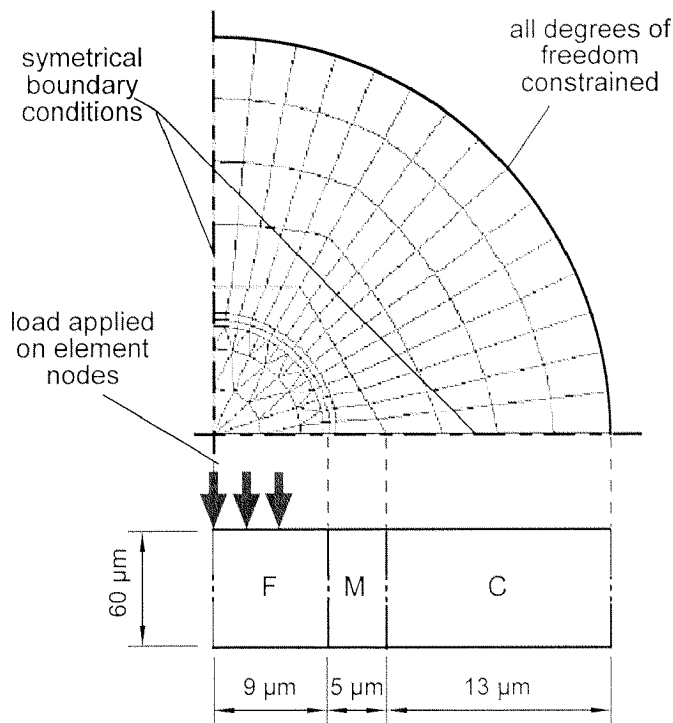


Figure 7.4:

A FEM study was conducted to get a qualitative estimate of the shear stress distribution along the interface. The scheme presents the meshing of the fiber -matrix - composite FEM model used to calculate the stress state of early stage push-out when the interface is still completely bonded. This allowed an accurate study of the stress state without including the complex effects of crack progression and frictional sliding of the fiber along the debonded fiber/matrix interface. (F = fiber; M = matrix, C = composite)

Six thousand four hundred volume elements (PATRAN type: 20 node elements) were divided into three layers with the isotropic mechanical properties of fiber, matrix and composite. Because it was found that, at a distance of $27\ \mu\text{m}$ from the fiber axis, all stresses decayed to zero, all nodes at the outer face of the composite layer could be constrained in all degrees of freedom. The mesh was refined towards the fiber/matrix interface in radial direction and biased towards the free surfaces of the specimen in axial direction, allowing accurate calculation in the regions with the highest stress gradients. Load was applied on the inner 60% of the surface nodes of the fiber, thus simulating the force indentation of the diamond indenter used in the push-out experiments. The total load on all nodes equalled to 0.1 N, which corresponds to the experimentally determined load shortly before initiation of debonding (fig. 7.2). The Young's modulus of the composite layer was varied from 2.3 to 70 GPa to simulate the entire range of the Young's modulus of pure PET up to pure GF. The FEM calculation was conducted using the linear static analysis of the PATRAN package with no thermal clamping included.

7.1.3. Energy-based analytical model

(A) Principle

In this work a new energy based model is proposed, where the push-out process is determined by minimal total energy. A cylindrical fiber of length d and radius r is initially embedded in a cylinder of composite. At every iteration step i the indenter is displaced by $\Delta\delta$. This results in progression of the crack length l_d by Δl_d (fig. 7.5 a). In the actual

push-out process it is assumed that growth of the crack length Δl_d adjusts itself in such a way that the total energy U_{tot} which the indenter supplies is minimized, whereas in the analytical model the value of Δl_d has to be determined at every iteration step i in order to minimize U_{tot} [168].

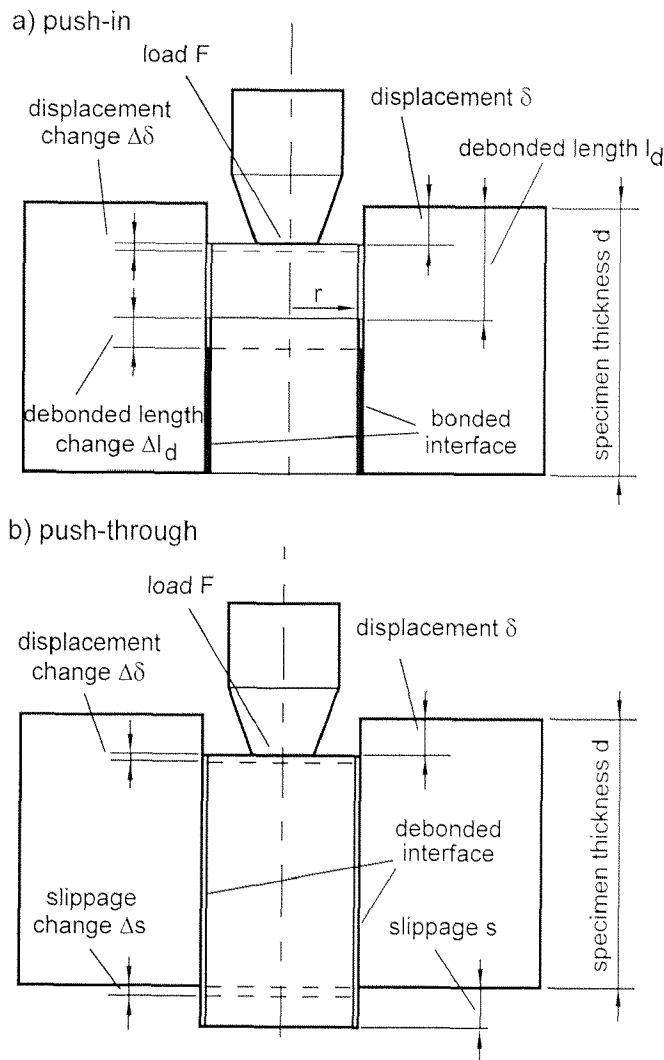


Figure 7.5: Push-in (a) and push-through (b) stage. Schematic of one iteration step in the push-out process of the proposed energy based analytical model, with partially debonded interface (a) and completely debonded interface (b).

After complete debonding of the interface the fiber has the possibility to slip out of the surrounding matrix at the back of the specimen by Δs at each iteration step i (fig. 7.5 b). Analogous to crack progression it is assumed that slippage s allows indenter displacement Δd with minimal energy U_{tot} .

$$U_{tot} \Rightarrow \left[U \left(\frac{\Delta l_{d,i}}{\Delta s_i} \right) \right] \quad (18)$$

To relate minimal energy to the applied force, energy is divided by the displacement change.

$$F_i = \frac{U_{tot,i}}{\Delta\delta} \quad (19)$$

The energy U_{tot} of the indenter consists of three components: debonding energy, potential energy change in the debonded part of the fiber and frictional energy at the debonded interface.

$$U_{tot} = U_{Debonding} + \Delta U_{potential} + U_{friction} \quad (20)$$

(B) Boundary conditions for strain and stress field

Stress decay along the axis of the debonded part of the fiber is constrained to an exponential character with the rate of decay left as a degree of freedom. The displacement change along the interface is also assumed to be exponentially distributed (21). If the external displacement is increased by $\Delta\delta$ the displacement change $\Delta\delta(z)$ of the fiber surface along the debonded interface up to the new crack length $l_d + \Delta l_d$ is:

$$\Delta\delta_i(z) = e^{c_{1,i}z} - c_{2,i} \quad (21)$$

With the two boundary conditions (BC) that the displacement change at the top of the free surface is equal to the indenter displacement change (22) and that the displacement at the new crack front is equal to zero if debonding is still incomplete and equal to the slippage Δs if debonding is completed (23),

$$\text{BC (1): } e^{c_{1,i}\delta_{ind}} - c_{2,i} = \Delta\delta_{ind} \quad (22)$$

$$\text{BC (2): } e^{c_{1,i}(l_d + \Delta l_d)} - c_{2,i} = \Delta s \quad (23)$$

the constants $c_{1,i}$ and $c_{2,i}$ are solved from the expressions:

$$(c_{2,i} + \Delta s)^{\frac{\delta_i}{l_d + \Delta l_d}} - c_{2,i} = \Delta\delta_{ind} \quad (24)$$

$$c_{1,i} = \frac{\ln(c_{2,i} + \Delta s)}{l_d + \Delta l_d} \quad (25)$$

Following (21), (24) and (25) the displacement $\delta_i(z)$ at the iteration i is then:

$$\delta_i(z) = \delta_{i-1}(z) + e^{[c_{1,i}(\delta_{i-1}(z) + z)]} - c_{2,i} \quad (26)$$

The strain in the debonded part of the fiber is expressed with:

$$\varepsilon_i(z) = c_{3,i} e^{c_{4,i}z} \quad (27)$$

The constants $c_{3,i}$ and $c_{4,i}$ are determined with the boundary conditions (28) and (30):

$$\text{BC (3): } c_{3,i} e^{c_{4,i}(\delta_{ind} + \Delta\delta_{ind})} = \frac{\partial\delta_i(\delta_i + \Delta\delta_i)}{\partial z} \quad (28)$$

using the fact that the strain is the derivative of the displacement,

$$\varepsilon_i(z) = \frac{\partial\delta_i(z)}{\partial z} \quad (29)$$

and:

$$\text{BC(4): } \int_{(\delta_{ind} + \Delta\delta_{ind})}^{(l_d + \Delta l_i)} c_{3,i} e^{c_{4,i}z} dz = \delta_{ind} + \Delta\delta_{ind} - s - \Delta s \quad (30)$$

BC(4) is based on the fact that the integrated strain over the debonded part of the fiber equals the displacement of the indenter minus the slippage of the back side of the fiber (30). The derivative of the displacement at the free end of the fiber (28) is calculated with a deviated polynomial of second degree.

$$\varepsilon_i(\delta_i + \Delta\delta_i) = -\frac{3z_{1,i} - 4z_{2,i} + z_{3,i}}{2\xi} \quad (31)$$

With (27), (28), (30) and (31) we get the expressions to compute the constants $c_{3,i}$ and $c_{4,i}$:

$$c_{4,i} = \frac{\varepsilon_i(\delta_i + \Delta\delta_i)(e^{[c_{4,i}(l_d + \Delta l_d - \delta_i - \Delta\delta_i)]} - 1)}{c_{4,i}} - \delta_i - \Delta\delta_i + s - \Delta s \quad (32)$$

$$c_{3,i} = \varepsilon_i(\delta_i + \Delta\delta_i) e^{-[c_{4,i}(\delta_i + \Delta\delta_i)]} \quad (33)$$

Hence the stress field in the debonded part of the fiber is:

$$\sigma(z) = E_{Fiber} \varepsilon(z) \quad (34)$$

Now the three terms for debonding energy, potential energy change and friction energy can be formulated.

(C) Debonding energy

Debonding is calculated by applying the concept of surface fracture energy, where the debonded interface $\Delta l_{d,i}$ is proportional to the applied energy at the crack front at iteration step i .

$$U_{deb,i} = \Gamma \cdot 2\pi r \cdot \Delta l_{d,i} \quad (35)$$

Γ , the surface fracture energy, is the first fitting parameter of the model:

$$1^{st} \text{ fitting parameter} \equiv \Gamma \left[\frac{J}{m} \right]$$

(D) Potential energy change

The change of potential energy at every iteration i was calculated for the debonded part of the fiber. Similar to (C) this energy change is primarily a function of the parameter $\Delta l_{d,i}$ (36).

$$U_{Pot,i} = \int_{\delta_i}^{l_{d,i}} \frac{1}{2} E_{Fiber} \varepsilon_i^2(z, \Delta l_{d,i}) \pi r^2 dz \quad (36)$$

$$\Delta U_{Pot,i} = U_{Pot,i} - U_{Pot,i-1} \quad (37)$$

(E) Friction energy

Friction is also influenced by $\Delta l_{d,i}$:

$$U_{Fri,i} = \int_{\delta_{ind}}^{(l_{d,i} + \Delta l_{d,i})} \frac{1}{2} [\tau_{i-1}(z) + \tau_i(z)] 2\pi r \Delta \delta_i(z) dz \quad (38)$$

with:

$$\tau_i(z) = \tau_0 + \mu [\sigma_{cl} + k \sigma_{z,i}(z, \Delta l_{d,i})] \quad (39)$$

In (39) interfacial friction is divided into three components. The friction caused by asperity interaction is accounted for with the term τ_0 . Radial stresses are divided into thermal induced clamping stresses σ_{cl} and stresses due to Poisson expansion $k \sigma_z$ where:

$$k = \frac{E_C \nu_F}{E_F(1 - \nu_C) + E_C(1 - \nu_F)} \quad (40)$$

$$E_C = \frac{E_F E_M}{E_F(1 - \nu_F) + E_M \nu_F} \quad (41)$$

$$\sigma_{cl} = k \frac{E_F}{V_F} \Delta\alpha \Delta T \quad (42)$$

ΔT is the difference between the push-out temperature and the temperature where total relaxation of the thermal induced radial stresses can be expected. The temperature for PET where no thermal induced stresses are effective was assumed to be at or slightly above the glass temperature of 70°C. The two fitting parameters for friction are the combined terms:

$$2^{nd} \text{ fitting parameter} \equiv \tau_0 + \mu \sigma_{cl} \left[\frac{N}{m^2} \right]$$

$$3^{rd} \text{ fitting parameter} \equiv \mu k$$

Inserting (35), (37) and (38) into (20) leads to the expression for the total necessary energy U_{tot} to displace the top of the fiber surface by $\Delta\delta_i$ as a function of $\Delta l_{d,i}$. By finding the $\Delta l_{d,i}$ at which U_{tot} becomes minimal the incremental growth of the crack length $\Delta l_{d,i}$ is defined.

$$\Delta l_{d,i} \Rightarrow [U_{tot,i}(\Delta l_{d,i})]_{min} \quad (43)$$

(F) Crack from back of specimen

The FEM computation suggested, that next to the free specimen surface, the back also experiences high shear stresses if the Young's modulus of the surrounding composite is low (fig. 7.6).

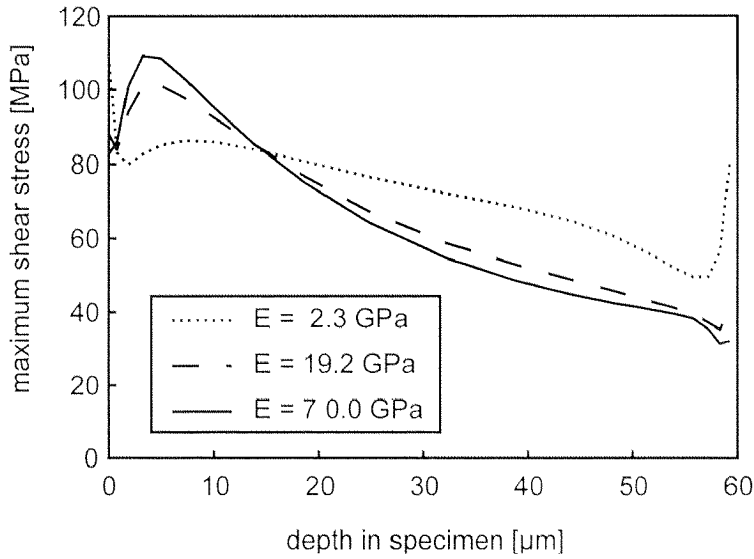


Figure 7.6:

The maximum shear stresses which are responsible for crack initiation are calculated for push-out situations with the GF/PET interface still completely bonded (specimen thickness: 60 μm , fiber diameter: 18 μm , applied load: 0.1 N). The Young's modulus is varied from 2.3 to 70 GPa, covering the range of the fiber volume content from pure PET over V_F 60% up to pure GF.

The Young's modulus is varied from 2.3 to 70 GPa, covering the range of the fiber volume content from pure PET over V_F 60% up to pure GF. Assuming a Young's Modulus corresponding to the highest possible fiber volume contents within a bundle, the maximum shear stresses occur slightly underneath the top of the free specimen surface. Therefore, it was concluded that the crack is initiated at this location. Nevertheless, relatively high shear stresses also occur at the back of the specimen, suggesting a second crack front progressing from the back along the interface. In this work, both crack fronts were taken into account. Thus, the iterations with progressive debonding are repeated up to the point where l_d reaches the critical length $l_{d,crit}$, expressed with specimen thickness d and fiber radius r , where the two crack fronts meet.

$$l_{d,crit} = d - nr \quad (44)$$

4th fitting parameter $\equiv n$ []

From this point the push-in (fig. 7.5 a) stage changes into the push-through stage (fig. 7.5 b) where the $U_{debonding}$ term of (20) becomes superfluent and minimal. U_{tot} is obtained through the optimal slippage change Δs (18) of the back end of the fiber.

7.1.4. Results and discussion

(A) Interfacial properties of weft-knitted GF/PET

From the monitored push-out data, interfacial properties were extracted using three different approaches. A first approximation of the interface shear strength was derived from formulae based on shear-lag analysis. Assuming that the hypotheses of the shear-lag analysis are correct, a possible failure criterion can be a maximum shear-stress criterion. Similar to [183], interfacial debonding shear stress (IDSS) τ_{deb} can be defined as:

$$\tau_{deb} = \frac{cF_{deb}}{2\pi r^2} \quad (45)$$

where

$$c^2 = \frac{2E_M}{E_F(1 + \nu_M) \ln\left(\frac{2\pi}{\sqrt{3}V_F}\right)} \quad (46)$$

A second approach commonly used is defining characteristically interfacial stresses σ_{deb} and τ_{fric} (table 7.2).

$$\sigma_{deb} = \frac{F_{deb}}{2\pi rd} \quad (47)$$

$$\tau_{Frict} = \frac{F_{Frict, max}}{2\pi rd} \quad (48)$$

	series 1	series 2	series 3	series 4	series 5
temperature [°C]	23	23	23	40	60
specimen thickness [μm]	55	103	103	100	104
groove width [μm]	250	60	250	250	250
number of samples	10	16	15	9	8
τ_{deb} (IDSS) [MPa]	30 ± 4	47 ± 7	46 ± 7	36 ± 3	32 ± 5
$\sigma_{deb,ini}$ [MPa]	29 ± 4	25 ± 4	24 ± 4	19 ± 2	16 ± 2
$\sigma_{deb,end}$ [MPa]	51 ± 3	59 ± 6	58 ± 6	53 ± 4	51 ± 5
τ_{fric} [MPa]	60 ± 7	64 ± 4	64 ± 6	62 ± 3	58 ± 5

Table 7.2: IDSS (Interface Debonding Shear Strength) τ_{deb} , $\sigma_{deb,ini}$, $\sigma_{deb,end}$ and τ_{fric} extracted from push-out experiments conducted on weft-knitted GF/PET.

In the third approach the interfacial properties of GF/PET were extracted using the proposed energy based analytical model.

If $\tau_0 + \mu\sigma_{cl}$ is plotted against the difference of the test temperature at which the push-out experiments were carried out and the residual stress free glass temperature T_g of PET (70°C), then the linear regression of the type:

$$\tau_0 + \mu\sigma_{cl} = 57.5 + 0.074\Delta T \quad (49)$$

defines a value for τ_0 , the friction term that is caused by asperity interaction (fig. 7.7). For the knitted GF/PET the average value for τ_0 was found to be 57.5 ± 2.5 MPa.

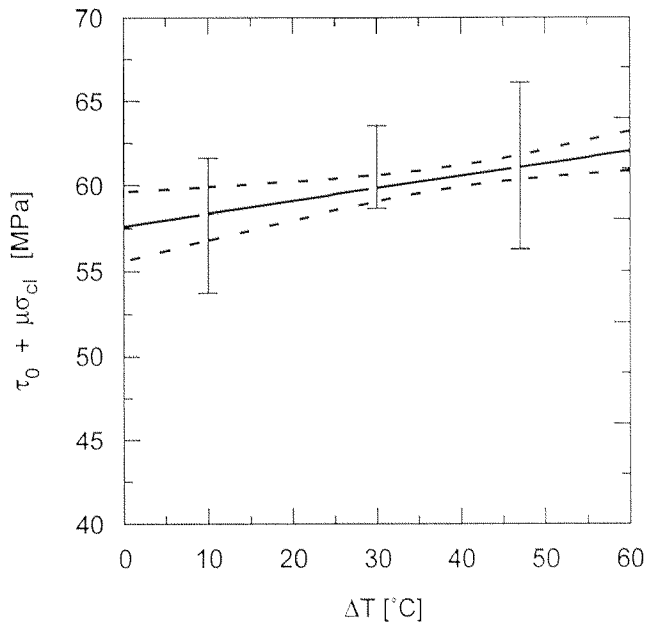


Figure 7.7:
Determination of friction stresses τ_0 , caused by asperity interactions, using the proposed energy-based model. $\tau_0 + \mu\sigma_{cl}$ is plotted versus the difference of the test temperature and the stress free glass temperature of PET. The dashed lines represent the 95% confidence limits of the linear regression through the data points. For the knitted GF/PET the average value for τ_0 was found to be 57.5 ± 2.5 MPa.

With (39) the expression for the thermal induced radial stresses (42) and the linear regression (49), the expression to determine μk is:

$$\mu k = \frac{V_F}{E_F} \cdot \frac{1}{\Delta\alpha} \quad (50)$$

where $\Delta\alpha$ is the difference between the linear expansion coefficients of fiber and matrix. Using (40) and assuming a high local fiber volume content V_F of 65% within the fiber bundle the friction coefficient μ of the GF/PET interface becomes 0.23. Note that $\Delta\alpha$ can differ considerably from its first approximation depending on the local fiber volume content around the loaded fiber. Further investigations are necessary to correlate the local $\Delta\alpha$ with the fiber volume content. The summarized results from the proposed model are listed in table 7.3.

test temperature T [°C]	surface fracture energy Γ [J/m ²]	asperity friction τ_0 [MPa]	thermal clamping σ_{cl} [MPa]	friction coefficient μ []
23	5.0 ± 0.8	57.5 ± 2.5	15.0 ± 2.5	0.23 ± 0.03
40	4.5 ± 0.8	57.5 ± 2.5	9.5 ± 2.5	0.23 ± 0.03
60	4.0 ± 0.8	57.5 ± 2.5	3.0 ± 2.5	0.23 ± 0.03

Table 7.3: Interfacial properties for weft knitted GF/PET obtained with energy based analytical model.

The surface fracture energy Γ was found to decrease with increasing test temperature. As the test temperature gets closer to the glass temperature of PET, the thermal induced radial stresses decrease.

For different material systems, crack initiation can occur at different locations of the interface. It appeared that these locations were mainly dependent upon the fiber matrix stiffness ratio. Usually, analytical models assume that debonding starts from the top of the free specimen surface [173, 176, 184]. Kerans reports that, after a certain length of debonded interface, interfacial failure can continue catastrophically [184]. This could be due to the fact that two crack fronts progressing from opposite directions meet along the interface. Variation of the composite stiffness showed that the stress decay along the completely bonded interface increased with increasing composite stiffness, i.e., with an increasing local fiber volume content V_F of the region around the loaded fiber. The calculated maximum shear stresses along the interface suggested that debonding in failure mode II is always initiated at or near the top of the free specimen surface. If the stiffness of the surrounding composite is low, a considerable rise of the maximum shear stress at the back of the specimen was predicted (fig. 7.6). Since the mixed Young's modulus of the composite increases only very slowly with an increasing fiber volume content (41), high shear stresses are to be expected at the interface near the back of the specimen. This justified the concept of a crack progressing from the back of the specimen as well.

(B) Parametric study with the energy based model

With the proposed energy based model, four different parameters of interfacial properties (Γ , $\tau_0 + \mu\sigma_{cb}$, μk , n) were extracted. To determine the relative errors when fitting the proposed model to each experimental load-displacement curve, a parametric study was conducted. While keeping three parameters constant at the value found to fit best to experimental data from GF/PET push-outs, one parameter was varied $\pm 30\%$ (fig. 7.8 a-d). The sensitivities to such changes were observed at three characteristic points of the load displacement curve. The characteristic points were defined as: Deb_{ini} (debonding is initiated), Deb_{end} (completion of debonding), and $Fric_{max}$ (maximum load during push-through). The relative error for each parameter was estimated from the change of the modeled values at these characteristic points (see table 7.4 and eq. 51). Applying results from the parametric study an optimal fitting strategy was deduced.

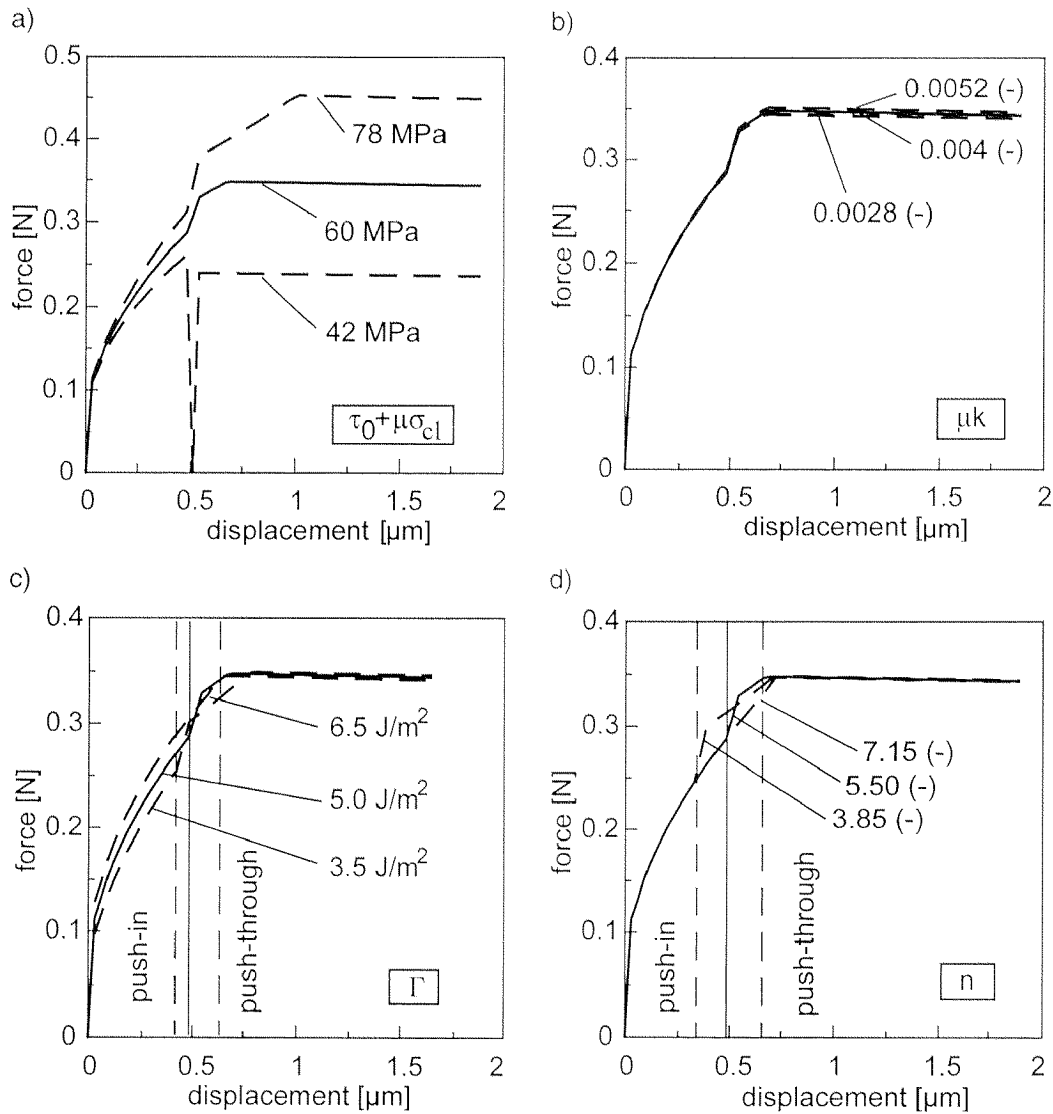


Figure 7.8: Thirty % variation of the four fitting parameters of the proposed energy based model. Friction due to asperity and residual stresses (a), effect of Poisson compression (b), surface fracture energy (c), length of crack growing from back of specimen (d).

The errors of the fitted parameters (tab. 4) were estimated with the following expression:

$$\text{relative error} = \frac{\Delta \text{ fitting parameter}}{\Delta \text{ characteristic point}} \cdot \Delta \text{ fitting accuracy} \cdot \frac{1}{\text{best value}} \quad (51)$$

with $\Delta \text{ fitting accuracy}$ no more than ± 0.01 N.

characteristic points	relative errors [%]			
	surface fracture energy Γ	friction $\tau_0 + \mu \sigma_{cl}$	crack length n	Poisson component μk
Deb_{ini}	20	125	> 200	> 200
Deb_{end}	16	12	9	175
$Fric_{max}$	160	3	> 200	100

Table 7.4: The estimated relative errors of the four fitting parameters for the three characteristic points of the load displacement curve.

(C) Fitting of model to experimental data

From the estimated errors for the four fitting parameters (table 7.4) the following fitting strategy was formulated. Since Γ was the only fitting parameter with significant influence on Deb_{ini} , it was used to fit the modeled Deb_{ini} to the experimental equivalent. The parameter $\tau_0 + \mu \sigma_{cl}$ was the only one with a considerable influence on $Fric_{max}$ and was, therefore, used for that characteristic point of the push-through stage. The parameter n was used to fit Deb_{end} because n had no influence on the other two characteristic points. For the composite system GF/PET, the influence of the Poisson effect was very small (table 7.4). The parameter μk had almost no influence on any points of the load displacement curve and, therefore, could not be accurately determined directly from the model.

(D) Specimen bending and thickness

Specimen bending was kept to a minimum for every push-out experiment conducted. If specimen bending had been too strong, mode I failure of the interface would have become predominant and the local stiffness around the loaded fiber could change along the axis due to different states of radial compression. Push-out experiments were conducted with sample holders of two different groove widths - 60 and 250 μm (table 7.5) - and with specimens of different thickness' (table 7.6) - from 55 to 104 μm - to ensure that extracted interfacial properties were neither influenced by bending effects nor by different radius/thickness ratios. For the sake of comparability, n was expressed in relation to specimen thickness, i.e. $n \cdot r/d = 1 - l_{d, krit}/d$ (see equation 44).

groove width [μm]	surface fracture energy Γ [J/m^2]	friction $\tau_0 + \mu\sigma_{cl}$ [MPa]	crack length nr/d []	Poisson component μ_k []
60	5.0 ± 0.6	61 ± 6	0.50 ± 0.06	0.004
250	5.1 ± 0.6	62 ± 6	0.51 ± 0.06	0.004

Table 7.5: Results for the four fitting parameters of experiments conducted on sample holders with two different groove width's (specimen thickness: 103 μm , push-out temperature: 23°C)

specimen thickness [μm]	surface fracture energy Γ [J/m^2]	friction $\tau_0 + \mu\sigma_{cl}$ [MPa]	crack length nr/d []	Poisson component μ_k []
55	5 ± 0.4	60 ± 7	0.71 ± 0.05	0.004
100	5.5 ± 0.8	65 ± 7	0.47 ± 0.04	0.004
103	5 ± 0.8	62 ± 5	0.47 ± 0.09	0.004

Table 7.6: Results for the four fitting parameters of experiments conducted on specimen with different thicknesses (groove width: 250 μm , push-out temperature: 23°C)

Except for n , which is not a parameter for an actual interfacial property but more a parameter reacting to different boundary conditions, none of the fitting parameters were influenced significantly by either the groove width or the specimen thickness.

(E) Comparison with existing analytical models [173, 176, 184]

The major difference of the proposed model to approaches of other authors is the concept of minimized total energy at the free fiber end. The total energy is treated as a function of change of crack length for a given crosshead displacement of the indenter. The progression of the crack front is determined by the minimum of that function. The advantage of this concept is that it is not dependent on a single stress or strain value right at the crack front, but integrates all stresses involved at an iteration point i to find the new position of the crack front for iteration point $i+1$. Because of this integration over the complete part of the debonded fiber the concept is less vulnerable to small errors of approximations at specific points.

The proposed model is avoiding the assumption made in previous approaches [173, 176, 184] that axial stress decay along the fiber is proportional to shear stress transfer through the interface, by using boundary conditions for the strain and stress field that are defined only by geometrical conditions. The assumption of shear stress proportional axial stress decay leads to an exponential stress distribution along the interface with stress decay exactly determined by shear stress transfer. In the approaches by [173, 176,

184], expressions are derived for an equilibrium of forces at the front of the progressing crack, which is sensitive to the discussed decay. From there the applied load at the free end of the fiber is recovered using various levels of approximations concerning the stress fields in the matrices surrounding the loaded fibers.

A new feature of the proposed model is the coverage of the transient phase of the push-out process. The transient phase starts at the border between push-in and push-through (fig. 7.9), at which the just completely debonded fiber is pushed into a steady purely friction controlled phase. The characteristic of this part of the load displacement curve can range from a simple load drop to complete jamming of the push-out process, where it takes less energy to increase the strain of the fiber than to let it slip along the debonded interface against pure friction. Because the transient phase is sensitive to changes of the length of the crack from the back of the specimen (fig. 7.8d) it helps to make an accurate fit to experimental data (fig. 7.9).

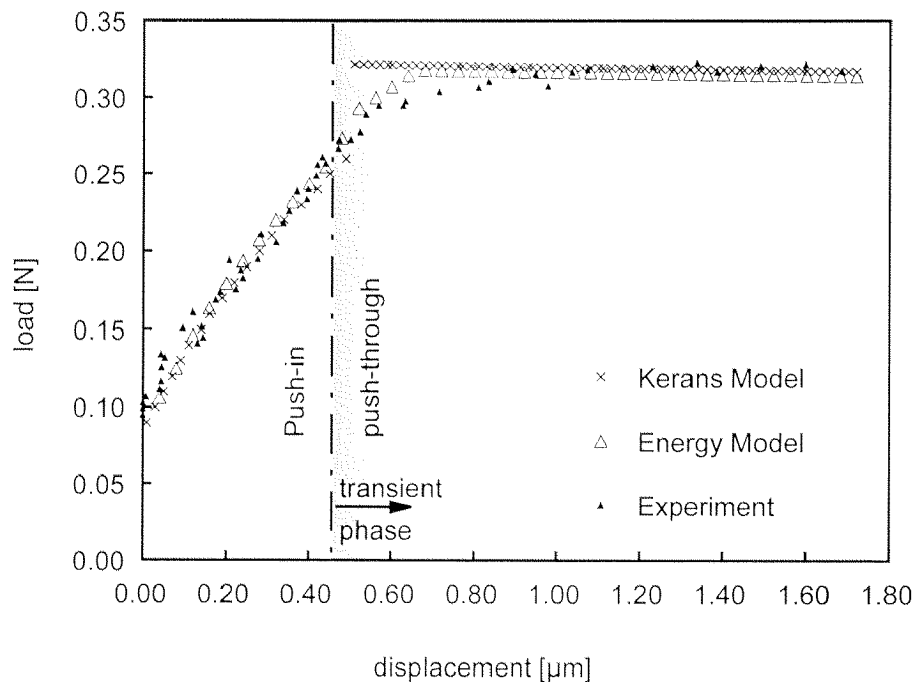


Figure 7.9: Kerans model and the proposed energy based model were fitted to an experimental load displacement curve of a push-out experiment on a GF/PET specimen (specimen thickness: 100 μm , fiber diameter: 17.7 μm , test temperature: 23°C). Particularly at the transient phase, at which the just completely debonded fiber is pushed into a steady purely friction controlled stage, the presented models gives an accurate, continuous representation of the push-out process.

Potential energy is stored in the debonded part as well as in the bonded part of the loaded fiber and in the matrix region around the interface. In this work it was found, that for

GF/PET the change of the stored energy in the debonded part of the fiber has a predominant influence on the load displacement curve. Parametric studies were carried out where more than 30% of the total potential energy was stored in the bonded part of the fiber and in the matrix region around the interface. The effect on the modeled load displacement curve was only very little, which allowed to calculate the potential energy change for the debonded part of the fiber only, using the above derived expression for the strain field (27).

The proposed energy based model was compared with the approach suggested by Kerans [184]. His model was felt to be representative for other models (e.g. [173, 176]) too, since their analysis have similar starting points. Both, Kerans' model and the proposed energy based model were fitted to an experimental load displacement curve of a push-out experiment on a GF/PET specimen (specimen thickness: 100 μm , fiber diameter: 17.7 μm). Both models correlated well with the experimental data (fig. 7.9) suggesting slightly different interfacial properties, however. The proposed model corresponds well with the experiment during all the three push-out stages while overestimating the load in the transient phase slightly. In the push-in phase, the best fit with the Kerans model remains slightly below the experimental data, neglects the transient phase and, in the steady push-through phase, rejoins the experimental curve (fig. 7.9).

It is concluded that the proposed energy based model gives an accurate, continuous representation of the push-out process while using the new principle of minimal energy which is independent of specific stress values right at the crack front.

7.1.5. Conclusions

Push-out test have been carried out with thin polished cut outs of the weft-knitted GF reinforced PET. The system compliance was measured and the experimental load displacement data could be corrected. This enabled a thorough interpretation of a large data set. In order to extract interfacial properties independent of testing conditions such as groove width and specimen thickness, an energy based analytical model is proposed. The model was independent of a solution for the stress field in the bonded part of the fiber and no assumptions about the nature of stress transfer from fiber to matrix through the interface were necessary. The concept of surface fracture energy was used to determine interfacial crack progression. Friction was treated including the effects of thermal induced residual stresses, asperity interaction between fiber and matrix and additional radial stresses caused by Poisson compression. A FEM study suggested that, while the location of interfacial failure initiation is near or at the top of the free specimen surface, a second crack can progress concurrently along the interface from the back of the sample. This effect was included in the model and was found to have considerable influence on the modeled load displacement curve. Looking at the specific influences of the model parameters, a strategy was derived to extract interfacial properties from experimental data with maximal accuracy. At room temperature, the following interfacial properties for GF/PET were found: $5.0 \pm 0.8 \text{ J/m}^2$ for surface fracture energy Γ , $57.5 \pm 2.5 \text{ MPa}$ for

asperity friction τ_0 , 15.0 ± 2.5 MPa for thermal clamping stress σ_{cl} and 0.23 ± 0.03 for the friction coefficient μ . Friction properties had a relatively large standard deviation, higher than could be expected from the conducted parametric study. It is suspected that neighboring fibers have an important influence on the local Young's modulus and the local thermal expansion coefficient, thus changing the effects of Poisson compression and thermal induced radial stresses. Further investigations are necessary to correlate the mechanical properties of the region surrounding the loaded fiber with the local fiber volume content. It is suggested that the proposed energy based analytical model, in this work applied on weft-knitted GF reinforced PET, is a suitable tool to extract interfacial properties from push-out experiments.

7.2. Push-out analyzer

7.2.1. Introduction

An energy-based analytical push-out model was described and discussed in the previous chapter. In order to apply the proposed model and to compare it with Kerans' approach [184] the models have to be fitted to the measured data. In this chapter, the "push-out analyzer" is presented, an automated tool that was developed for the following purposes:

- Analyzing of raw push-out data, i.e. performing compliance correction and determination of debonding start.
- Determination of interfacial properties by fitting either Luethi's [96] or Kerans' model [184] to experimental push-out data.
- Applying automated search algorithms in order to avoid variation in results caused by manual fitting.
- Offering a platform-independent program, accessible on the internet and written in java programming language, therefore executable on all operating systems supporting java.

An overview of the program and its three interactive windows is given below. The program can be accessed and operated on the internet: <http://www.biocomp.mat.ethz.ch>

7.2.2. Interactive window I: Data

The experimental push-out data is pasted into the first interactive window (fig. 7.10). The respective load displacement curve is displayed after assigning load and displacement columns. Test parameter (specimen thickness, fiber diameter) and material properties (moduli, Poisson ratio) have to be entered to accomplish this first step.

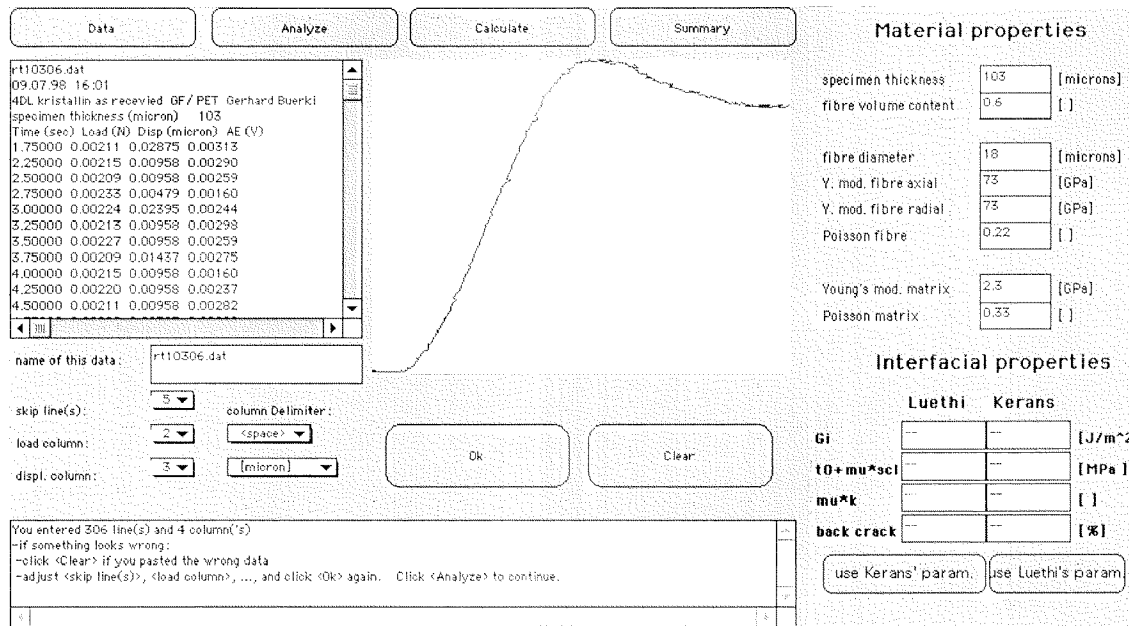


Figure 7.10: First interactive window of the push-out analyzer. In this step, experimental data and material properties are entered. The measured load-displacement curve is displayed after assigning load and displacement columns.

7.2.3. Interactive window II: Analyze

In this part of the program, the following steps are performed (see figure 7.11):

- Determination of debonding start (Deb_{ini} , see table 7.4).
- Two sections of the experimental load-displacement curve are defined. The section before the debonding start is used to determine specimen compliance, the following section is the part where the modeled load-displacement curve is fitted to.
- The actual compliance is calculated and the experimental load-displacement curve is corrected in order to make it compatible with Luethi- and Kerans model, which do not consider specimen compliance.

Initial debonding is found by calculating the first derivative of the load displacement curve. The derivative is increasing up to initial debonding where the additional relative displacement between fiber and matrix leads to a decrease of the derivative. Therefore, maximum slope of the load displacement curve (figure 7.11, A) defines debonding start. In practice it was found that calculated and experimentally observed Deb_{ini} (see figure 7.2) correlated well.

Up to debonding start, load-displacement data are used to calculate specimen compliance. The program offers the option to perform a linear or a parabolic fit (fig. 7.11, B). In most cases, displacement up to debonding was found to be a parabolic function of the applied load. The left border of the section, where compliance is determined (see

figure 7.11), is adapted to the individual push-out experiments in order to cover a representative part of the load-displacement data before debonding start.

The section after Deb_{ini} is used to extract interfacial properties. Kerans and Luethi's model are fitted to the experimental values of this section after compliance correction (see figure 7.12).

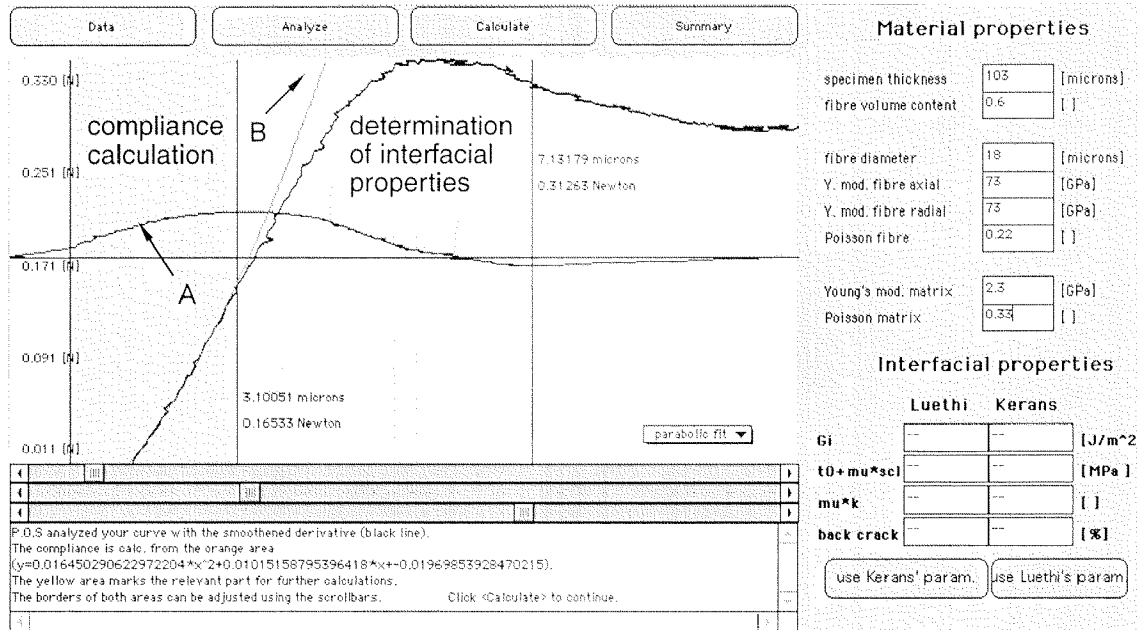


Figure 7.11: Two sections are defined in this step: Up to debonding start (deb_{ini}), load-displacement data is used to calculate specimen compliance. The models (Kerans' or Luethi's) are fitted to the compliance corrected experimental values after Deb_{ini} (fig. 7.12) in the second section. A: first derivative of the load-displacement curve. B: linear or parabolic fit of the specimen compliance.

7.2.4. Interactive window III: Calculate

This is the main part of the program. The Luethi and Kerans model are fitted to the compliance corrected experimental data by applying a direct multidimensional search algorithm (fig. 7.12). The actual fitting is performed by adjusting the free interfacial parameters Γ (page 107), $t_0 + \mu \sigma_{c1}$ (page 108), μk (page 108) and n (page 109) in order to find the best possible fit between modeled and experimental data. As a measure for the quality of the fit, a nondimensional residuum was defined. Load and displacement were normalized with maximum force and displacement. For each modeled point of the curve the next closest point of the experimental curve was found. The nondimensional distance between these two points multiplied with the distance between the modeled point and its proceeding neighbor became the partial residuum. The sum of the partial residuum for each modeled point was defined as the total residuum. To minimize the total residuum, the Powell method [185] was chosen. It is an efficient method for finding the minimum of a function of n variables. Being a direct method, it has the major advantage that no

gradient of the total residuum needs to be computed. The algorithm requires $n+1$ main- and $n+1$ subiterations. Each iteration was performed 5 times. The search algorithm along a single axis of the parametric space was done applying the Fibonacci (golden mean) method 11 times per iteration. In total, a model is executed 275 times to accomplish an entire fit. In the interactive window the residuum reached after fitting the models to experimental data is indicated (fig. 7.12). The automated search algorithm should be repeated until the residuum cannot be further reduced by additional runs.

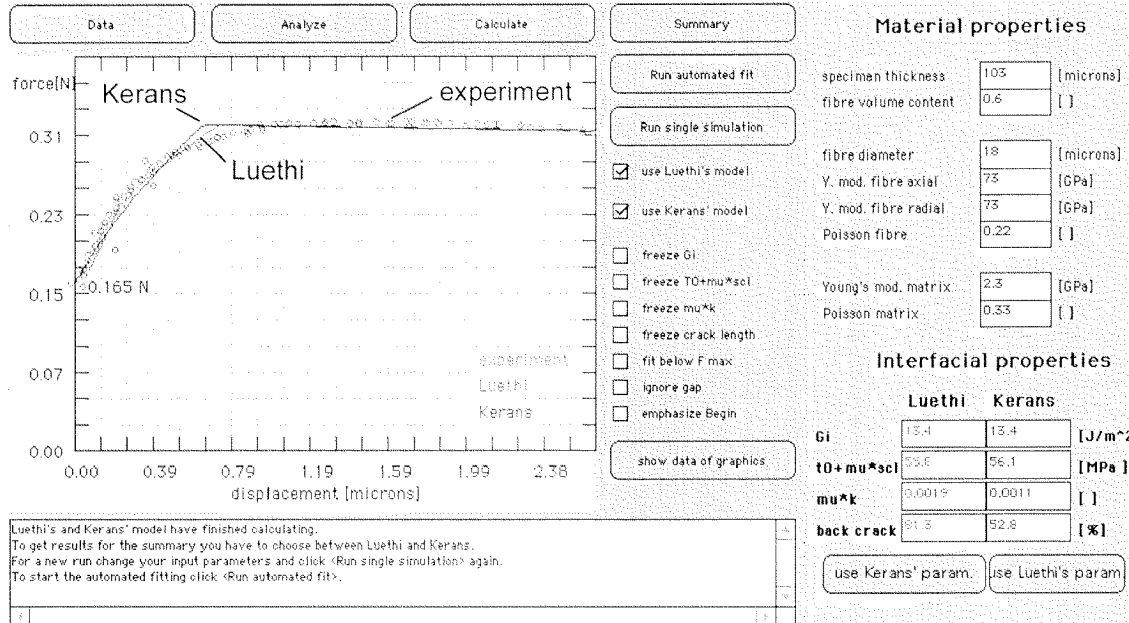


Figure 7.12: The main part of the program is to fit Luethi's and Kerans model to experimental data. The total residuum, i.e. the parameter describing deviations between models and experimental data, is minimized by applying a multidimensional search algorithm after Powell [185].

The automated fitting process can be influenced by seven different options. The first four options individually freeze the free parameters, i.e. block their degree of freedom. The other three options concern weighting of the partial residuum. Depending on the type of push-out experiment, it was found that total residuum can be further reduced by choosing one or more of the following options:

- fit below F_{max} : Modeled points above maximum experimental load are penalized by multiplying their partial residuum with factor 5.
- ignore gap: The largest displacement gap of the experimental load-displacement curve is ignored in the fitting process. This option is of advantage when investigating brittle materials with considerable load drops.
- emphasize begin: The first 30 points of the modeled curve are weighted 20 times. This option helps to reduce the total residuum if the major part of the analyzed experimental data consists of frictional sliding.

These options can be used to simplify the fitting process. In some cases, the automated search algorithm remains stuck in local minima. Freezing parameters or modifying weighting of partial residuum can help to approach the absolute minimum of the total residuum faster. However, before running the final fit, all options should be deselected in order to assure unbiased fitting.

7.2.5. Conclusions

The push-out analyzer developed in this work simplifies the application of either Luethi's or Keran's energy based pushed out model considerably. An operator-independent, automated search algorithm enables fast and systematic fitting. It further allows a direct comparison of results reached with Kerans' and Luethi's approach. Finally, the use of a platform independent from programming language and publication on the internet allows easy access and use of the push-out analyzer from anywhere using a standard internet browser.

7.3. Effects of environmental exposure on the interfacial properties of knitted GF reinforced PET

7.3.1. Introduction

In the previous chapters, an energy-based model and a computer program to evaluate push-out experiments were presented. Some experimental results were discussed, but the emphasis was kept on the concept. This chapter is focussed on experimental results, more specifically on the effects of environmental exposure on knitted GF reinforced PET. The conclusions drawn from the previous two chapters were taken into account. The push-out analyzer was used to determine the interfacial properties presented in this chapter.

7.3.2. Materials and methods

For comparability reasons, macroscopic (4-pt bending) and microscopic (push-out) testing were performed on the same samples. Exposed push-out samples were taken from intact areas of tested 4-pt bending specimens. Materials and processing details of the 4-pt bending samples are given in chapter 2, environmental conditions and experimental setup are described in chapter 6.2.

The samples were immersed in H₂O at 90°C for 7 and 14 days, respectively. Mass gain was measured in function of the exposure time (see figure 6.2). After exposure, the 4-pt bending test was performed as described in chapter 6. Push-out samples were cut from the tested specimens by diamond saw, at least 5 mm away from borders in order to

avoid side effects. Samples were grounded and stored in air at room temperature until push-out testing.

Push-out experiments were performed similarly to chapter 7.1.2 with the exception of two parameters: sample rate was increased to 8 Hz (instead of 4 Hz) and indendator speed was slightly reduced to 0.19 $\mu\text{m/s}$ (instead of 0.24 $\mu\text{m/s}$). In addition, push-back experiments with similar experimental parameters were carried out by turning the samples and loading the pushed out fibers from the back of the specimen. This was done to control the validity of the push-out experiments and to acquire a second value for fiber friction. Two indentors with different dimensions were used (see table 7.7). The advantage of the indentor with the more acute angle of center was that fibers could be pushed further through the composite. An overview of a push-out sample from top and from back is given in figure 7.13.

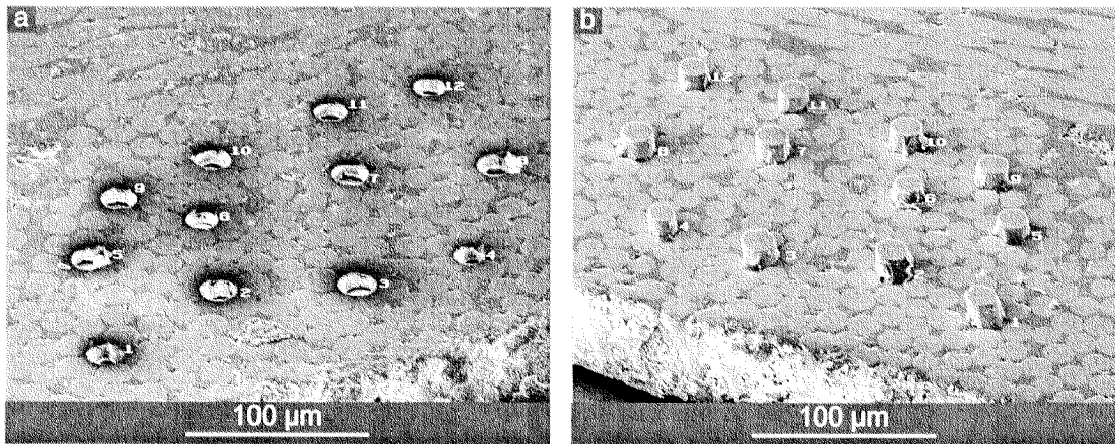


Figure 7.13: View on top (a) and back side (b) of a knitted GF reinforced PET push-out sample. All pushed fibers in this image were pushed out within the same fiber bundle. Push-back experiments were performed to obtain a second value for fiber friction and to control the validity of push-out experiments.

Sample thicknesses, number of pushed-out and pushed-back fibers are summarized in table 7.7. Push-out tests were considered invalid when fiber breakage and/or damage of the surrounding composite occurred.

Exposure time [days]	indenter: angle of center [°]/ diameter [μm]	specimen thickness [μm]	number of fibers pushed out	number of fibers pushed back	number of valid experiments
unexposed	60 / 7.1	85	18	16	11
unexposed	45 / 6.0	68	24	21	14
7	45 / 6.0	180	22	12	12
14	45 / 6.0	195	17	14	13

Table 7.7: Sample and experimental parameters of push-out experiments on unexposed and environmentally exposed knitted GF reinforced PET. Tests involving broken fibers and/or damage of the surrounding composite were considered invalid and therefore were not evaluated.

7.3.3. Results

Load displacement curves

Significant differences in load-displacement behavior of unexposed and exposed GF/PET were found. After reaching maximum force, a distinctive load drop followed by a steady friction level was observed in push-out tests with exposed samples. Two representative load-displacement curves of unexposed and exposed GF/PET are presented in figure 7.14. In both, unexposed and exposed samples, debonding start ($F_{deb,ini}$) occurred between 1.5 and 2 N, whereas debonding was completed at significant lower load levels ($F_{deb,end}$) in exposed samples.

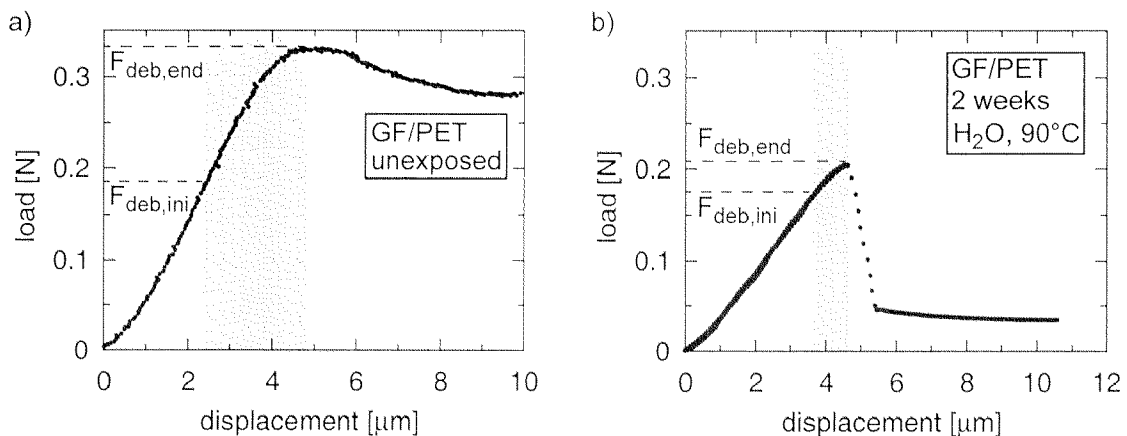


Figure 7.14: Load-displacement behavior of unexposed (a) and exposed (b) knitted GF reinforced PET. Debonding start ($F_{deb,ini}$) occurred between 1.5 and 2 N in all samples, whereas debonding was completed at significant lower load levels ($F_{deb,end}$) in exposed samples. Load drops and steady friction levels were observed exclusively in exposed GF/PET.

Load drops in push-out experiments are indications for low friction resistance. In exposed samples, a major part of the elastic energy stored in the surrounding composite was released instantly after completed debonding. This relative displacement between fiber and matrix becomes perceptible after compliance correction of the load displacement curves. No load drops were observed in experiments with unexposed samples.

Maximum interfacial stress σ_{deb} reached in exposed GF/PET was significantly lower than in unexposed samples. Maximum interfacial stress corresponds to $\sigma_{deb,end}$, i.e. maximum load divided by interface surface (see equation 47). In first approximation, $\sigma_{deb,end}$ can be considered as interface debonding strength [181]. Interfacial stress vs. compliance corrected displacement data of unexposed and exposed GF/PET samples is shown in figure 7.15.

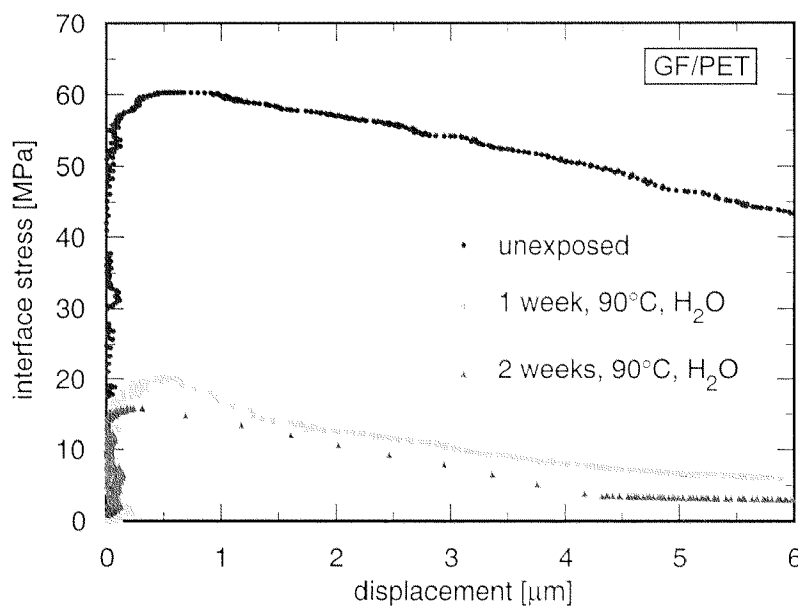


Figure 7.15: Interface stress plotted vs. compliance corrected displacement of unexposed and exposed GF/PET. A significant decrease of maximum interfacial stress and friction was observed as a consequence of immersion in water at 90°C.

The observed changes in load-displacement indicated not only decreasing interfacial properties, but also different interfacial failure behavior as a consequence of the exposure. Therefore, a microscopic investigation of the failure behavior by means of SEM and a systematic analysis of the interfacial properties was performed.

Microscopic failure behavior

Front- and backside specimen surface of push-out samples were studied using SEM to evaluate microscopic failure of the fiber/matrix interface. Significant different interface failure was observed in unexposed and exposed samples (fig. 7.16 and 7.17).

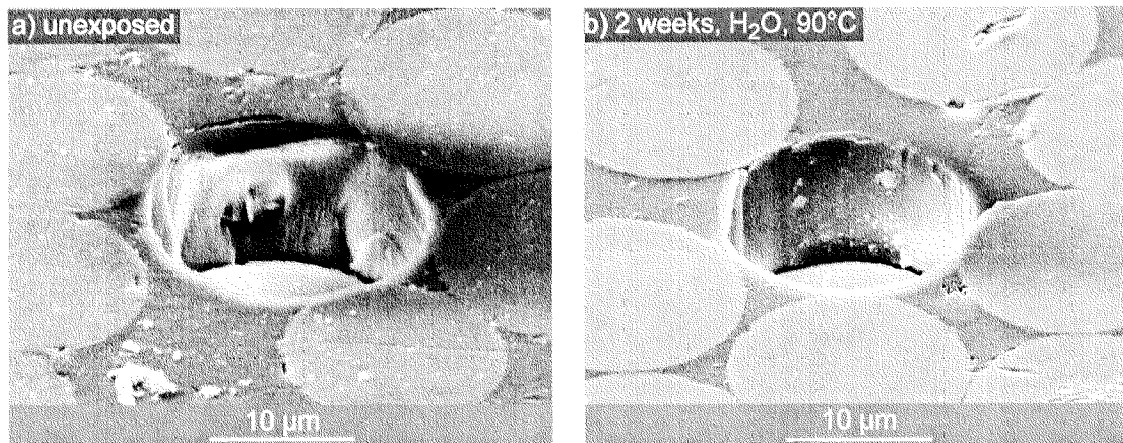


Figure 7.16: *Fibers pushed out of knitted GF reinforced PET. The surrounding matrix in unexposed samples revealed strong plastic deformation (a). After 2 weeks of exposure in water at 90°C, a more brittle failure behavior of the interface was observed (b).*

After push-out, the samples were turned to study the pushed-out fiber surfaces and to perform push-back experiments. The more plastic interface failure behavior of unexposed GF/PET could be confirmed on the backside specimen surface (fig. 7.17).

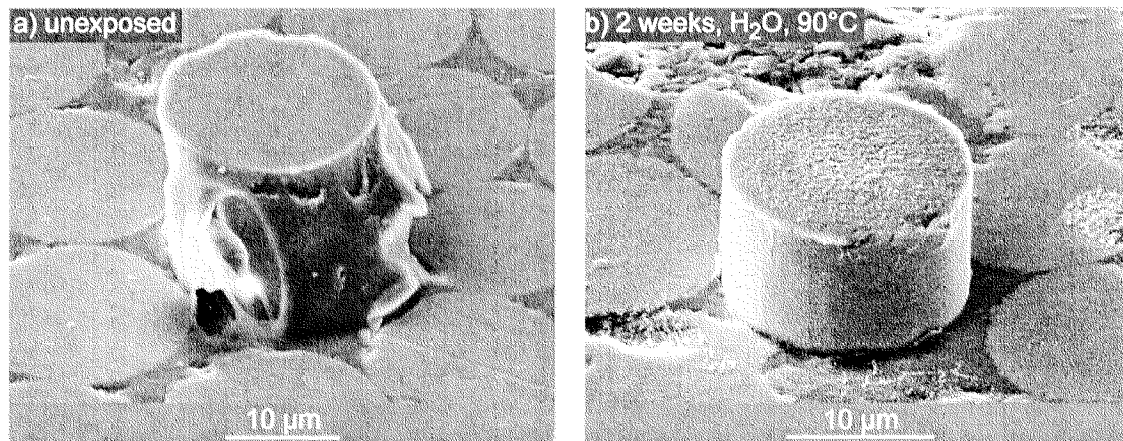


Figure 7.17: *Pushed-out fibers on the backside specimens surface. In approximately 50% of unexposed samples, fibers were found to be covered by a polymeric interphase (a), whereas brittle interface failure and matrix free fiber surfaces were observed in exposed GF/PET (b). The fiber itself did not exhibit characteristics of degradation (b).*

A polymeric interphase was observed, adhering on the fiber surfaces of approximately 50% of the unexposed samples, whereas brittle interface failure and matrix free fiber sur-

faces were found in exposed samples. The fiber itself did not exhibit characteristics of degradation. This is in accordance with the macroscopic fracture surfaces of exposed GF/PET samples (see figure 6.11).

The existence of an interphase explains the high friction level found for unexposed GF/PET. The friction measured in this samples cannot be considered as interfacial friction but rather as friction between polymeric interphase adhering to the fiber and surrounding polymer.

Push-back experiments

Push-back experiments were carried out to obtain a second value for interfacial friction. This was of particular importance because of the existence of an interphase observed on pushed out fibers in unexposed samples. Load-displacement curves of two push-back tests performed on unexposed GF/PET are shown in figure 7.18. The characteristics determined for fibers pushed further through the composite ($\sim 15 \mu\text{m}$) differed much from those of only partially pushed-out fibers ($\sim 5 \mu\text{m}$).

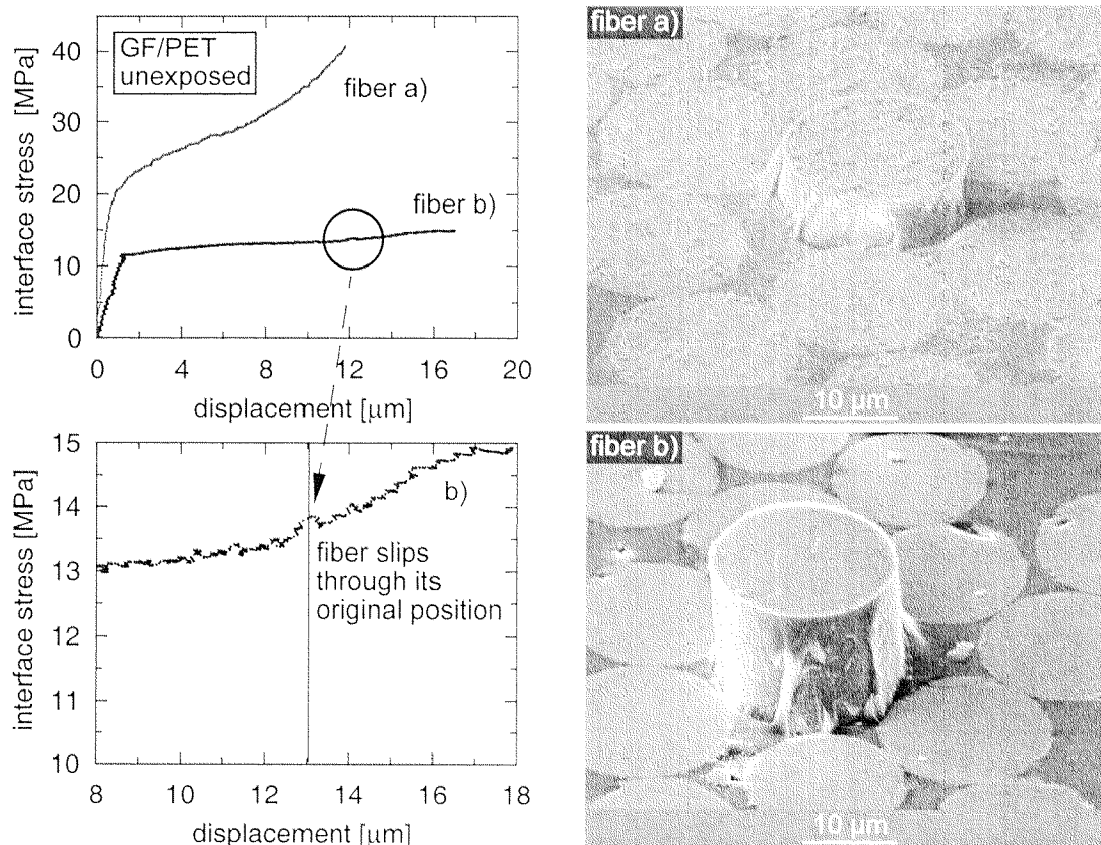


Figure 7.18: *Push-back experiments on unexposed GF/PET samples. Fibers pushed-out only partially ($\sim 5 \mu\text{m}$, (a)) showed different push-back characteristics than fibers pushed approximately $15 \mu\text{m}$ through the composite (b). When fiber a) was pushed back, load continuously increased without reaching a friction level while fiber b) showed a more typical push-back behavior with a friction stress level and a distinctive load peak when it was pushed through its original position.*

Fibers that were pushed out only approximately 5 μm out of the composite, showed continuously increasing load in push-back experiments (fig. 7.18, a). This load-displacement behavior indicated plastic deformation of the interphase. In approximately 50% of the cases, fibers that were pushed-out 15 μm and more (fig. 7.18, b) revealed steady friction levels and a typical load peak when the fibers were pushed through their original position. It is assumed that in these cases the interphase was debonded from the fiber and/or from the surrounding matrix because elongation at break of the interphases was exceeded in the preceding push-out tests. The friction τ_{fric} determined in these push-back experiments is assumed to be caused by interfacial friction and/or friction between interphase and surrounding matrix.

Interfacial friction τ_{fric} , was determined according to equation 48 at the displacement at which the fiber slipped through its original position (fig. 7.18, b). In push-back experiments without this characteristic behavior, observed with partially pushed-out fibers (fig. 7.18, a), friction was calculated at the displacement where the original fiber position was supposed to be. The original fiber position could be determined by visual observation during push-back and by the displacement covered in the corresponding push-out experiment. The high friction values determined for these partially pushed-out fibers are assumed to be caused by plastic deformation of the interphase adhering on fibers of unexposed GF/PET samples.

Interfacial friction τ_{fric} , determined in push-back experiments of unexposed and exposed samples is presented in table 7.8.

push-back	unexposed (a) (pushed-out ~ 5 μm)	unexposed (b) (pushed-out ~ 15 μm)	exposed (1 week)	exposed (2 weeks)
τ_{fric} [MPa]	31.3 \pm 2.7	13.3 \pm 1.5	6.1 \pm 0.5	3.2 \pm 0.5

Table 7.8: Interface friction determined in push-back experiments. A significant decrease as a function of exposure time was observed. The high values determined in push-back experiments of partially pushed-out fibers (a) are related with a polymeric interphase adhering to the fiber surface (fig. 7.18, a).

For the reasons mentioned above, it is assumed that the value found for partially pushed-out fibers cannot be considered as interfacial friction and are rather related to a polymeric interphase. The other results, associated with interfacial friction, were found to significantly decrease in function of the exposure time.

Interfacial properties determined with energy based models

Push-out experiments were evaluated using the push-out analyzer presented in chapter 7.2. Kerans' and Luethi's models were fitted to the measured load-displacement data. Results found for unexposed and exposed samples are summarized in table 7.9.

exposure time [days]	surface fracture energy Γ [J/m^2]	friction $\tau_0 + \mu\sigma_{cl}$ [MPa]	crack length nr/d []	Poisson component μk []
Luethi				
unexposed	13.1 ± 2.1	59.5 ± 2.4	0.86 ± 0.03	0.005 ± 0.005
7	11.9 ± 2.1	6.7 ± 1.0	0.57 ± 0.17	0.003 ± 0.002
14	15.3 ± 2.7	6.1 ± 1.8	0.79 ± 0.12	0.006 ± 0.003
Kerans				
unexposed	14.8 ± 3.1	58.6 ± 2.2	0.64 ± 0.07	0.005 ± 0.002
7	14.1 ± 2.9	6.0 ± 0.9	0.47 ± 0.15	0.008 ± 0.003
14	14.6 ± 3.2	4.9 ± 1.5	0.81 ± 0.06	0.011 ± 0.006

Table 7.9: Interfacial properties evaluated from push-out experiments using Luethi's and Kerans' energy based models. Surface fracture energy Γ did not vary significantly, whereas an important decrease of interfacial friction $\tau_0 + \mu\sigma_{cl}$ was found. The differences between the two models remained within standard deviation.

In accordance with the parametric study (figure 7.8), Poisson component μk could not be determined accurately by the energy-based models, because it has almost no influence on any point of the load-displacement curve. Standard deviations up to 100% were found. For this reason and because μk is of small importance for the total interfacial properties, it will not be further considered.

Crack length from back n , is influenced by experimental parameters like specimen thickness, as discussed in chapter 7.1.4. Since specimen thicknesses were different for exposed and unexposed samples and because n is not an interface property, it will not be subjected to discussion.

7.3.4. Discussion

Surface fracture energy. Results found for Γ revealed no significant influence of the exposure. Debonding start ($F_{deb,im}$), the parameter that mostly influences Γ , occurred at the same load levels for all samples. However, surface fracture energies determined with the push-out analyzer were found to be approximately 2.5 times higher than the values found in chapter 7.1.4. The main reason for this difference is the evaluation of interface properties using the push-out analyzer (chapter 7.2). In chapter 7.1.4, debonding start was determined manually, i.e. fitting the models to experimental data without mathematical criterions. In contrast, determination of debonding start by means of the push-out analyzer is automatically performed by calculating maximum slope of the load-displacement curve (see chapter 7.2.3), therefore providing more reliable results.

Friction. As determined with Luethi's and Kerans' model, interfacial friction after 1 week in H₂O at 90°C was reduced to approximately 10% of the value found in unexposed GF/PET. However, investigation of the backside specimen surface and push-back experiments led to the conclusion that the high friction values determined in unexposed GF/PET were related to deformation of an interphase, observed on the fiber surfaces of pushed-out fibers. This interphase was observed only in unexposed GF/PET. In push-back experiments revealing a steady friction level, friction of 13.3 ± 1.5 MPa was determined. This value can be related to actual friction, however, it remains unclear if it was caused by friction between fiber and interphase, interphase and surrounding matrix or both.

Interface debonding strength and correlation with macroscopic properties. Maximum interface stress in push-out experiments is reached when debonding is completed. The corresponding value $\sigma_{deb,end}$ was defined in equation 47 and corresponds to a first approximation of an interface debonding strength [181]. The interface debonding strength in function of exposure time is plotted in figure 7.19. The macroscopical 4-pt bending strength (chapter 6.3.3), determined previously with the specimens from which the push-out samples were taken, is shown in the same figure.

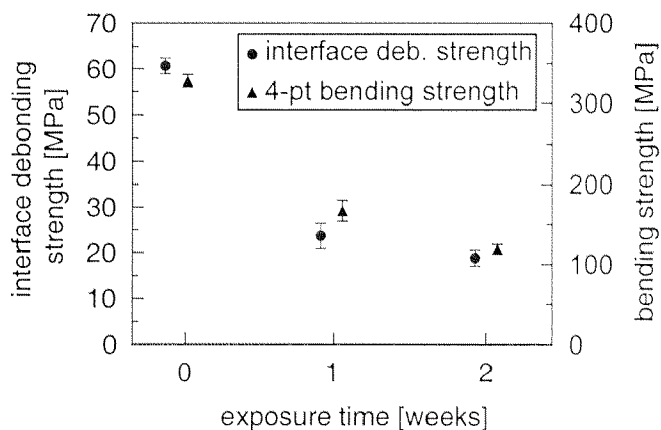


Figure 7.19: Microscopical interface debonding strength and macroscopical bending strength of knitted GF reinforced PET, determined in push-out experiments and 4-pt testing, respectively. A significant reduction of the properties with increasing exposure time was observed. Their relative decrease was found to be approximately similar.

The microscopical interface debonding strength exhibits the same relative reduction in function of exposure time than the macroscopical 4-pt bending strength. As described in chapter 6, the exposure of knitted GF reinforced PET to water at 90°C causes a reduction of matrix properties. The fact that the interface debonding strength was also found to decrease, is coherent with the SEM analysis of exposed 4-pt bending (fig. 6.11) and impact specimens (fig. 6.13), which suggested that the degradation of matrix was accompanied by a degradation of the fiber/matrix interface.

The similar relative decrease of interface debonding strength and macroscopic bending strength, caused by matrix and fiber/matrix degradation, can be understood with respect to the structure of KFRCs. The knitted fiber bundles can be modeled as straight and curved beams, as proposed by de Haan [46]. A weakness of either the matrix or the

interface reduces the strength of the fiber bundles in the intermeshing area and consequently of the complete structure. Defects in the intermeshing area were indicated by de Haan as strength reducing factors of the macroscopic structure. Therefore, interface and matrix strength is assumed to be correlated with the macroscopical strength of KFRCs. This is in accordance with the data presented in figure 7.19.

7.3.5. Conclusions

The environmental exposure of knitted GF reinforced PET in H₂O at 90°C revealed significant effects on interfacial properties determined by push-out and push-back experiments.

Interface failure behavior of unexposed GF/PET was dominated by deformation and debonding of polymeric interphase adhering on the glass fibers. This interphase could be a result of transcrystalline growth of PET on glass fibers during processing of the composite. Interfacial bonding strength of the interphase was apparently higher on glass fibers than its shear strength with respect to the surrounding PET matrix. In order to completely debond glass fibers from the surrounding composite, fibers had to be pushed-out more than 10 μm out of the composite. However, it remains unclear whether interface friction determined after completed debonding of the interphase is related to friction between fiber and interphase, interphase and surrounding matrix or both.

After exposure in H₂O at 90° interface failure was observed to be more brittle. In contrast to unexposed samples, an interphase adhering on the fibers pushed out of the composite was not observed. Experimental load-displacement curves of exposed samples revealed load drops which indicate reduced fiber friction. This effect became more pronounced with increasing exposure time. In contrast to friction, surface fracture energy Γ did not change as a consequence of environmental exposure. Γ is defined by the fiber debonding process and does not include frictional sliding. Results suggest that in both, unexposed and exposed GF/PET, it takes the same amount of energy to introduce a crack between fiber and surrounding matrix. However, in exposed samples significantly less energy is needed to push the fiber through the composite once interface bonding is destroyed.

The first approximation of interface debonding strength, i.e. maximum interface stress $\sigma_{deb,end}$ was significantly reduced as a consequence of exposure. The relative decrease of interface debonding strength was found to be similar than the relative reduction of the macroscopic 4-pt bending strength. This was attributed to a strength reducing effect of matrix and interface degradation on the macroscopical properties of KFRCs.

8. FINAL CONCLUSIONS

In the present study, micro- and macromechanical properties of plain weft-knitted fabric reinforced composites (KFRCs) were investigated. Two fiber/matrix combinations were chosen, focussing different application scopes: Knitted carbon fiber (CF) reinforced poly(ether-ether-ketone) is of interest for biomedical and aerospace applications because of its high mechanical properties and enhanced environmental resistance, whereas knitted glass fiber (GF) reinforced poly(ethylene-terephthalate) is considered for the automotive industry because of a competitive price combined with appropriate mechanical properties.

The effect of environmental degradation of CF/PEEK and GF/PET knits on mechanical properties was covered with respect to potential applications. Long-term exposure at elevated temperatures in simulated body fluid (SBF) and water was investigated. Correlations between micro- and macromechanical failure behavior were addressed to further increase the understanding of KFRCs.

Structure. The fiber bundles in CF reinforced PEEK panel were analyzed by reconstructing 2D polished sections to a 3D structure. It was found that the cross section of fiber bundles is not circular. The pressure applied throughout consolidation flattens the fiber bundles, resulting in a more elliptic shape of the bundle cross section. The ratio of bundle width to height was observed to increase from bulk to surface layer of the composite panel. The bundle geometry is considered crucial for the mechanical properties of KFRCs. The analysis of the 3D structure served as input for a mechanical model, described in [46].

The individual knit layers were found to be highly interpenetrated. In a panel consisting of 8 layers, single layers located in the bulk and surface were spread over 80% and 50% of the panel thickness, respectively. It is assumed that interpenetration is more effective in structure with large loops, as studied in this work. The high degree of interpenetration leads to increased delamination resistance.

Failure behavior. The failure behavior of KFRCs was investigated by thermography, compact tension, 4-pt bending and falling weight impact testing. Linear fracture mechanics was applied to assess out-of-plane energy release rates G_{IC} and fracture toughness K_{IC} of knitted CF reinforced PEEK in mode I. The resulting damage zones and fracture surfaces were analyzed by SEM. The following conclusions can be drawn:

- Fiber bundles play a crucial role in the failure behavior of KFRCs. In systems with high interface bonding (CF/PEEK), fiber bundles released from their environment were the smallest units observed in a damage zone resulting from compact tension, 4-pt bending and impact testing. The released bundles are compact and exhibit short fiber pull out lengths. Lower fiber/matrix interface strength (GF/PET) leads to higher pull-out lengths and to fibers released from bundles.

- Out-of-plane crack growth in wale and course direction of CF/PEEK knits is stable on a macroscopic scale, whereas it is unstable between two crack propagation steps. The crack propagation steps are controlled by fiber bundles, oriented perpendicular to the crack growth direction (pinning bundles). The fracture path follows the bundle/matrix interface of fiber bundles oriented in crack growth direction (guiding bundles). At locations with a high density of pinning bundles, crack propagation is stopped and reinitiated when a critical tensile load is reached, leading to tensile failure of the pinning bundles.
- The out-of-plane energy release rates G_{IC} and fracture toughness K_{IC} of CF/PEEK knits are high in comparison to other composite materials. K_{IC} is related with the density of pinning bundles and, therefore, is significantly higher for crack growth in course, when load is applied in wale (0° testing).
- Interlaminar failure of KFRCs is assumed to be strongly inhibited by the pronounced interpenetration of knit layers. It was shown that interlaminar fracture, caused by high shear stresses in perforation impact, did not propagate in between knit layers. Therefore, delamination is not considered to be a limiting aspect as it is in other composite systems.
- Failure characteristics in perforation impact is dependent on fiber/matrix interface strength, matrix toughness and stiffness of the KFRC. High energy dissipation and late damage initiation were observed for knitted GF reinforced amorphous PET. The amount of dissipated energy is related to the total fracture surface area consisting of released fibers and/or released fiber bundles.
- Fiber/matrix interface failure in knitted GF reinforced PET was investigated using the push-out method. Ductile failure of the interface was observed when glass fibers were pushed-out of the PET matrix. Surfaces of pushed-out fibers were found to be covered by a polymeric interphase from which it is concluded that the fiber/matrix interface exhibits a higher shear strength than the interphase.
- The failure behavior of environmentally degraded GF/PET knits was dominated by an embrittlement of the matrix and reduced interface and matrix strength. The observed reduction of 4-pt bending modulus in exposed GF/PET is attributed to early failure of matrix and interface, significantly before the ultimate bending stress is reached. Concerning impact failure, the reduced interface and matrix properties lead to an increased total fracture surface and a larger damage zone in comparison with unexposed GF/PET.

Environmental degradation. The effects of hygrothermal exposure on the mechanical properties of KFRCs was investigated with respect to their environments in potential applications. Samples were immersed in water and simulated body fluid (SBF) at 37, 60 and 90°C for exposure times up to 50 weeks.

Knitted CF reinforced PEEK exhibits excellent environmental stability. From literature, it is known that hygrothermal exposure of some CF/PEEK composites caused a significant decrease of properties which are dominated by matrix and interface. In the presented work, no significant effect of longterm exposure on fracture toughness, flex-

ural and impact properties of CF/PEEK knits was found. It is concluded that the studied material, therefore, is highly appropriate for load-bearing implants.

In contrast to the outstanding environmental resistance of CF/PEEK, knitted GF reinforced PET was found to be considerably affected by hygrothermal exposure. After one and two weeks of exposure to water at 90°C, a reduction of bending strength to 50 and 35% of the initial value was determined, respectively. Dissipated energy and peak force in perforation impact decreased. The lower properties are attributed to a severe degradation of the PET matrix by hydrolysis. Matrix degradation is accompanied by a decrease of interface debonding strength which was shown in push-out experiments. A relation between the reduction of interface debonding strength and 4-pt bending strength was found. The observed correlation led to the assumption that weakness of either the matrix or the interface reduces the strength of the fiber bundle in the intermeshing area and consequently of the complete structure. This is in accordance with de Haan, who indicated defects in the intermesh as strength reducing factors of the macroscopic structure by [46].

With respect to automotive applications, the environmental sensitivity of GF/PET has to be addressed by avoiding moisture contact. Even though the hydrolysis of PET is slower at lower temperatures, the temperatures at which cars are regularly exposed to are relatively high (e.g. during insolation). Considering a 50% reduction of bending properties, determined after one week in water at 90°C, it has to be expected that over the life time of a car, moisture and service temperatures would cause degradation effects strong enough to reduce the performance of GF/PET to a critical level.

Outlook. It has been shown that KFRCs are versatile materials which exhibit damage tolerant failure behavior. Because of the variety of knit structures and the possibility to combine almost any fiber/matrix material, KFRCs have a high potential in various application fields.

Knitted fabrics, as biomaterials, can adopt load-bearing functions when used as reinforcement of biocompatible, high performance polymers, e.g. PEEK. Another currently investigated option is the application of knitted textiles in tissue engineering. The high specific surface area and the open structure of knitted yarns are assumed to enable in-growing tissue. By using elastomeric biodegradable matrices, KFRCs with low stiffness and high elongation at break can be reached, thus approaching the properties of soft tissues.

A topic of further research is the “missing link” between the loop geometry in the textile fabric or prepreg sheets and the loop geometry in the final part. The need to predict the local reinforcement structure in applications can be approached with analysis and modeling of the loop deformation upon processing and shaping.

9. REFERENCES

- [1] Bunsell A. R., Composite Materials Series, in *Fibre Reinforcements for Composite Materials*, vol. 2, Pipes R. B., ed., Amsterdam, Elsevier, 1988, pp. 537.
- [2] Arendts F. J., Drechsler K., Brandt J., Advanced textile structural composites - status and outlook, *Proceedings of the International Conference on Advanced Composite Materials*, 1993, pp. 409-416.
- [3] Johnson C., Automotive applications for textile based composite structures, *TEX Comp 3*, Aachen, 1996, p. 24/1
- [4] Drechsler K., Brandt J., Applications of composites in transportation industry, *TEX Comp 3*, Aachen, 1996, pp. 25/1-20.
- [5] Williams D. F., Consensus and definitions in biomaterials, in *Advances in biomaterials*, 8, de Putter C., de Lange K., de Groot K., Lee A. J. C., eds., Amsterdam, Elsevier Science, 1988, pp. 11-16.
- [6] Wintermantel E., Werkstoffe für Medizin und Umwelt: Innovation durch Biokompatibilität, *Inauguration lecture*, ETH Zurich, 1993.
- [7] Wintermantel E., Mayer J., Anisotropic biomaterials: strategies and developments for bone implants, in *Encyclopedic Handbook of Biomaterials and Bioengineering*, Part B-1, Wise D. L., Trantolo D. J., Altobelli D. E., Yaszemski J. D., Gresser J. D., Schwartz E. R., eds., New York, Dekker, 1995, pp. 3-42.
- [8] Chang F. K., Perez J. L., Davidson J. A., Stiffness and strength tailoring of a hip prosthesis made of advanced composite materials, *Journal of Biomedical Materials Research*, 24, 1990, pp. 873-899.
- [9] Shirandami R., New design of hip prosthesis using carbon fibre reinforced composite, *Journal of Biomedical Engineering*, 12(1), 1990, pp. 19-22.
- [10] Cheal E. J., Grierson A. E., Reilly D. T., Sledge C. B., Spector M., Comparative study of carbon polymer composite and titanium femoral stems in dogs using computed tomography, *ASTM Special Technical Publication*, 1993, pp. 4-16.
- [11] Widmer M. S., Faserverstärkte Hüftprothesenschäfte - Untersuchungen zu ihrer Herstellung in wirtschaftlichen Verfahren, darunter dem Spritzgussprozess, Department of Materials, ETH Zurich, 1995.
- [12] Otani T., Whiteside L., White S., McCarthy D., Effects of femoral component material properties on cementless fixation in total hip arthroplasty. A comparison study between carbon composite, titanium alloy, and stainless steel, *Arthroplasty*, 8(1), 1993, pp. 67-74.
- [13] Yildiz H., Ha S., Chang F., Composite hip prosthesis design. I. Analysis, *Journal of Biomedical Materials Research*, 39(1), 1998, pp. 92-101.
- [14] Yildiz H., Chang F., Goodman S., Composite hip prosthesis design. II. Simulation, *Journal of Biomedical Materials Research*, 39(1), 1998, pp. 102-119.
- [15] Akeson W. H., Woo S. L., Coutts R. D., Matthews J. V., Gonsalves M., Amiel D., Quantitative histological evaluation of early fracture healing of cortical bones immobilized by stainless steel and composite plates, *Calcified Tissue International*, 19(1), 1975, pp. 27-37.
- [16] McKibbin B., Biological considerations in osteosynthesis, *Chirurgie*, 115(9), 1989, pp. 683-686.
- [17] Prakash R., Marwah S., Goel S., Tuli S., Carbon fibre reinforced epoxy implants for bridging large osteoperiosteal gaps, *Biomaterials*, 9(2), 1988, pp. 198-202.
- [18] Mayer J., Gestricke aus Kohlenstoffasern für biokompatible Verbundwerkstoffe, dargestellt an einer homoelastischen Osteosyntheseplatte, Department of Materials, ETH Zurich, 1994.
- [19] Zimmerman M., Parsons J., Alexander H., The design and analysis of a laminated partially degradable composite bone plate for fracture fixation, *Journal of Biomedical Materials Research*, 21, 1987, pp. 345-361.
- [20] Bao Q. B., McCullen G. M., Higham P. A., Dumbleton J. H., Yuan H., The artificial disc: theory, design and materials, *Biomaterials*, 17(12), 1996, pp. 1157-1167.

- [21] Shono Y., McAfee P., Cunningham B., Brantigan J., A biomechanical analysis of decompression and reconstruction methods in the cervical spine. Emphasis on a carbon-fiber-composite cage, *Journal of Bone and Joint Surgery, American Volume*, 75(11), 1993, pp. 1674-1684.
- [22] Ciappetta P., Boriani S., Fava G., A carbon fiber reinforced polymer cage for vertebral body replacement: technical note, *Neurosurgery*, 41(5), 1997, pp. 1203-1206.
- [23] Parsons J. R., Lee C. K., Langrana N. A., Clemow A. J., Chen E. H., Functional and biocompatible intervertebral disc spacer containing elastomeric material of varying hardness, US Patent 5-171-281, 1992.
- [24] Ramakrishna S., Application of textiles and textile composites for biomaterials development, *TEX Comp 3*, Aachen, 1996, pp. 27/1-27.
- [25] Latour R. A., Jr., Black J., Miller B., Fracture mechanisms of the fiber/matrix interfacial bond in fiber-reinforced polymer composites, *Surface and Interface Analysis*, 17(7), 1991, pp. 477-484.
- [26] Latour R. A., Jr., Black J., Development of FRP composite structural biomaterials: Ultimate strength of the fiber/matrix interfacial bond in *in vivo* simulated environments, *Journal of Biomedical Materials Research*, 26, 1992, pp. 593-606.
- [27] Latour R. A., Black J., Fiber-reinforced polymer composite biomaterials: characterization of interfacial bond strength and environmental sensitivity, in *Biomaterials' Mechanical Properties, ASTM STP 1173*, Kambic H. E., Yokobori A. T., eds., Philadelphia, American Society for Testing and Materials, 1994, pp. 193-211.
- [28] Meyer M. R., Friedman R. J., Del Schutte H., Jr., Latour R. A., Jr., Long-term durability of the interface in FRP composites after exposure to simulated physiologic saline environments, *Journal of Biomedical Materials Research*, 28(10), 1994, pp. 1221-1231.
- [29] Wagner H. D., Lustiger A., Effect of water on the mechanical adhesion of the glass/epoxy interface, *Composites*, 25(7), 1994, pp. 613-616.
- [30] Ma C. C. M., Yur S. W., Environmental effect on the water absorption and mechanical properties of carbon fiber reinforced PPS and PEEK composites, *Annual Technical Conference and Exhibition of the Society of Plastics Engineers*, 47, 1989, pp. 1496-1500.
- [31] Horn W. J., Shaikh F. M., Soeganto A., Degradation of mechanical properties of advanced composites exposed to aircraft environment, *American Institute of Aeronautics Journal*, 27(10), 1989, pp. 1399-1405.
- [32] Maharaj G. R., Strait L. H., Gavens A. J., Jamison R. D., Characterization of creep and environmental effects on composite materials for human hip prostheses, 8th International Conference on Composite Materials (ICCM-VIII), Honolulu, USA, 1991, pp. 7A/1-10.
- [33] Ma C. C. M., Huang Y. H., Chang M. J., Ong C. L., Sheu M. F., Hygrothermal effect on the PEEK/C.F. and PPS/C.F. under impact loading (I), *In Search of Excellence Annual Technical Conference, ANTEC Conference Proceedings.*, 37. Publ by Soc of Plastics Engineers, Brookfield, CT, USA., 1991, pp. 2092-2096.
- [34] Juska T., Effect of water immersion on fiber/matrix adhesion in thermoplastic composites, *Journal of Thermoplastic Composite Materials.*, 6(4), 1993, pp. 256-274.
- [35] Yang B., Hojo M., Tanaka K., Effect of water environment on propagation of delamination fatigue crack in thermoplastic composite laminates, *Fuhe Cailiao Xuebao Acta Materiae Compositae Sinica.*, 11(4), 1994, pp. 95-103.
- [36] Selzer R., Friedrich K., Influence of water up-take on interlaminar fracture properties of carbon fibre-reinforced polymer composites, *Journal of Materials Science*, 30, 1995, pp. 334-338.
- [37] Zhao S., Gaedke M., Moisture effects on Mode II delamination behavior of carbon/epoxy composites, *Advanced Composite Materials*, 5(4), 1996, pp. 291-307.
- [38] Zhang G. G., Latour R. A., Kennedy J. M., Delschutte H., Friedman R. J., Long term compressive property durability of carbon fibre reinforced polyetheretherketone composite in physiological saline, *Biomaterials*, 17 (8), 1996, pp. 781-789.
- [39] Adams R. D., Singh M. M., The dynamic properties of fibre-reinforced polymers exposed to hot, wet conditions, *Composites Science and Technology*, 56(8), 1996, pp. 977-997.

- [40] Ma C. C. M., Lee C. L., Chang M. J., Tai N. H., Hygrothermal behavior of carbon fiber-reinforced poly (ether ether ketone) and poly (phenylene sulfide) composites, *Polymer Composites*, 13(6), 1992, pp. 448-453.
- [41] Storfer-Isser N. I., Clegg W. J., Environmental degradation of the transverse properties in APC-2, *13th European Conference on Biomaterials*, Göteborg Sweden, 1997, p. LMP16.
- [42] Mayer J., Wintermantel E., Influence of knit structure and fiber matrix adhesion on failure mechanisms of knitted carbon fiber reinforced thermoplastics, *4th Japan Int. SAMPE Symposium*, Tokyo, Japan, 1995, pp. 667-672.
- [43] Chou T.-W., Ko F.-K., Textile structural composites, in *Composite Materials Series*, vol. 3, Pipes R. B., ed., Amsterdam, Elsevier, 1989, pp. 387.
- [44] Ko F. K., Three-dimensional fabrics for composites, in *Textile Structural Composites*, vol. 2, Chou T.-W., Ko F. K., eds., Amsterdam, Elsevier, 1989, pp. 129-172.
- [45] Fukuta K., Onooka R., Aoki E., Nagatsuka Y., *15th Textile Research Symposium*, Osaka, 1984, pp. 36-38.
- [46] de Haan J., Structure-property relations in plain weft-knitted fabric reinforced composites (KFRCs) preparing load-bearing implants: Experimental study and beam model approach, Department of Materials, Swiss Federal Institute of Technology, 1999.
- [47] Gommers B., Verpoest I., Vanhoutte P., Modelling the elastic properties of knitted fabric reinforced composites, *Composites Science and Technology*, 56(6), 1996, pp. 685-694.
- [48] Mayer J., de Haan J., Reber R., Knitted Carbon Fiber Reinforced Thermoplastics: An Overview, *First Asian-Australian Conference on Composite Materials (ACCM-1)*, Osaka, Japan, 1998, pp. 401/1-4.
- [49] Byun J. H., Chou T. W., Modelling and characterization of textile structural composites: a review, *Journal of Strain Analysis for Engineering Design*, 24(4), 1989, pp. 253-262.
- [50] Wulforth B., Moll K. U., Determination of stitching as a new method to reinforce composites, *TEX Comp 3*, Aachen, Germany, 1996, pp. 4/1-12.
- [51] Weimer C., Mitschang P., Neitzel M., Selection and improvement of a feeding-system for minimised fibre damage in stitsched textile composites, *TEX Comp 4*, Kyoto, Japan, 1998, pp. O2/1-8.
- [52] Scardino, An introduction to textile structures and their behavior, in *Textile Structural Composites*, 2, Chou T.-W., Ko F. K., eds., Amsterdam, Elsevier, 1989, pp. 1-26.
- [53] Hoffmann L., Yu T. P., Wang S. S., Fracture of knitted randomly oriented short-fiber composite, *International Journal of Fracture*, 74(4), 1995, pp. 363-381.
- [54] Chang F.-K., Chang K.-Y., Engdahl R., Modeling of unidirectional performed composites, *Journal of Reinforced Plastics and Composites*, 7(6), 1988, pp. 582-600.
- [55] Lebrun G., Boukhili R., Gauvin R., Delamination behavior of non-woven bidirectional fabric composites, *24th International SAMPE Technical Conference*, Toronto, Canada, 1992, pp. T484-496.
- [56] Hoffmann L., Wang S. S., Cyclic fatigue crack growth and fracture in knitted randomly oriented short-fiber composite, *Engineering Fracture Mechanics*, 52(6), 1995, pp. 1151-1163.
- [57] Wang Y., Li J., Do P. B., Properties of composite laminates reinforced with knitted multi-layer non-crimp fabrics, *50 Years of Progress in Materials and Science Technology International SAMPE Technical Conference*, 26. SAMPE, Covina, CA, USA, 1994, pp. 88-95.
- [58] Wang Y., Li J., Do P. B., Properties of composite laminates reinforced with E-glass multiaxial non-crimp fabrics, *Journal of Composite Materials*, 29(17), 1995, pp. 2317-2333.
- [59] Stumpf H., Mader E., Baeten S., Pisanikovski T., Zah W., Eng K., Andersson C. H., Verpoest I., Schulte K., New thermoplastic composite preforms based on split-film warp-knitting, *Composites Part A (Applied Science and Manufacturing)*, 29A(12), 1998, pp. 1511-1523.
- [60] Youjiang W., Jian L., Do P., Properties of composite laminates reinforced with E-glass multiaxial non-crimp fabrics, *Journal of Composite Materials*, 29(17), 1995, pp. 2317-2333.

- [61] Bibo G., Hogg P., Kemp M., Mechanical characterisation of glass- and carbon-fibre-reinforced composites made with non-crimp fabrics, *Composites Science and Technology*, 57(9-10), 1997, pp. 1221-1241.
- [62] Buck A., German Patent Application DE 3108041 C2.
- [63] Marvin A. W., Some mechanical properties of knitted glass laminates, *Journal of the Textile Institute*, 52, 1961, pp. 21-25.
- [64] Varin R. R., Knitted fabrics in fiber reinforced structural composites, *27th National SAMPE Symposium and Exhibition*, San Diego, CA, 1982, pp. 659-666.
- [65] Rudd C. D., Owen M. J., Middleton V., Mechanical properties of weft knit glass fibre/polyester laminates, *Composites Science and Technology*, 39(3), 1990, pp. 261-277.
- [66] Anon, Knitted-fiber-reinforced composites, *Automotive Engineering*, 102(8), 1994, pp. 21-24.
- [67] Hamada H., Nakai A., Fujita A., Inoda M., Mechanical properties of weft knitted fabric reinforced composites, *Advanced Composites Letters*, 4(3), 1995, pp. 83-85.
- [68] Youjiang W., Gowayed Y., Xiangming K., Jian L., Dongming Z., Properties and analysis of composites reinforced with E-glass weft-knitted fabrics, *Journal of Composites Technology and Research*, 17(4), 1995, pp. 283-288.
- [69] Karger-Kocsis J., Czigany T., Gaal J., Ostgathe M., Stiffness and strength anisotropy in the tensile response of weft knitted fabric-reinforced PEEK- and PET-composites, *Advanced Composites Letters*, 5(3), 1996, pp. 71-75.
- [70] de Haan J., Peijs T., Mechanical properties of flexible knitted composites, *Advanced Composites Letters*, 5(1), 1996, pp. 9-13.
- [71] Ramakrishna S., Tang Z., Teoh S., Tsai K., Knitted fabric reinforced flexible composite material, *Key Engineering Materials*, 137, 1997, pp. 16-23.
- [72] de Haan J., Reber R., Mayer J., Wintermantel E., Knitted carbon fibre reinforced materials. Composites for load bearing implants: strength criteria, *The 4th International Symposium for Textile Composites: Texcomp*, Kyoto, Japan, 1998, pp. P3/1-4.
- [73] de Haan J., Fischbach T., Reber R., Mayer J., Wintermantel E., Comparison of plain weft knitted carbon fibre reinforced thermoplastics and thermosets, *The 4th International Symposium for Textile Composites: Texcomp*, Kyoto, Japan, 1998, pp. O8/1-6.
- [74] Mayer J., de Haan J., Kirch M., Wild U., Wintermantel E., Structure and mechanical properties of knitted carbon fiber reinforced polyamide 12, *Journal of Thermoplastic Composite Materials*, 1998, in press.
- [75] Mayer J., de Haan J., Reber R., Wilde D., Ziegmann G., Wintermantel E., Knitted carbon and glass fiber reinforced thermoplastics: potentials and limitations, *Techtextil ASIA*, Osaka, Japan, 1998, pp. 75-83.
- [76] Ramakrishna S., Hull D., Tensile behaviour of knitted carbon-fibre-fabric/epoxy laminates - part I: experimental, *Composites Science and Technology*, 50(2), 1994, pp. 237-247.
- [77] Gommers B., Verpoest I., Van H. P., Determination of the mechanical properties of composite materials by tensile tests. I. Elastic properties, *Journal of Composite Materials*, 32(4), 1998, pp. 310-334.
- [78] Gommers B., Verpoest I., Van H. P., Determination of the mechanical properties of composite materials by tensile tests. II. Strength properties, *Journal of Composite Materials*, 32(2), 1998, pp. 102-122.
- [79] Ramakrishna S., Hull D., Energy absorption capability of epoxy composite tubes with knitted carbon fibre fabric reinforcement, *Composites Science and Technology*, 49(4), 1993, pp. 349-56.
- [80] Mayer J., Wintermantel E., Failure behavior of knitted carbon fiber reinforced thermoplastics, *Euromat 95*, Venice/padua, 1995, pp. 1-6.
- [81] de Haan J., Kameo K., Nakai A., Fujita A., Mayer J., Wintermantel E., Hamada H., Notched strength of knitted fabric composites, *International Conference on Composite Materials, ICCM II*, Gold Coast, Queensland, Australia, 1997, pp. 219-226.

- [82] Reber R., de Haan J., Petitmermet M., Mayer J., Wintermantel E., Intralaminar fracture toughness of weft-knitted carbon fiber reinforced PEEK, *2nd ESIS TC4 Conference on Polymers and Composites*, Les Diablerets, Switzerland, 1998, in press.
- [83] Reber R., de Haan J., Mayer J., Wintermantel E., Failure behavior of weft knitted carbon fiber reinforced PEEK, *The First Asian-Australian Conference on Composite Materials*, Osaka, Japan, 1998, pp. 407/1-4.
- [84] Xiaoping R., Tsu W. C., Failure behavior of knitted fabric composites, *Journal of Composite Materials*, 32(3), 1998, pp. 198-222.
- [85] Czigany T., Ostgathe M., Karger-Kocsis J., Damage development in GF/PET composite sheets with different fabric architecture produced of a commingled yarn, *Journal of Reinforced Plastics and Composites*, 17(3), 1998, pp. 250-267.
- [86] Shen C., Chi J. W., A study of the physical properties of epoxy resin composites reinforced with knitted glass fiber fabrics, *Journal of Reinforced Plastics and Composites*, 11(11), 1992, pp. 1239-1250.
- [87] Ramakrishna S., Hamada H., Impact damage resistance of knitted glass fiber fabric reinforced polypropylene composites, *Science and Engineering of Composite Materials*, 4(2), 1995, pp. 61-72.
- [88] Karger-Kocsis J., Yuan Q., Mayer J., Wintermantel E., Transverse impact behavior of knitted carbon fiber fabric reinforced thermoplastic composite sheets, *Journal of Thermoplastic Composite Materials*, 10(2), 1997, pp. 163-172.
- [89] Shen C., Hong C. C., Che C. L., The fatigue properties of weft-knit fabric reinforced epoxy resin composites, *Composites Science and Technology*, 45(4), 1992, pp. 283-291.
- [90] Moos E., Karger-Kocsis J., Effects of knit stretching and matrix crystallinity on the fatigue behaviour of knitted fabric-reinforced GF/PET composites, *Advanced Composites Letters*, 6(3), 1997, pp. 75-79.
- [91] de Haan J., Reber R., Mayer J., Wintermantel E., Static and fatigue testing of knitted carbon fiber reinforced polyamide 12 (CF/PA12) composites, *JEC/SAMPE 99*, Paris, 1999, in press.
- [92] Luethi B., Reber R., Mayer J., Wintermantel E., Janczak-Rusch J., Rohr L., Characterization of the GF/PET interface in knitted composites by means of the push-out technique, *Symposium of Interfacial Materials Science on Composite Materials 97*, Osaka, Japan, 1997, pp. 503-506.
- [93] Karger-Kocsis J., Moos E., Czigany T., Effects of interphase and fibre content on the mechanical behavior of weft-knitted glass fibre reinforced polypropylene, *Advanced Composites Letters*, 6(2), 1997, pp. 31-36.
- [94] Karger-Kocsis J., Czigany T., Effects of interphase on the fracture and failure behavior of knitted fabric reinforced composites produced from commingled GF/PP yarn, *Composites Part A (Applied Science and Manufacturing)*, 29A(9-10), 1998, pp. 1319-1330.
- [95] Mayer J., Giorgetta S., Koch B., Wintermantel E., Patscheider J., Spescha G., Characterization of thermally oxidized carbon fibre surfaces by ESCA, wetting techniques and scanning probe microscopy, and the interaction with polyethylmethacrylate. Development of a biocompatible composite material, *Composites*, 25(7), 1994, pp. 763-769.
- [96] Luethi B., Reber R., Mayer J., Wintermantel E., Janczak-Rusch J., Rohr L., An energy-based analytical push-out model applied to characterise the interfacial properties of knitted glass fibre reinforced PET, *Composites Part A*, 29A(12), 1998, pp. 1553-1562.
- [97] Ramakrishna S., Hull D., Tensile behaviour of knitted carbon-fibre-fabric/epoxy laminates. II. Prediction of tensile properties, *Composites Science and Technology*, 50(2), 1994, pp. 249-258.
- [98] Ramakrishna S., Characterization and modeling of the tensile properties of plain weft-knit fabric-reinforced composites, *Composites Science and Technology*, 57(1), 1997, pp. 1-22.
- [99] Ramakrishna S., Analytical and finite element modeling of elastic behavior of plain-weft knitted fabric reinforced composites, *Key Engineering Materials*, 137, 1997, pp. 71-78.

- [100] de Haan J., Peijs T., Mayer J., Wintermantel E., Modelling of the deformation behaviour of flexible knitted composites, *European Conference on Composite Materials*, London UK, 2, 1996, pp. 421-427.
- [101] Huysmans G., Gommers B., Verpoest I., A binary finite element model for the effective stiffness prediction of 2D warp knitted fabric composites, *4th International Conference on Deformation and Fracture of Composites*, Manchester UK, 1997, pp. 309-318.
- [102] Kelay M., Bader D., Reed P., Mechanical deformation mechanisms in knitted fabric composites, *Journal of Thermoplastic Composite Materials*, 10(1), 1997, pp. 76-84.
- [103] Huysmans G., Verpoest I., Van H. P., A poly-inclusion approach for the elastic modelling of knitted fabric composites, *Acta Materialia*, 46(9), 1998, pp. 3003-3013.
- [104] Gommers B., Verpoest I., Van H. P., Analysis of knitted fabric reinforced composites. I. Fibre orientation distribution, *Composites Part A (Applied Science and Manufacturing)*, 29A(12), 1998, pp. 1579-1588.
- [105] Gommers B., Verpoest I., Van H. P., The Mori-Tanaka method applied to textile composite materials, *Acta Materialia*, 46(6), 1998, pp. 2223-2235.
- [106] Wilde D., Ziegmann G., Knitted fabric reinforced thermoplastics - properties and applications, *Techtextil 97*, Frankfurt a. Main, 1997.
- [107] Gommers B., The elastic properties of knitted fabric composites, Department of Materials Science, Katholieke Universiteit Leuven, 1997.
- [108] Ko F. K., Du W., Processing of textile preforms, in *Science and Innovation in Polymer Composites Processing*, Cambridge, Massachusetts Institute of Technology, 1992.
- [109] Bogdanovic A. E., Pastore C. M., Mechanics of textile and laminated composites, London, Chapman and Hall, 1996, pp. 237-239.
- [110] de Haan J., Mayer J., Reber R., Tensile properties of plain weft knitted carbon fiber reinforced polyamide 12 composites, *1st Asian-Australian Conf. Comp. Mat. (AACCM-1)*, Osaka, Japan, 1998, pp. 403/1-4.
- [111] Ko F., Global activities in advanced textile preforming, *TEX Comp 3*, Aachen, 1996, pp. 1/1-4.
- [112] Brite Euram project report (BRE2-0938, BE-7290), Subtask 5.2: Optimisation of processing parameters with double belt press, in: Property tailoring and net shape proceeding of structures from textile preforms with thermoplastic matrices, 1999.
- [113] Niskanen K. J., Sadowski J. W., Evaluation of some fibre orientation measurements, *Trans Tech Sect Can Pulp Pap Assoc*, 15, 1989, pp. J220-J224.
- [114] Toll S., Andersson P. O., Microstructure of long- and short-fiber reinforced injection molded polyamide, *Polymer Composites*, 14(2), 1993, pp. 116-125.
- [115] Lorensen W., Cline H., Marching cubes: a high resolution 3D surface construction algorithm, *Computer Graphics*, 21(4), 1987, pp. 163-169.
- [116] Beehag A., Ye L., Role of cooling pressure on interlaminar fracture properties of commingled CF/PEEK composites, *Composites Part A: Applied Science and Manufacturing*, 27(3), 1996, pp. 175-182.
- [117] Hojo M., Kageyama K., Tanaka K., Prestandardization study on mode I interlaminar fracture toughness test for CFRP in Japan, *Composites*, 26(4), 1995, pp. 243-255.
- [118] Yoon H., Takahashi K., Mode I interlaminar fracture toughness of commingled carbon fibre/PEEK composites, *Journal of Materials Science*, 28(7), 1993, pp. 1849-1855.
- [119] Petitmermet M., Double Cantilever Beam (DCB)-Versuche zur Charakterisierung der Mode I Delamination von mit Kohlenstofffasern Gestricken verstärkten Thermoplasten, Internal Research, Professur für Biokompatible Werkstoffe und Bauweisen, ETH Zürich, 1992.
- [120] Schuster J., Friedrich K., Thermography of damage propagation in polymer composites during fatigue testing, *Materialprüfung*, 36(7-8), 1994, pp. 298-301.
- [121] Dibley D., Thermography optimizes composites manufacture, *Materials-World*, 5(1), 1997, pp. 21-23.

- [122] Henneke E. G., Thermography - an NDT method for damage investigation in composite materials, *Microstructural Science.*, 14, 1987, pp. 521-537.
- [123] Karger Kocsis J., Fejes Kozma Z. S., Failure mode and damage zone development in a GMT-PP by acoustic emission and thermography, *Journal of Reinforced Plastics and Composites.*, 13(9), 1994, pp. 768-792.
- [124] Laine Arto J., Detection of failures in plastic composites using thermography, *Proceedings of SPIE: The International Society for Optical Engineering.*, 1992, pp. 207-212.
- [125] Richard H. A., Benitz K., A loading device for the creation of mixed mode in fracture mechanics, *International Journal of Fracture*, 22, 1983, pp. R55-R58.
- [126] Kageyama K., Kobayashi I., Chou T. W., Analytical compliance method for mode I interlaminar fracture toughness testing of composites, *Composites*, 18(5), 1987, pp. 393-399.
- [127] Cowley K. D., Beaumont P. W. R., The interlaminar and intralaminar fracture toughness of carbon-fibre/polymer composites: the effect of temperature, *Composite Science and Technology*, 57, 1997, pp. 1433-1444.
- [128] Narisawa I., Yee A. F., Cracking and fracture of polymers, in *Structure and Properties of Polymers*, 12, Thomas E. L., ed., Weinheim, New York, Basel, Cambridge, Tokyo, VCH, 1993, pp. 699-767.
- [129] Wigent D. E., Mohamend M. H., Fahmy A. A., Fracture and fatigue in a 3-D woven carbon fiber/epoxy composite, *International SAMPE Symposium and Exhibition*, Anaheim, USA, 1996, pp. 1217-1229.
- [130] Gribi M. A., Bruchzähigkeiten von Aluminium-Silizium-Magnesium-Gusslegierungen, Department of Materials, ETH Zurich, 1985.
- [131] Froes F. H., Yau T.-L., Weidinger H. G., Titanium, zirconium and hafnium, in *Structure and Properties of Nonferrous Alloys*, 8, Matucha K. H., ed., Weinheim, New York, Basel, Cambridge, Tokyo, VCH, 1996, pp. 399-469.
- [132] Jones R., Baker A., Callinan R., Residual strength of impact damaged composites, *International Journal of Fracture*, 24(1), 1984, p. R51.
- [133] Bibo G. A., Hogg P. J., The role of reinforcement architecture on impact damage mechanisms and post-impact compression behaviour, *Journal of Materials Science*, 31(5), 1996, pp. 1115-1137.
- [134] Brite Euram project report (BRE2-0938, BE-7290), Property tailoring and net shape proceeding of structures from textile preforms with thermoplastic matrices, 1999.
- [135] Jones D. P., Leach D. C., Moore D. R., The application of instrumented falling weight impact techniques to the study of toughness in thermoplastics, *Plastic and Rubber Processing and Applications*, 6(1), 1986, pp. 67-79.
- [136] Reed P. E., Falling weight impact testing and design, *Plastics, Rubber and Composites Processing and Applications*, 17(3), 1992, pp. 157-163.
- [137] Yee F. C., Lam W. C., Interface and its effect on the properties of composites, *Proceedings of the International Conference on Advanced Composite Materials*, 1993, pp. 417-421.
- [138] Karger-Kocsis J., Moos E., Mouzakis D. E., Perforation impact response of bimaterial sheet composed of high density polyethylene and high density polyethylene with discontinuous Selar microlayers, *Plastics, Rubber and Composites Processing and Applications.*, 26(4), 1997, pp. 178-183.
- [139] Chou S., Chen Hong C., Chen Hong E., Effect of weave structure on mechanical fracture behavior of three-dimensional carbon fiber fabric reinforced epoxy resin composites, *Composites Science and Technology*, 45(1), 1992, pp. 23-35.
- [140] Larsson F., Damage tolerance of a stitched carbon/epoxy laminate, *Composites Part A (Applied Science and Manufacturing)*, 28A(11), 1997, pp. 923-934.
- [141] Lowe A. C., Moore D. R., Robinson I. M., Data for designing with continuous-glass-fibre-reinforced polypropylene, *Composites Science and Technology.*, 52(2), 1994, pp. 205-216.
- [142] Morton J., Godwin E. W., Impact response of tough carbon fiber composites, *Composite Structures*, 1989, pp. 1-19.

- [143] Cantwell W. J., Morton J., The impact resistance of composite materials - a review, *Composites*, 22(5), 1991, pp. 347-362.
- [144] Kemmish D., Hay J., The effect of physical ageing on the properties of amorphous PEEK, *Polymer*, 26(6), 1985, pp. 905-912.
- [145] Buggy M., Carew A., Effect of thermal ageing on carbon fibre-reinforced polyetheretherketone (PEEK) part I static and dynamic flexural properties, *Journal of Materials Science*, 29(7), 1994, pp. 1925-1929.
- [146] Leach D. C., Cogswell F. N., Nield E., High temperature performance of thermoplastic aromatic polymer composites, *Materials Sciences for the Future. 31st International SAMPE Symposium and Exhibition*, Las Vegas USA, 1986, pp. 434-448.
- [147] Ma C. C. M., Lee C. L., Chang M. J., Tai N. H., Effect of physical aging on the toughness of carbon fiber-reinforced poly (ether ether ketone) and poly (phenylene sulfide) composites, *Polymer Composites.*, 13(6), 1992, pp. 441-447.
- [148] Nguyen H. X., Ishida H., Poly(aryl-ether-ether-ketone) and its advanced composites: a review, *Polymer Composites*, 8(2), 1987, pp. 57-73.
- [149] Wang Q., Springer G. S., Moisture absorption and fracture toughness of PEEK polymer and graphite fiber reinforced PEEK, *Journal of Composite Materials*, 23(5), 1989, pp. 434-447.
- [150] Pritchard G., Randles S. J., Long fibre thermoplastics for aerospace, *BFF Reinforced Plastics Congress 88*, 1988, pp. 73-76.
- [151] Dickson R., Jones C., Harris B., Leach D., Moore D., The environmental fatigue behaviour of carbon fibre reinforced polyether ether ketone, *Journal of Materials Science*, 20(1), 1985, pp. 60-70.
- [152] Hojo M., Tanaka K., Gustafson Claes G., Hayashi R., Effect of water environment on propagation of delamination fatigue cracks in unidirectional CF/PEEK laminates, *Nippon Kikai Gakkai Ronbunshu A Hen*, 56(526), 1990, pp. 1335-1342.
- [153] Product information, Vetrotex Textilglas, *Gevetex Textilglas GmbH, Germany*.
- [154] Loewenstein K. L., *The manufacturing technology of continuous glass fibers*, 6, 2 ed., Amsterdam, Elsevier, 1983.
- [155] Moiseev Y. V., Zaikov G. E., Chemical resistance of polymers in aggressive media, New York, Consultant Bureau, 1987, pp. 205-273.
- [156] Zimmerman H., Nguyen T. K., Investigations on thermal and hydrolytic degradation of poly(ethylene terephthalate), *Polymer Engineering and Science*, 20(10), 1980, pp. 680-683.
- [157] Jabarin S., Lofgren E., Thermal stability of polyethylene terephthalate, *Polymer Engineering and Science*, 24(13), 1984, pp. 1056-1063.
- [158] Bastioli C., Guanella I., Romano G., Effects of water sorption on the physical properties of PET, PBT and their long fibers composites, *Polymer Composites*, 11(1), 1990, pp. 1-9.
- [159] Jabarin S. A., Lofgren E. A., Effects of water absorption on physical properties and degree of molecular orientation of poly(ethylene terephthalate), *Polymer Engineering and Science*, 26(9), 1986, pp. 620-625.
- [160] Ha S.-W., Reber R., Eckert K.-L., Petitmermet M., Mayer J., Wintermantel E., Baerlocher C., Gruner H., Chemical and morphological changes of vacuum-plasma-sprayed hydroxyapatite coatings during immersion in simulated physiological solutions, *Journal of the American Ceramic Society*, 81(1), 1998, pp. 81-88.
- [161] ASTM D 790M, Standard test methods for flexural properties of unreinforced and reinforced plastics and electrical insulating materials, *Annual Book of ASTM Standards*, 8(01), 1992.
- [162] Trustrum K., Jayatilaka S., On estimating the Weibull modulus for a brittle material, *Journal of Materials Science*, 14, 1979, pp. 1080-1084.
- [163] Herrera-Franco P. J., Drzal L. T., Comparison of methods for the measurement of fibre/matrix adhesion in composites, *Composites*, 23(1), 1992, pp. 2-27.

- [164] Shonaike G. O., Hamada H., Maekawa Z., Matsuda M., Yuba T., Matsuo T., Influence of cooling conditions on the mechanical properties of commingled yarn composites, *Journal of Thermoplastic Composite Materials*, 9(1), 1996, pp. 76-89.
- [165] Denault J., Vu Khanh T., Fiber/matrix interaction in carbon/PEEK composites, *Journal of Thermoplastic Composite Materials*, 6(3), 1993, pp. 190-204.
- [166] Ye L., Friedrich K., Interlaminar fracture of commingled-fabric-based GF/PET composites, *Composites*, 24(7), 1993, pp. 557-564.
- [167] Mandell J. F., Chen J. H., McGarry F. J., A microdebonding test for in situ assessment of fibre/matrix bond strength in composite materials, *J. Adhesion*, 1, 1980, pp. 40-44.
- [168] Marshall D. B., Oliver W. C., An indentation method for measuring matrix-fiber frictional stresses in ceramic composites, *Journal of the American Ceramic Society*, 67(12), 1984, pp. C 259-C 260.
- [169] Marshall D. B., Oliver W. C., Measurement of interfacial mechanical properties in fiber-reinforced ceramic composites, *Journal of the American Ceramic Society*, 70(80), 1987, pp. 542-548.
- [170] Mandell J. F., Hong K. C. C., Grande D. H., Interfacial shear strength and sliding resistance in metal and glass-ceramic matrix composites, *Ceramic Engineering and Science Proceedings*, 8(7-8), 1987, pp. 937-940.
- [171] Brun M. K., Singh R. N., Effect of thermal expansion mismatch and fiber coating on the fiber/matrix interfacial shear stress in ceramic matrix composites, *Advanced Ceramic Materials*, 3(5), 1988, pp. 506-509.
- [172] Morseher G., Pirouz P., Heuer Arthur H., Temperature dependence of interfacial shear strength in SiC-fiber-reinforced reaction-bonded silicon nitride, *Journal of the American Ceramic Society*, 73(3), 1990, pp. 713-720.
- [173] Gao Y. C., Mai Y. W., Cotterell B., Fracture of fiber-reinforced materials, *Zeitschrift fuer angewandte Mathematik und Physik*, 39, 1988, pp. 550-572.
- [174] Zhou L. M., Mai Y. W., A new model for evaluation of the interfacial friction coefficient and residual clamping stress in a fibre-push-out test, *Philosophical Magazine Letters*, 68(1), 1993, pp. 5-11.
- [175] Zhou L. M., Mai Y. W., On the fibre pullout and pushout problem: Effect of fibre anisotropy, *Zeitschrift fuer angewandte Mathematik und Physik*, 44, 1993, pp. 769-775.
- [176] Zhou L. M., Mai Y. W., Ye L., Kim J. K., Techniques for evaluating interfacial properties of fibre-matrix composites, *Key Engineering Materials*, 104-107, 1995, pp. 549-600.
- [177] Liang C., Hutchinson J. W., Mechanics of the fiber pushout test, *Mechanics of Materials*, 14(3), 1993, pp. 207-221.
- [178] Hsueh C.-H., Interfacial debonding and fiber pull-out stresses of fiber-reinforced composites. VII. Improved analyses for bonded interfaces, *Materials Science and Engineering*, A154(2), 1992, pp. 125-132.
- [179] Grande D. H., Mandell J. F., Hong K. C. C., Fibre-matrix bond strength studies of glass, ceramic, and metal matrix composites, *Journal of Materials Science*, 23(1), 1988, pp. 311-328.
- [180] Hsueh C.-H., Interfacial friction analysis for fibre-reinforced composites during fibre push-down (indentation), *Journal of Materials Science*, 25(2A), 1990, pp. 818-828.
- [181] Shetty D. K., Shear-lag analysis of fiber push-out (indentation) tests for estimating interfacial friction stress in ceramic-matrix composites, *Journal of the American Ceramic Society*, 71(2), 1988, pp. C107-109.
- [182] Piggott M. R., Debonding and friction at fibre-polymer interfaces. I: Criteria for failure and sliding, *Composites Science and Technology*, 30, 1987, pp. 295-306.
- [183] Desaegeer M., Verpoest I., On the use of the micro-indentation test technique to measure the interfacial shear strength of fibre-reinforced polymer composites, *Composites Science and Technology*, 48(1-4), 1993, pp. 215-226.
- [184] Kerans R. J., Marshall D. B., Theoretical analysis of the fiber pullout and pushout tests, *Journal of the American Ceramic Society*, 74(7), 1991, pp. 1585-1596.
- [185] Powell M. D., An efficient method for finding the minimum of a function of several variables, *The Computer Journal*, 7, 1964.

LIST OF ABBREVIATIONS AND SYMBOLS

Abbreviations

CF	carbon fibers	GF	glass fibers
CFRP	carbon fiber reinforced polymer	IDSS	interface debonding shear stress
CLSM	confocal laser scanning microscopy	IR	infrared
CT	compact tension	KFRC	knitted fabric reinforced composite
DL	double layer	PEEK	poly(ether-ether-ketone)
FEM	finite element method	PET	poly(ethylene-terephthalate)
FRC	fiber reinforced composite	SBF	simulated body fluid
FRP	fiber reinforced polymer	UD	unidirectional

Symbols

α	linear thermal expansion coefficient	σ_{deb}	interface stress
δ	fiber displacement	σ_z	radial fiber stresses
ε	strain	τ_0	fiber friction caused by asperity interactions
Γ	surface fracture energy	τ_{deb}	interface debonding shear stress
λ	compliance	τ_{fric}	interface friction shear stress
μ	friction coefficient		
ν	Poisson coefficient		
σ_{cl}	thermal induced clamping stress		
a	crack length	E_{tot}	total dissipated energy
Δa	crack growth	F_{peak}	peak force
Deb_{end}	fiber debonding end	G_{12}	shear modulus
Deb_{ini}	fiber debonding initiation	G_{IC}	energy release rate
DI	ductility index	K_{IC}	fracture toughness
E	Young's (elastic) modulus	P	probability of failure
E^*	effective modulus	R	characteristical strength
ΔE_{crack}	energy released in crack growth Δa	s	fiber slippage
E_{init}	initiation energy	$U_{debonding}$	debonding energy
E_{prop}	propagation energy	$U_{friction}$	friction energy
		V_F	fiber volume content

ACKNOWLEDGMENTS

Die vorliegende Dissertation entstand im Rahmen eines Brite Euram Projektes (BRE2-0938, Project BE-7290). Finanziert wurde die Arbeit von der europäischen Union und dem Bundesamt für Bildung und Wissenschaft. Verwirklicht werden konnte sie nur durch die Mithilfe von vielen Personen, denen ich an dieser Stelle herzlichst danken möchte:

Meinem Referenten, Herrn Prof. Dr. E. Wintermantel, dessen Unterstützung weit über das Fachliche hinausging. Durch seine dynamische und unkonventionelle Weise die Professur zu leiten, hat er mir den nötigen Freiraum gegeben ohne mich dabei das Ziel aus den Augen verlieren zu lassen.

Herrn Prof. Dr. P. J. Uggowitzer für die Übernahme des Korreferats, das kritische Durchlesen der Arbeit und den wertvollen fachlichen Input.

Allen meinen Projektpartnern, insbesondere den Herren A. Buck sen. und jun., Inhaber der Firma Buck TSP GmbH, welche das Ausgangsmaterial vestrikt haben und mir damit eindrücklich gezeigt haben, dass sich die Gestrickstechnologie nicht auf das Herstellen von Pullovern beschränkt. Weiter den Herren M. Huisman, R. Reinicke und J. Peter vom Institut für Verbundwerkstoffe GmbH, für das zur Verfügung stellen der Impactanlage und die Hilfe bei der Durchführung der Versuche.

Frau Dr. J. Janczak-Rusch für die Hilfe bei der Interpretation der Push-out Resultate, Herrn B. Lüthi für seine Kreativität und sein Durchhalten im Zusammenhang mit dem Push-out Modell und Analyzer, Herrn G. Bürki für das magische Händchen bei der Durchführung der Versuche und Herrn Dr. L. Rohr für die angenehme und fruchtbare Zusammenarbeit mit der EMPA Thun. Ebenso Herrn P. Wyss von der EMPA Dübendorf für das Ausleihen der Thermokamera und die fachkundige Einführung in deren Bedienung.

Zwei Persönlichkeiten haben den Inhalt dieser Arbeit entscheidend geprägt. Meinem Partner Dr. Joop de Haan und meinem "Mentor" Dr. Jörg Mayer sei für die unzähligen Gespräche, ihre Tips und ihre fordernde Kritik herzlichst gedankt. Ebenso geht ein grosses Dankeschön an Dr. Marc Petitmermet, von dem ich wertvolle Korrekturen und uneingeschränkte Hilfe insbesondere in der kritischen Schlussphase erhalten habe.

Viele Studierende haben in Form von Semester- und Diplomarbeiten entscheidende Beiträge zum Gelingen dieser Arbeit geleistet. Ihnen und allen anderen Freunden, Kolleginnen und Kollegen auf deren Hilfe ich immer zählen konnte, möchte ich meine Dankbarkeit aussprechen: Andi, Anna, Beat, Ben, Christoph, Christophe, Curzio, Dieter, Dirk, Dominique, Erdal, Fredi, Fränzi, George, Hampi, Kurosch, Kurt, Markus, Martin, Matthias, Patrik, Philipp, Ramon, René, Rolf, Sabine, Suk-Woo, Thorleif, Toru, Urs, Viola und der ganzen BWB-Crew, der ich eine interessante und erfolgreiche Zukunft in der Forschung wünsche.

Ein inniger Dank geht an meine Familie, der diese Arbeit gewidmet ist und die mir unbeschreiblich viel bedeutet. Schliesslich danke ich Dir, Anouk, für alles was ich hier weder ausdrücken kann noch will. *Ce qui précède définit seulement une façon de penser. Maintenant, il s'agit de vivre - Albert Camus.*

CURRICULUM VITAE

Personal information

Name: Roland Reber
Nationality: Switzerland
Citizen of: Schangnau (BE)
Date and place of birth: June 26, 1969, Basel
permanent address: Albisriederstrasse 181
8047 Zürich, Switzerland

Education

ETH Zürich 1995 - present
Scientific research and Ph.D. thesis at the Chair of
Biocompatible Materials Science and Engineering

ETH Zürich 1990 - 1995
Diploma in Materials Engineering

Gymnasium, Liestal 1985 - 1988
Matura, Typus C

Practical experience

AMS Medinvent (Pfizer), Crissier June - October 1993
optimization of a vascular implant (stent)

Swiss Bank Corporation, Basel December 1989 - September 1990
mainframe operating

CIBA-Geigy AG, Basel October 1988 - February 1989
pharmaceutical reasearch (osteoporosis)

Awards

Medaille der ETH Zürich 1995